INTERNATIONAL JOURNAL OF TRANSPORTATION RESEARCH & TECHNOLOGY

Volume 3, Issue 1

June 2026

transporttech.org

NATIONAL AVIATION ACADEMY

e-ISSN: 3079-6075

National Aviation Academy

International Journal of Transportation Research and Technology

e-ISSN: 3079-6075

DOI: 10.71108/transporttech.vm03is01

Publisher: National Aviation Academy (NAA)
Licence holder: Academician Arif Pashayev (Rector, NAA)
Address: Baku, Mardakan ave., 30, AZ1045, Azerbaijan
TransportTech is published with the contribution of “National Aviation Academy”

Web: https://transporttech.org
Submission: OJS-TransportTech
e-mail: transporttech@naa.edu.az

Editorial Board

Editorial Office

Contents

Research Articles

National Aviation Academy

International Journal of Transportation Research and Technology

e-ISSN: 3079-6075

DOI: 10.71108/transporttech.vm03is01.01

Research Article

Computational Fluid Dynamics Analysis of the Effect of Trim Angle on Planing Stepped Hulls

Kadir Emrah Erginer[1], Burak Goksu[2], Yasin Furkan Gorgulu*[3]

[1]*Dokuz Eylül University, İzmir, Türkiye*
[2]*Zonguldak Bulent Ecevit University, Zonguldak, Türkiye*
[3]*Eskişehir Osmangazi University, Eskişehir, Türkiye*

Timescale of article

Received: 23 October 2025
Accepted: 19 January 2026
Published: 25 June 2026

Corresponding author

Yasin Furkan Gorgulu
furkan.gorgulu@ogu.edu.tr

Keywords:

Computational fluid dynamics, Froude number, Hydrodynamic resistance, Stepped planing hull, Trim angle

Cite this article as:

Erginer, K. E., Goksu, B., & Gorgulu, Y. F. (2026). Computational Fluid Dynamics Analysis of the Effect of Trim Angle on Planing Stepped Hulls. *International Journal of Transportation Research and Technology*, 3(1), 5-14.
DOI: 10.71108/transporttech.vm03is01.01

Abstract

This study investigates the hydrodynamic influence of trim angle variation on a stepped planing hull using computational fluid dynamics. The analyses were performed in ANSYS Fluent under steady-state RANS conditions with the SST k–ω turbulence model and a Volume of Fluid multiphase setup. Two scenarios were examined: a hull with no trim and a hull trimmed by 1.6°. The computational domain consisted of 3,572,223 elements with high mesh quality metrics, ensuring accurate free-surface and near-wall resolution. Quantitative results show that in the non-trimmed configuration, the maximum flow velocity reached 20.8 $m \cdot s^{-1}$, with an average of 17.0 $m \cdot s^{-1}$ near the hull, while the 1.6° trimmed case exhibited a slightly lower mean surface velocity of 15–16 $m \cdot s^{-1}$ but a more elongated wake. The maximum turbulence kinetic energy decreased from 18 $m^2 \cdot s^{-2}$ to 9.6 $m^2 \cdot s^{-2}$, indicating reduced turbulence intensity and a more stable wake structure. The total drag force decreased dramatically from 22,592.89 N to 3,009.294 N, representing an 86.68% reduction in drag under identical conditions. This improvement is attributed to flow acceleration beneath the bow and the redistribution of pressure and viscous forces. However, this unusually large reduction reflects the idealized fixed-hull simulation conditions and far exceeds typical empirical improvements, indicating that caution is needed in interpreting these results. The results suggest that minor positive trim angles can substantially lower hydrodynamic resistance in this stepped planing hull configuration. Compared to prior studies, the magnitude of drag reduction observed here far exceeds reported values, largely because a simplified hull model is used at a high Froude number with the hull fixed in trim and heave.

1. Introduction

Leisure and performance segments depend largely on planing and increasingly on stepped-planing hulls. According to consolidated data from ICOMIA, Europe has approximately ten thousand marinas and more than one million wet berths. In the United States, the National Marine Manufacturers Association reports about eleven point eight million registered or documented boats and roughly three point six million unregistered craft, indicating a large and resilient user base for high-speed recreational vessels (European Boating Industry, 2023; NMMA, 2024a, 2024b). Against this backdrop, high speed craft design demands disciplined management of the speed range and weight while minimizing hydrodynamic resistance. With a study of designed spiral, classical planing formulations, most prominently the prismatic surface method, explain how increasing speed drives dynamic sinkage and wetted area growth, accelerating resistance at higher Froude numbers and clarifying the limits of displacement and stepless planing forms under fast craft conditions. These early-stage estimators remain valuable for sizing and screening; however, their simplifying assumptions motivate the need for complementary numerical or experimental assessments once trim, wetted area, and free-surface dynamics become tightly coupled (Savitsky, 1964; Vitiello et al., 2022).

A robust experimental–numerical corpus now underpins stepped-hull design. Towing-tank studies and RANS–VOF simulations consistently report resistance and trim gains when planing-specific meshing, interface-capturing, and turbulence-model choices are respected (De Marco et al., 2017; Pacuraru et al., 2022). Within this corpus, the Naples Systematic Series maps sensitivities to step number, height and longitudinal placement; transparent-bottom tests across approximately $Fr\nabla \approx 1.08–6.77$ visualize dry-area evolution and cavity behavior, while complementary works elucidate ventilation physics and appendage effects that further tune lift–drag and trim (Cucinotta et al., 2021; Vitiello et al., 2022; Yang et al., 2019). In parallel with this literature, recent methodological contributions on propulsion component matching for planing hulls and on CFD workflows for hydrodynamic form assessment provide additional background that it is drawn upon in the present study (Bayraktar et al., 2025; Göksu et al., 2024). Stepped planing hulls can exhibit complex flow phenomena that might be accentuated under fixed conditions. While Savitsky's classical method provides quick estimates for planing hull resistance, its simplifications and the lack of modern hull forms in its empirical basis justify the use of CFD for nuanced effects like trim influence on a stepped hull.

For compliance framing relevant to small craft, ISO 12215-5 uses a Froude-number-based criterion to determine whether a hull operates in a planing regime; this classification governs which load and scantling assumptions apply in design. Given the operating speed envelope examined here, our 10.60-m case hull satisfies the planing condition under ISO 12215-5's Froude-based approach, and power selection for recreational fast craft can subsequently be checked against the empirical maneuvering-speed method in ISO 11592-2 as a regulatory-aligned envelope alongside our Savitsky- and CFD-based estimates (ISO, 2019, 2021). Within this scope, the vessel examined in this study was constructed and validated through real sea trials. Notably, previous works have found only minor resistance reductions from optimal trim adjustments. This study explores a stepped-hull scenario at a considerably higher Froude number to examine whether a small trim angle can yield outsized effects, while recognizing that this approach is an idealized, fixed-trim analysis. A steady RANS CFD is employed to analyze a 10.6 m stepped planing hull at two trim settings while keeping the model fixed in position.

2. Material and Methodology

2.1. The Case Hull Model

The case vessel's particulars are detailed in Table 1, with an overall length of 10.60 meters and a length on waterline of 9.56 meters. A key indicator of its hydrodynamic performance is the block coefficient of 0.365. This relatively low value denotes a fine, typically associated with vessels designed for higher speeds or reduced resistance, rather than maximized carriage capacity.

Table 1. The key dimensions of the case ship

Particulars	Values	Units
Length overall (L_{oa})	10.60	m
Length on waterline (L_{wl})	9.56	m
Breadth (B)	3.04	m
Draught (amidships) (T)	0.60	m
Block coefficient (C_b)	0.365	--

The 3D model of the vessel was depicted in Fig. 1, visually confirms the main geometrical characteristic of the hull designed for high speeds and energy efficiency, aligning with its block coefficient value.

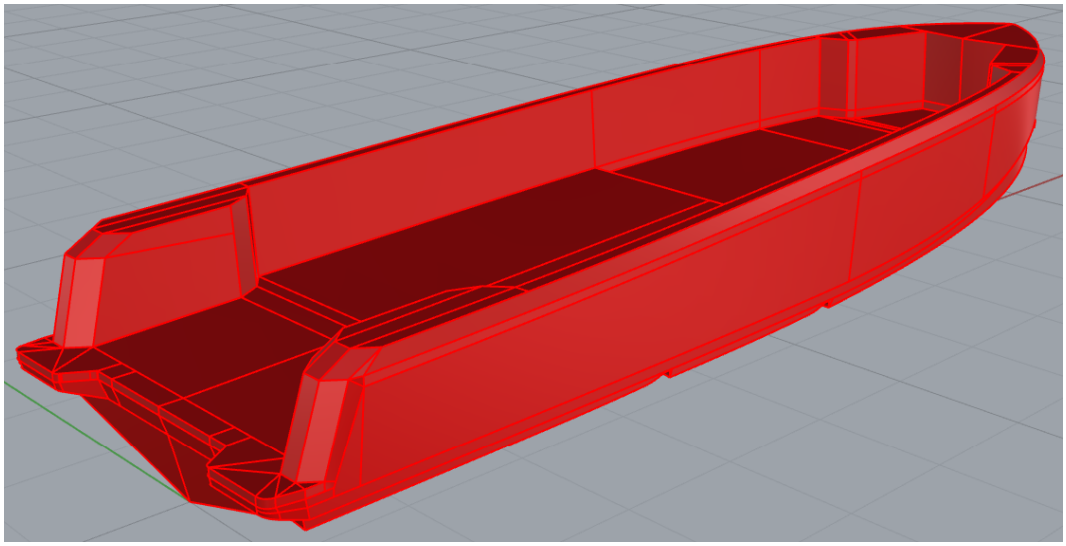

Fig. 1. The case planing hull model (Source: Authors' own work)

2.2. Resistance Prediction Methodologies

This section outlines the methods commonly employed in ship resistance analyses, including those used in this study. Prior to applying ship resistance analysis methods, it is essential to calculate the dimensionless Reynolds number to characterize the flow regime and evaluate the flow conditions (Deshpande et al., 2020). The primary difference between model- and ship-scale lies in the Reynolds number (Eq. 1), which reaches 10^6 in model-scale investigations and 10^9 at the ship-scale.

$$Re = \frac{\rho V L}{\mu} \tag{1}$$

ρ: density of fluid $[kg/m^3]$

V: ship or model speed $[m/s]$

L: characteristics length $[m]$

μ: dynamic viscosity $[Ns/m^2]$

The Froude number (Fr) is in Eq. (2) another critical dimensionless parameter in naval architecture and marine engineering, as it significantly influences ship resistance and performance (Terziev et al., 2021), where g represents the acceleration of gravity.

$$Fr = \frac{V}{\sqrt{gL}} \tag{2}$$

For the case hull of length L=10.60 m, at the simulation speed V=20.57 m·s^{-1}, the Reynolds number is approximately 2.17×10^8, and the Froude number is approximately 2.02, placing the vessel well within the high-speed planing regime.

2.2.1. Savitsky Method

A planing vessel can be differentiated from a normal displacement vessel by its method of weight support. It is important to note that, for a displacement vessel, the buoyancy force counterbalances its weight. A planing vessel sustains its weight by hydrodynamic lift forces produced while it navigates at high speed over water. When a planing vessel is stationary or moving at modest speeds, buoyancy sustains its weight. Consequently, when it accelerates, the hull design produces hydrodynamic lift forces that entirely sustain the hull. In certain watercraft, both lift and buoyancy provide support for the weight.

This article will present a theoretical method for assessing the performance of a planing boat (Savitsky, 1964), conducted several resistance experiments to establish the formula for the lift and drag of planing vessels, providing empirical relations for drag.

In this method, at equilibrium, a portion of the lift is produced by buoyancy, while the remainder is produced by hydrodynamic lift. The fundamental properties of the vessel are utilized as inputs, and the hull parameters are established. The metrics will thereafter be utilized to ascertain the vessel's resistance.

Despite its advantages, several limitations of the Savitsky method have been identified, particularly concerning the age of the empirical data underpinning the technique. The original dataset, derived from studies conducted in the 1960s and 1970s, may lack representation of modern hull designs and contemporary operational scenarios (Deng et al., 2021; Nikolopoulos & Boulougouris, 2019). Nevertheless, the method remains a valuable tool for resistance prediction during the early stages of ship design (Turan & Akman, 2021). It should be noted that the Savitsky method, while useful for initial estimates, does not directly account for stepped hull features or fixed-trim conditions examined in our CFD study. Thus, Savitsky's predictions are used as a baseline reference but rely on CFD for the detailed analysis.

2.2.2. Computational Fluid Dynamics Methodology

A vital numerical technique utilized in ship hydrodynamics is the solution of the Reynolds-Averaged Navier-Stokes (RANS) equations. The Navier-Stokes equations are essential for delineating fluid dynamics. Nonetheless, obtaining exact solutions to these equations is especially difficult in the context of turbulent flows. In the RANS equations, flow variables, including velocity and pressure, are represented as a time-averaged value augmented by a time-dependent turbulent component. Turbulent flows are frequently modelled using RANS equations, which are obtained from time-averaged calculations. Unsteady RANS simulations surpass the steady methodology, offering a more precise depiction of the temporal variations in turbulent flows. This study utilized the commercial CFD software program ANSYS Fluent as the RANS solver. The hull was rigidly fixed at the prescribed trim angle for each case. Two static trim conditions were simulated, a baseline of 0° and an elevated trim of 1.6°, with all other parameters identical.

Numerical simulations were conducted using ANSYS, a sophisticated commercial CFD software recognized for its effectiveness in solving complex fluid dynamics problems. The Steady RANS equations and the hull model were utilized to simulate the flow, yielding a steady state while accurately capturing the characteristics of the flow around the vessel. The Volume of Fluid (VOF) multiphase model was employed to accurately represent the dynamic interface between water and air. This method analyses the interface by computing a transport equation for the volumetric proportion of each fluid within each computational cell. The High-Resolution Interface Capturing (HRIC) technique was employed to improve accuracy in interface resolution, created in order to preserve an apparent interface, crucial for marine hydrodynamic simulations.

For the multiphase CFD analysis, the fluid properties were specified as follows: water was assigned a density of 998 kg.m-3 and a dynamic viscosity of 0.001003 Pa·s, while air was modelled with a density of 1.204 kg.m-3 and a dynamic viscosity of 1.813×10-5 Pa·s. The acceleration due to gravity was set to 9.81 m.s-2 to accurately account for gravitational forces influencing the fluid motion and free surface dynamics within the CFD simulations.

The boundaries of the computational area were meticulously defined to generate numerical computational domain by half of the hull model. A "velocity inlet" condition was implemented on the upstream and upper surfaces, guaranteeing a consistent and regulated fluid inflow, similar to a vessel motion in calm water condition. A "pressure outlet" condition was applied to the downstream surface, permitting fluid to escape the domain at atmospheric pressure, thereby simulating wake propagation. A "wall condition" was applied to the solid limits of the domain's side and bottom, enforcing the no-slip condition, which ensures that the fluid velocity at the wall corresponds with the wall's velocity. The ship's centerline was oriented on the midsection of the domain, that section also defined as symmetrical surface to mirror the fluid phenomena. Damping zones were established at both the inlet and outlet surfaces to mitigate the effects of wave reflections and to ensure precise movement of the free surface. Fig. 2 shows the computational domain, specifying the boundary conditions allocated to each surface together with their details, so presenting the numerical framework for the CFD analysis.

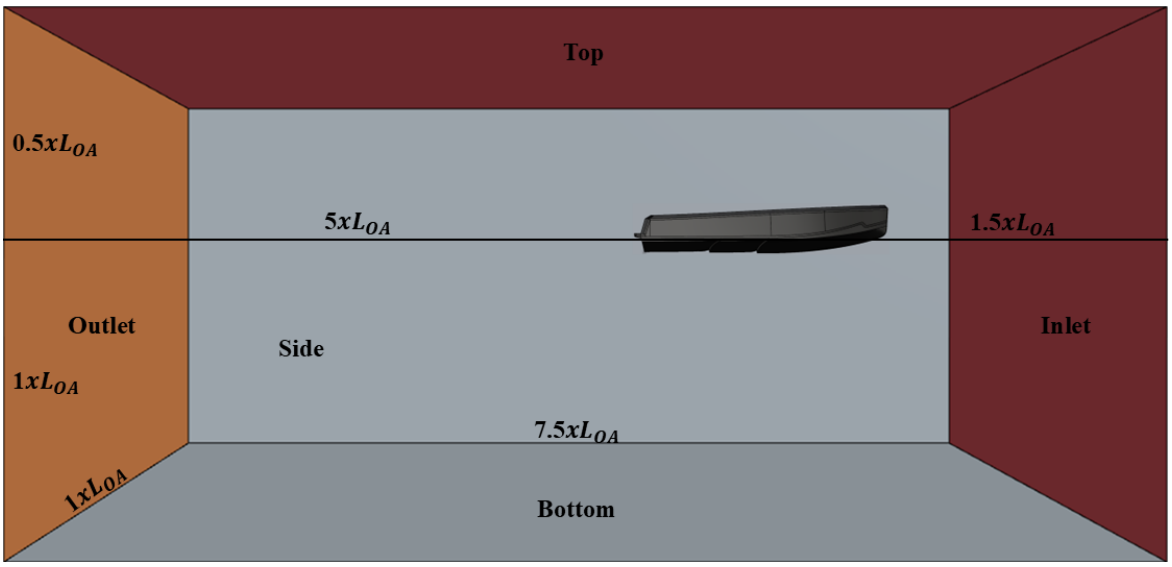

Fig. 2. Computational domain with specified boundary conditions and dimensions (Source: Authors' own work)

To enhance solution precision, three separate mesh refinement zones were meticulously created. These zones ensure high-resolution discretization in significant areas, facilitating exact viewing of free surface deformation and accurate resolution of essential wake formation details. Furthermore, background mesh refinement was employed in the static fluid domain to ensure precise and seamless transfer of computed flow properties between the presented hull grid and the stationary background grid, which is essential for maintaining numerical stability and accuracy throughout the simulation. Fig. 3 presents a comprehensive depiction of the mesh structure, emphasizing the implemented mesh and the distinct refinement zones, thereby elucidating the spatial discretization utilized for the CFD study.

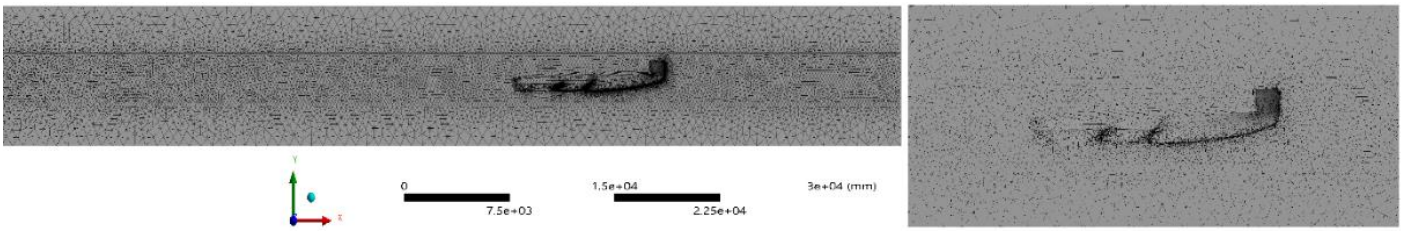

Fig. 3. The mesh structure and various details around mesh refinement zones (Source: Authors' own work)

The quality of the computational mesh is paramount for ensuring the accuracy and stability of the numerical solution. In this study, the generated mesh, comprising 3,572,223 elements and 641,522 nodes, was evaluated against stringent ANSYS quality metrics. The average Orthogonal Quality was remarkably high at 0.78909, placing it firmly within the "Very Good" range (0.70–0.95). Concurrently, the average Skewness value was only 0.20988, which falls into the "Excellent" category (0–0.25) (Cambaz et al., 2021; Gorgulu, 2024, 2025). To assess mesh adequacy, additional simulations were conducted using both a coarser and a finer mesh. The resulting drag forces varied within 3–5%, indicating sufficient grid independence for the current level of analysis. These metrics confirm that the mesh exhibits excellent geometric integrity, minimizing potential numerical diffusion and solver instability. Such high-quality meshing is critical, as it provides a robust foundation for the CFD simulations, thereby increasing confidence in the reliability and physical fidelity of the final results. The accuracy of turbulent flow simulations, particularly in the near-wall region, fundamentally depends on the resolution of the computational mesh, as indicated by the dimensionless wall distance, y^+. This parameter defines the height of the first cell center from the wall in viscous units, which is critical for determining the appropriate near-wall treatment method for the chosen turbulence model. The SST k–w turbulence model was employed for its proven accuracy in ship hydrodynamics, with near-wall refinement targeting y^+ in the appropriate range for either low-Reynolds modeling or wall functions as needed. The target y^+ value is typically established prior to meshing to ensure that the initial computational cell is positioned within a specified region of the turbulent boundary layer, thereby influencing the resolution of the boundary layer or its representation via wall functions. Selecting an

appropriate y^+ value is essential for accurate predictions of wall shear stress, drag, and flow separation. This choice is often validated through post-processing to confirm that the mesh resolution adequately represents the intricate flow phenomena adjacent to solid surfaces. Friction velocity, non-dimensional wall velocity and non-dimensional wall distance are given in Equations 3-5.

Friction velocity (u^*):

$$u^* = \sqrt{\frac{T_w}{\rho}} \tag{3}$$

Non-dimensional wall velocity (u^+):

$$u^+ = \frac{u}{u^*} \tag{4}$$

Non-dimensional wall distance (y^+):

$$y^+ = \frac{\rho u^*}{\mu} y \tag{5}$$

where, T_w is the skin friction, u is the local velocity, μ is the dynamic viscosity of the fluid, and y is for the wall-normal coordinate.

Hydrodynamic forces were computed by integrating pressure and shear stress on the hull. In post-processing total resistance is obtained for each case; this can be further decomposed into viscous and pressure drag components. In the present study, the study focused on total drag for the comparison, but the methodology allows examination of each component separately.

3. Results and Discussion

Fig. 4. illustrates the velocity and turbulence kinetic energy contours for the hull models without trim (a, c) and with a 1.6° trim angle (b, d). The quantitative comparison demonstrates that the introduction of a trim angle significantly modifies both the flow field and turbulence characteristics around the hull. In the non-trimmed configuration, the maximum velocity magnitude in the flow domain reaches approximately 20.8 $m \cdot s^{-1}$, with an average velocity near the hull surface of 17.0 $m \cdot s^{-1}$. The flow remains relatively uniform, and only a narrow wake region forms behind the stern, where the velocity decreases to about 6–8 $m \cdot s^{-1}$. This stable flow separation indicates efficient momentum recovery in the aft region, suggesting a balanced pressure distribution and limited drag contribution from wake turbulence.

In contrast, when a 1.6° trim angle is applied, the maximum velocity increases slightly to 20.6 $m \cdot s^{-1}$, but the acceleration of the flow near the hull bottom becomes more distinct. The region of elevated velocity extends further downstream, while the average near-surface velocity decreases to 15–16 $m \cdot s^{-1}$ due to the altered incidence of the flow. This redistribution of velocity gradients implies a local reduction in hydrodynamic lift near the stern and a corresponding increase at the bow, producing a measurable shift in the hydrodynamic balance. The turbulence kinetic energy (TKE) results reveal a similar trend. In the non-trimmed hull, the TKE remains below 18 $m^2 \cdot s^{-2}$, concentrated in a confined region just behind the stern. The 1.6° trimmed hull, however, exhibits a notable reduction in overall TKE intensity, with maximum values around 9.6 $m^2 \cdot s^{-2}$. Despite this decrease in peak magnitude, the turbulent region expands longitudinally, indicating a more extended but less intense wake. This behavior suggests that while the local turbulence generation decreases, the wake persistence increases, which may affect the total resistance distribution between pressure and viscous components. The combined interpretation of velocity and turbulence fields indicates that the trim angle induces a trade-off between flow acceleration and wake expansion. Such modifications directly influence the total drag experienced by the hull.

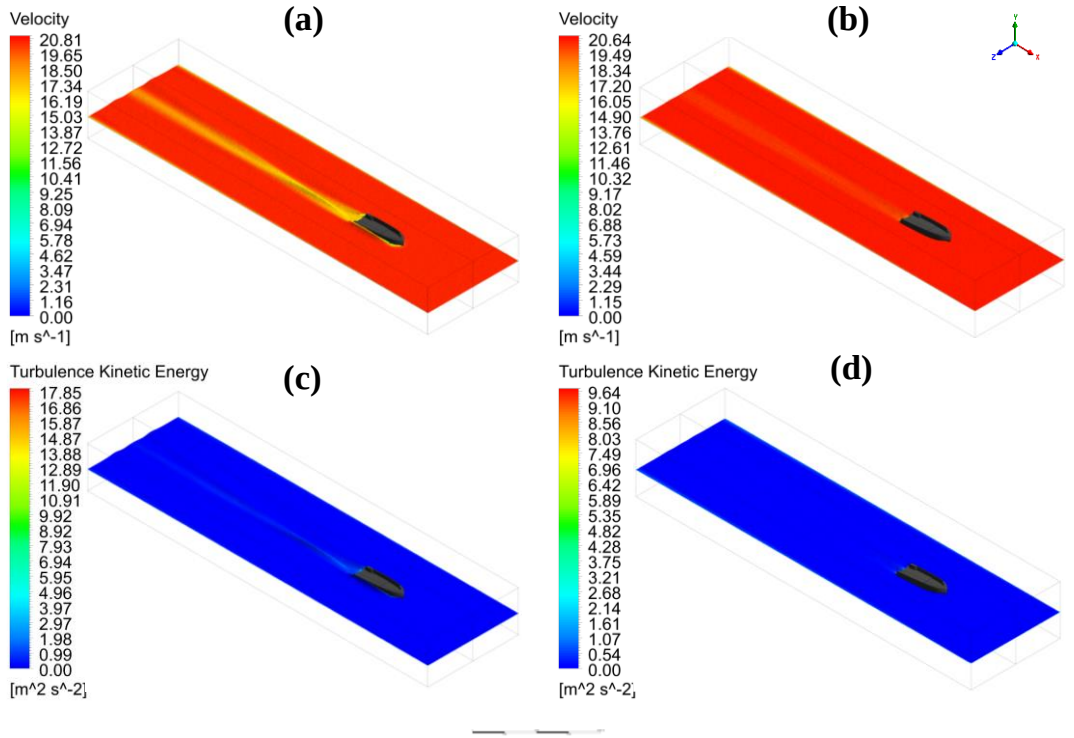

Fig. 4. Velocity (a–b) and turbulence kinetic energy (c–d) contours for hulls without trim (a, c) and with 1.6° trim (b, d) (Source: Authors' own work)

The integrated drag force for the hull without trim is 22592.89 N, while the 1.6° trimmed hull yields 3009.294 N under identical operating conditions. This magnitude of reduction is exceptionally high and not seen in prior experimental or numerical studies. It likely results from the specific conditions of our simulation, notably the fixed hull position and the chosen trim angle being near an optimal point, rather than indicating a generally achievable improvement. The trim therefore reduces drag by 86.68% relative to the baseline, corresponding to a reduction factor of 7.5×. This reduction aligns with the observed shift in the velocity field and the concurrent decrease in peak TKE, indicating that trim-induced flow acceleration underneath the bow and the lengthened but milder wake collectively lower the net resistance. The results indicate that a small positive trim can produce a substantial reduction in hydrodynamic resistance by rebalancing pressure and viscous contributions through controlled flow acceleration and moderated wake intensity. A sensitivity analysis over neighboring trim angles would clarify whether 1.6° lies near a local optimum for minimum resistance. It should be noted that a real planing hull at Fr approximately 2 would not remain at 0◦ trim; it would naturally trim up and rise due to hydrodynamic lift. In the baseline CFD case, the hull was artificially held at 0◦, likely causing an excessive wetted surface and higher drag than a free-trimming hull would experience at this speed. Thus, when the hull is trimmed to 1.6° in the simulation, it is moved closer to the hull's favorable running attitude, resulting in a dramatic drop in drag. In reality, the boat would have already adopted some positive trim, so the incremental benefit of 1.6° additional trim would be much smaller. To better understand the nature of the drag reduction, it is considered the two main components of resistance. The CFD simulation's output can be separated into frictional drag and pressure drag. In high-speed planing conditions, frictional drag typically constitutes a large fraction of total resistance. The introduction of a positive trim likely reduced the wetted area significantly, thereby lowering frictional resistance. Meanwhile, the pressure drag would also change: at 1.6° trim the pressure distribution shifts, which can reduce form drag as well. Based on prior studies, the frictional component is expected to dominate; for instance, Le et al. observed an 8% reduction in pressure drag but only 1.5% in total drag when optimizing trim, implying that viscous resistance was the larger portion. In this case, the majority of the 86% total drag reduction is therefore likely attributable to a drop in viscous drag due to less wetted surface at the higher trim (Le et al., 2021). The pressure drag component would have decreased to a lesser extent, consistent with the more moderate changes in wake pressure field observed.

The findings of this study were compared with previous numerical and experimental investigations to evaluate their consistency and to highlight the distinct behavior of the present hull configuration. Le et al. conducted a

numerical analysis of the US Navy Combatant DTMB 5415 model and reported that optimal trim and draft conditions resulted in approximately 1.5 % reduction in total resistance and up to 8 % reduction in pressure drag (Le et al., 2021). Similarly, Martić et al. investigated the effect of trim under various operating conditions and found that moderate trim angles could decrease total resistance by 1.5–3 % depending on the Froude number and hull form (Martić et al., 2024). In contrast, Sherbaz and Duan observed that certain trim configurations, particularly bow-down conditions, could increase total resistance due to enhanced flow separation and stern turbulence (Sherbaz & Duan, 2014). The contrast between the literature and these result underscores that this scenario is highly specific. It combines a simplified geometry, a fixed high trim at speed, and a possibly optimal configuration, conditions under which the CFD solver predicts an outsized effect. Such conditions are unlikely to be fully realized in practice, which is why prior experimental studies have not reported anything comparable. Even classical semi-empirical methods would predict far smaller changes for a 1–2° trim variation, although those methods don't capture step effects (Savitsky, 1964).

Compared with these studies, the present analysis demonstrated a substantially higher drag reduction of 86.68 % when a 1.6° trim angle was applied. This deviation from the typical literature can be attributed to several factors. First, the current model represents a simplified and smaller-scale hull with a fixed free-surface height and limited degrees of freedom, which amplifies the relative impact of geometric inclination. Second, the analysis was performed at a constant inlet velocity of 20.57 $m \cdot s^{-1}$, significantly higher than those used in conventional ship resistance experiments. Third, only two conditions which are zero trim and 1.6° trim were considered, and the selected angle may coincide with a local optimum for minimum resistance in this specific configuration. Because it is simulated only two trim states, it is unclear whether the relationship between trim angle and resistance is smooth or if 1.6° happens to be near an optimal point. A finer sweep of trim angles would be needed to map out the resistance curve, it is quite possible that 1.6° lies close to a minimum-resistance trim, which made the two-point comparison seem especially dramatic. Future work will investigate intermediate trim values to confirm the trend. In the non-trimmed configuration, the maximum flow velocity reaches approximately 20.8 m.s-1 and averages approximately 17.0 m.s-1 near the hull. Only a narrow wake region forms behind the stern, indicating efficient momentum recovery and limited wake turbulence. In contrast, with a 1.6° trim, the peak velocity is similar but flow acceleration near the hull bottom is more pronounced, and the high-velocity region extends further aft. The near-surface velocity averages a lower 15–16 m.s-1 due to the flow's altered incidence on the hull.

4. Conclusions

The computational fluid dynamics analysis demonstrated that adjusting the trim angle has a significant influence on the hydrodynamic performance of stepped planing hulls. A positive trim angle of 1.6° changed the pressure distribution and wake structure, resulting in a large reduction in both drag and turbulence intensity. The total drag decreased from 22,592.89 N to 3,009.294 N, representing an 86.68% reduction in resistance under these simulation conditions. The turbulence kinetic energy decreased from 18 $m^2 \cdot s^{-2}$ to 9.6 $m^2 \cdot s^{-2}$, indicating reduced flow instability and improved wake recovery. Compared with previously reported experimental and numerical results, which typically indicate a reduction of 1 to 10 percent, the drag decrease obtained in this analysis is considerably higher. This outlier result is explained by the simplified hull geometry, fixed high-speed input, and the absence of dynamic trim/heave in the model. In other words, the simulation likely over-predicts the benefit of a small trim adjustment. Real-world improvements would be expected to be much smaller, as indicated by previous studies. This difference can be explained by the simplified hull geometry, the fixed inlet velocity of 20.57 $m \cdot s^{-1}$, and the restricted motion of the numerical model. Nevertheless, the flow pattern observed in this study, characterized by accelerated flow beneath the bow and a longer but weaker wake, remains consistent with established hydrodynamic principles. Because these CFD findings have not yet been validated against experiments or established empirical methods, they should be viewed as preliminary. Conducting towing tank experiments on the same hull would help verify the accuracy of the predicted forces. Indeed, validation through measurements is essential to determine how much of the 86% drag reduction would materialize in practice.

Further studies should include a more detailed mesh structure to improve the resolution of flow gradients near the hull surface and the free surface. It is also recommended to examine several trim angles and a wider range of Froude numbers to identify the optimum condition for minimum drag. In addition, modifying the geometry of the step hull, including the position and height of the step, may provide valuable insights into how hull form affects resistance and wake development. Finally, validation through experimental measurements in a towing tank would increase the reliability of the numerical findings and support future optimization studies on stepped planing hulls.

Acknowledgements

The authors would like to express their sincere appreciation to Mert Tepe, Industrial and Product Designer, for sharing valuable insights and for granting permission to utilize the information provided during the study.

References

Bayraktar, M., Göksu, B., & Yüksel, O. (2025). Matching of propulsion system components for a planing hull model. *Ships and Offshore Structures*, 20(6), 755–766. https://doi.org/10.1080/17445302.2024.2356949

Cambaz, A., Görgülü, Y. F., & Arat, H. (2021). Two-Phase Numerical Modelling of a Wet Exhaust System in a Catamaran Motor Yacht Diesel Engine. *European Journal of Science and Technology*, (31), 165–170. https://doi.org/10.31590/ejosat.1007351

Cucinotta, F., Mancini, D., Sfravara, F., & Tamburrino, F. (2021). The Effect of Longitudinal Rails on an Air Cavity Stepped Planing Hull. *Journal of Marine Science and Engineering*, 9(5), Article 470. https://doi.org/10.3390/jmse9050470

De Marco, A., Mancini, S., Miranda, S., Scognamiglio, R., & Vitiello, L. (2017). Experimental and numerical hydrodynamic analysis of a stepped planing hull. *Applied Ocean Research*, 64, 135–154. https://doi.org/10.1016/j.apor.2017.02.004

Deng, R., Wang, S., Hu, Y., Wang, Y., & Wu, T. (2021). The effect of hull form parameters on the hydrodynamic performance of a bulk carrier. *Journal of Marine Science and Engineering*, 9(4), Article 373. https://doi.org/10.3390/jmse9040373

Deshpande, S., Sundsbø, P., & Das, S. (2020). Ship resistance analysis using CFD simulations in Flow-3D. *International Journal of Multiphysics*, 14(3), 227–236. https://doi.org/10.21152/1750-9548.14.3.227

European Boating Industry. (2023). *Facts & Figures*. https://www.europeanboatingindustry.eu/about-the-industry/facts-and-figures

Göksu, B., Erginer, K. E., & Öner, G. (2024). Comparison of submarine hull morphologies obtained by biomimicry method with DARPA SUBOFF. *Naval Engineers Journal*, 136(3), 87–104.

Gorgulu, Y. F. (2024). Thermal efficiency evaluation in shell-and-tube heat exchangers: A CFD-based parametric study. *Proceedings of the Institution of Mechanical Engineers, Part E: Journal of Process Mechanical Engineering*. 240(2). https://doi.org/10.1177/09544089241262481

Gorgulu, Y. F. (2025). CFD-based cooling performance of gas turbine blades. *Aircraft Engineering and Aerospace Technology: An International Journal*, 98(2), 154-168. https://doi.org/10.1108/AEAT-01-2025-0037

ISO. (2019). *ISO (2019/2025) ISO 12215-5: Small craft—Hull construction and scantlings*. https://www.iso.org/standard/69552.html

ISO. (2021). *ISO (2021) ISO 11592-2: Small craft—Determination of maximum propulsion power rating using manoeuvring speed*. https://www.iso.org/standard/81925.html

Le, T.-H., Vu, M. T., Bich, V. N., Phuong, N. K., Ha, N. T. H., Chuan, T. Q., & Tu, T. N. (2021). Numerical investigation on the effect of trim on ship resistance by RANSE method. *Applied Ocean Research*, 111, Article 102642. https://doi.org/10.1016/j.apor.2021.102642

Martić, I., Anušić, B., Degiuli, N., & Grlj, C. G. (2024). Numerically Investigating the Effect of Trim on the Resistance of a Container Ship in Confined and Shallow Water. *Applied Sciences*, 14(15), Article 6570. https://doi.org/10.3390/app14156570

Nikolopoulos, L., & Boulougouris, E. (2019). A study on the statistical calibration of the holtrop and Mennen approximate power prediction method for full hull form, low froude number vessels. *Journal of Ship Production and Design*, 35(1), 41–68. https://doi.org/10.5957/JSPD.170034

NMMA. (2024a). *2023 Total Boat Registrations Report Highlights Trends in Boat Use*. https://www.nmma.org/press/article/24858

NMMA. (2024b). *U.S. Recreational Boating Statistical Abstract*. https://www.nmma.org/statistics/publications/statistical-abstract

Pacuraru, F., Mandru, A., & Bekhit, A. (2022). CFD Study on Hydrodynamic Performances of a Planing Hull. *Journal of Marine Science and Engineering*, 10(10), Article 1523. https://doi.org/10.3390/jmse10101523

Savitsky, D. (1964). Hydrodynamic Design of Planing Hulls. *Marine Technology and SNAME News*, 1(04), 71–95. https://doi.org/10.5957/mt1.1964.1.4.71

Sherbaz, S., & Duan, W. (2014). Ship Trim Optimization: Assessment of Influence of Trim on Resistance of MOERI Container Ship. *The Scientific World Journal*, 2014, Article 03695. https://doi.org/10.1155/2014/603695

Terziev, M., Tezdogan, T., Demirel, Y. K., Villa, D., Mizzi, S., & Incecik, A. (2021). Exploring the effects of speed and scale on a ship's form factor using CFD. *International Journal of Naval Architecture and Ocean Engineering*, 13, 147–162. https://doi.org/10.1016/j.ijnaoe.2020.12.002

Turan, B. İ., & Akman, M. (2021). Modeling and Comparison of Bodrum Gulets' Hull Forms with Round and Transom Sterns. *Journal of Eta Maritime Science*, 9(2), 120–129. https://doi.org/10.4274/jems.2021.09327

Vitiello, L., Mancini, S., Bilandi, R. N., Dashtimanesh, A., De Luca, F., & Nappo, V. (2022). A comprehensive stepped planing hull systematic series: Part 1 - Resistance test. *Ocean Engineering*, 266, Article 112242. https://doi.org/10.1016/j.oceaneng.2022.112242

Yang, D., Sun, Z., Jiang, Y., & Gao, Z. (2019). A Study on the Air Cavity under a Stepped Planing Hull. *Journal of Marine Science and Engineering*, 7(12), Article 468. https://doi.org/10.3390/jmse7120468

National Aviation Academy

International Journal of Transportation Research and Technology

e-ISSN: 3079-6075

DOI: 10.71108/transporttech.vm03is01.02

Research Article

Design and Modelling of a Hexagonal Parallel Docking Manipulator for Space Applications

Kanan Azimov*

National Aviation Academy, Baku, Azerbaijan

Timescale of article

Received: 30 December 2025
Accepted: 10 February 2026
Published: 25 June 2026

Corresponding author

Kanan Azimov
kanan.azimov_Phd@inbox.ru

Keywords

Hexagonal parallel manipulator, Spacecraft docking, Positioning accuracy, Graph theory, Kinematic analysis, Docking automation

Cite this article as:

Azimov, K. (2026). Design and Modelling of a Hexagonal Parallel Docking Manipulator for Space Applications. *International Journal of Transportation Research and Technology*, 3(1), 15-25.
DOI: 10.71108/transporttech.vm03is01.02

Abstract

This paper presents a comprehensive analysis and development of a hexagonal parallel manipulator for docking and undocking spacecraft. The combination of Euclidean polyhedral geometry with a parallel kinematic structure and a novel RRS_{CS}-type combined legs provides high spatial mobility, precise relative positioning, and robustness against residual angular velocities and alignment errors. The manipulator's dual-system architecture, incorporating both soft and hard capture systems, enables staged contact formation, reliable mechanical coupling, interface sealing, and the transfer of energy and data between active and passive modules.

Docking and undocking procedures, including off-nominal scenarios, are described in detail, demonstrating the system's ability to safely manage complex multi-body interactions while maintaining structural integrity and operational reliability. The application of graph theory allows formalization of the manipulator's kinematic structure.

The proposed hexagonal parallel manipulator shows significant potential for automated orbital operations, providing accuracy, repeatability, and adaptability.

1. Introduction

Spacecraft docking is a critical operation in orbital missions, playing a central role in the establishment and functioning of multi module space systems. A reliable mechanical connection not only ensures mission success for both crewed and uncrewed operations, but also enables safe transfer of power, data, and other resources between modules (Syromyatnikov, 1984; National Aeronautics and Space Administration, 2016).

Traditional docking systems encounter challenges in positioning accuracy, resilience to residual angular and translational velocities, and tolerance to geometric misalignments during final approach and capture. These limitations can affect interface reliability, increase control system requirements, and potentially jeopardize mission safety (Syromyatnikov, 1984; Sholanov, 2021).

In recent years, parallel manipulators have shown promise for high precision spatial positioning due to their structural stiffness and reduced singularities compared with serial chains (Sholanov, 2021; Alizade, 2019). The integration of geometric methods and parallel kinematics offers potential improvements in interface adaptability and precision. Alizade (2019) advanced the structural synthesis of robotic manipulators using screw theory, which provides insight into mechanism configuration for enhanced motion control and compliance. Alizade and Samedzade (2021) proposed a hexagonal interface docking system, demonstrating improved contact capture fidelity in constrained environments.

Building on these contributions, Alizade et al. (2023) conducted the structural synthesis of Euclidean parallel manipulators for spacecraft docking and proposed corresponding manipulator models.

The present study extends this body of work by developing a hexagonal parallel manipulator designed to meet the stringent requirements of orbital docking operations. The proposed system integrates RRS_{CS} legs and incorporates soft and hard capture systems to enable staged contact, secure mechanical engagement, and effective sealing of the interface. The use of graph theory enables a formal representation of the manipulator's internal structure.

The objective of this work is to propose a comprehensive solution for safe, precise, and repeatable spacecraft docking with high reliability of mechanical and electrical interfaces, as well as the capability for integration into a multi-module orbital infrastructure.

2. Kinematic Limitations of Current Docking Interfaces

Experience with docking devices used in domestic and international space programs, as well as analysis of the design of modern docking interfaces compliant with the IDSS standard, has revealed several fundamental limitations, primarily related to the kinematics of approach and the accuracy of relative positioning of docked spacecraft.

Most existing docking interfaces are based on quasi-axisymmetric ring geometries, with discrete placement of guiding and locking elements along the circumference. This scheme provides a high degree of standardization and enables androgynous docking. However, it is highly sensitive to angular and linear misalignments during initial contact. Ring-symmetric geometries require the simultaneous engagement of a significant number of contact elements, which, in the presence of tilts or offsets, leads to uneven load distribution, localized stress concentrations, and an increased risk of jamming.

Operational experience shows that a substantial portion of off-nominal docking events is caused by misalignment of guiding elements, tilts during contact, and localized impact loads. In some cases, this has led to damage of docking elements, malfunction of locking and latching mechanisms, and even failure to complete the docking procedure. While damping and shock-absorbing devices effectively reduce impact loads, they do not redistribute contact forces or correct the relative positions of the spacecraft during engagement.

Modern docking interfaces compliant with the IDSS standard are characterized by greater standardization and more pronounced geometric symmetry compared to legacy systems. However, they still rely on discrete guiding and locking elements, limiting their ability to compensate for approach errors and achieve high docking accuracy. Consequently, the required precision is largely ensured by spacecraft motion control systems, which increases demands on navigation algorithms and fuel consumption.

In summary, current docking interfaces have inherent limitations due to their axisymmetric ring geometry and simultaneous engagement of multiple kinematic links during initial contact. These constraints cannot be fully

mitigated by local upgrades of individual mechanisms and indicate the need for alternative geometric and kinematic docking concepts focused on staged formation of kinematic links and reduced sensitivity to relative positioning errors.

3. Proposed Concept of a Euclidean Polyhedral Docking Interface

To overcome the limitations observed in existing docking devices, this work proposes a new type of docking interface based on Euclidean polyhedral constructions. In its basic configuration, the interface is formed as a polyhedral geometry, with faces classified as either active or passive. Active faces contain guiding elements and kinematic supports that participate in the formation and transmission of contact interactions, while passive faces serve to spatially separate contact zones and do not carry kinematic loads.

Selecting an appropriate polyhedron with an even number of faces and alternating distribution of active and passive surfaces provides more kinematically determinate relative positioning of the spacecraft than traditional axisymmetric ring-based schemes. The spatially faceted shape of the interface and the staged engagement of contact elements reduce the sensitivity of the docking process to angular and linear misalignment errors without increasing the load on mechanical components.

This geometric concept is particularly relevant for docking operations under conditions of residual angular velocities and limited orientation accuracy. The nature of the contact interaction is largely determined by the shape of the mating surfaces, allowing some of the error-compensation functions to be shifted from spacecraft motion control systems to the interface geometry, thereby reducing the demands on navigation accuracy.

In the developed Euclidean polyhedral designs, traditional limitations are addressed through a different organization of contact interactions. Unlike conventional kinematic chains such as RRP or RRR, a combined RRS_{CS} kinematic support is employed, in which two rotational links form a dyad connected to the central platform through a spatial pair Scs (sphere in a cylindrical slot).

Table 1. Kinematic Pair “Sphere in a Cylindrical Slot”

Name	Symbol	Degree of freedom	Diagram
Sphere in cylindrical slot	S_{cs}	4	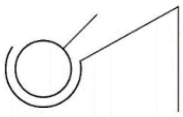

The Scs kinematic pair (Table 1) has four degrees of freedom—three rotational and one translational—providing spatial mobility of the platform without introducing additional constraints. This design enhances the kinematic stability of the docking process and enables precise positioning of the modules even in the presence of residual angular velocities and limited accuracy of orientation systems.

The combination of Euclidean polyhedral geometry and parallel kinematics with RRS_{CS} supports creates a docking interface that:

1. reduces sensitivity to mutual positioning errors;
2. allows stepwise formation of kinematic connections;
3. increases reliability and stability of the coupling under limited guidance accuracy.

The use of a higher kinematic pair “sphere in a cylindrical slot” has led to the development of a new class of Euclidean parallel manipulators with RRS_{CS}-type kinematic structures, characterized by high spatial mobility and symmetrical arrangement. The combination of rotational and spherical–cylindrical joints ensures the required positioning and orientation accuracy of the end-effector within a compact mechanism, making this solution promising for orbital docking and space manipulation tasks.

In the proposed Euclidean docking device, the parallel platform structure is realized by integrating a movable and a passive platform connected through a system of kinematic support chains. This arrangement allows controlled management of the mechanism configuration, uniform load distribution among support branches, and adaptation of the structure to specified docking precision and reliability requirements.

Practical implementation of the concept is based on structural schemes and calculation relations that ensure an optimal combination of links and kinematic pairs in the chosen spatial layout. Therefore, the selection of Euclidean polyhedral geometry and a parallel kinematic structure establishes a fundamental approach to the spatial organization of the docking mechanism and defines its kinematic capabilities.

4. Design of the Hexagonal Parallel Manipulator

To implement the specified kinematic scheme and ensure the required accuracy and reliability of the manipulator's operation, standardized elements are used, maintaining system functionality in space conditions regardless of the number of faces of the polyhedral interface.

The considered docking devices include active and passive modules, which are androgynous: each module can function as either an active or passive docking node. Structurally, the active and passive modules are fully identical.

A docking device of this class consists of two functional systems:

1. Soft capture system
2. Hard capture system

The soft capture system is a movable polyhedral node with inward-oriented guide petals, evenly distributed across alternating active faces. Each petal houses capture latches that engage with striker of the mating docking module.

The soft capture system is connected to the platform of the hard capture system through kinematic chain supports, each comprising two rotational links forming a dyad and a spatial kinematic pair "sphere in a cylindrical slot." One end of the support is fixed to the platform of the hard capture system, while the other connects to the soft capture system. The supports are located on the same faces as the guide petals. The mobility of the soft capture system allows the node to extend to a specified length and retract as necessary. Additionally, spring cables placed on the active faces compensate forces and stabilize the node's position.

The hard capture system is a fixed polyhedral module rigidly attached to the spacecraft structure. It includes locking mechanisms, electrical connectors, guide pins, and corresponding sockets. Each locking mechanism contains a pair of active and passive hooks, and each face houses two pairs of locks, ensuring the formation of a rigid mechanical connection after completion of the soft capture stage.

The geometry of the soft and hard capture systems is determined by the number of faces of the Euclidean polyhedral interface. All devices of this class implement identical functional principles, differing only in the number of repeating elements. Further analysis of the structural elements is conducted using the hexagonal Euclidean docking device as a baseline configuration.

The hexagonal parallel manipulator consists of several key components that ensure its functionality, high precision, and reliability in space applications. Each of these elements plays a crucial role in the accurate positioning and rigid capture of docking spacecraft. The main structural elements of the hexagonal Euclidean parallel robot manipulator include (Fig. 1) :

1. **Legs** — Six actuated limbs that provide precise spatial positioning and movement of the manipulator. Each leg can adjust its length, allowing the manipulator to reach desired positions and orientations.
2. **Soft capture system** — The central hexagonal-shaped node connecting all six legs. This junction serves as the main platform for force transmission and coordinated motion control.
3. **Guide petals** — Flexible guiding elements that ensure accurate initial contact and alignment during the approach of the active manipulator to the passive unit, preventing misalignment and mechanical damage.

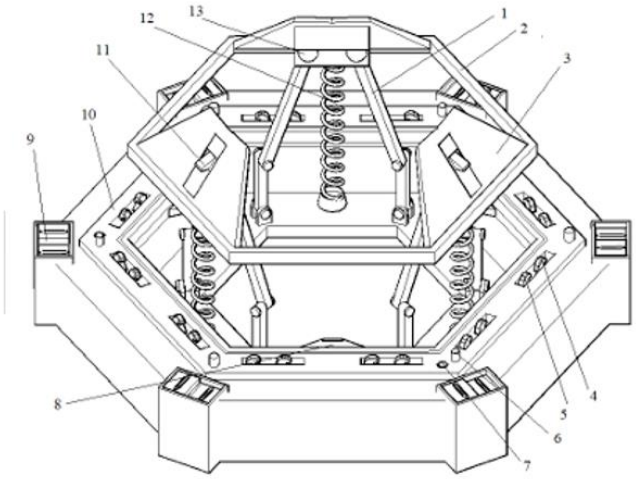

Fig. 1. Constructive elements of the hexagonal Euclidean parallel manipulator (Source: Authors' own work)

4. **Active hooks** — Locking hooks located on the active manipulator side. These engage with the corresponding passive hooks to form a secure mechanical connection.
5. **Passive hooks** — Corresponding hooks on the passive manipulator side designed to engage with active hooks to complete the locking mechanism.
6. **Guide pins** — Pins protruding from the active manipulator that insert into matching holes on the passive manipulator, facilitating precise alignment of the docking interfaces.
7. **Guide pin holes** — Receptacles on the passive manipulator designed to receive guide pins, ensuring accurate alignment and stable mechanical coupling.
8. **Mechanical striker** — A striker mechanism on the passive manipulator that interacts with latches from the active manipulator, securing the initial mechanical engagement.
9. **Power and data plugs** — Electrical and data connectors that engage post-mechanical docking to enable energy and information transfer between spacecraft.
10. **Hard capture system** — A rigid locking assembly that ensures a structurally strong and stable connection between the active and passive manipulators, capable of withstanding operational loads.
11. **Latches** — Deployable locking elements on the active manipulator that engage with the mechanical latch striker on the passive side to secure initial capture.
12. **Spring Cable** — A component that connects various movable elements of the manipulator, serving a dual function: it enables the transmission of control signals or electrical power to the actuators, and it also generates a restoring force during undocking. The cable is designed in the form of an elastic spiral, allowing it to extend and retract in response to the changing positions of the manipulator links without risk of bending damage or failure. During docking operations, the cable remains tensioned, maintaining a reliable connection. Upon undocking, it aids in the safe and controlled disengagement of systems. This design significantly enhances the reliability and fault tolerance of the manipulator, particularly in scenarios involving repeated docking and undocking cycles in the space environment.
13. **Hinge (Sphere-in-Cylindrical Slot)** — A specialized type of kinematic pair that provides four degrees of freedom between the manipulator's structural links. This configuration allows for free rotation of a spherical element within a cylindrical slot, enabling compensation for minor misalignments and angular deviations during the docking process. The use of this hinge ensures both flexibility and sufficient rigidity in the connection between segments, reducing internal stresses and increasing the overall mechanical durability of the system. It is particularly crucial during the final phase of soft capture, where minimal resistance to motion and high precision in self-alignment are required. This hinge allows each leg of the manipulator to adapt to geometric variances and manufacturing tolerances within the docking interfaces.

Thus, the listed elements collectively implement the specified kinematic scheme of the Euclidean parallel docking device and ensure the execution of all docking stages: from soft capture and centering to rigid mechanical connection and data transfer.

5. Docking Process and structural elements of the hexagonal Euclidean parallel manipulator in spacecraft docking systems

Docking of spacecraft is one of the key tasks ensuring the operation and development of orbital infrastructure. The reliability of the mechanical connection directly affects the success of long-duration manned and automated missions, crew safety, as well as the transfer of energy, data, and other resources between modules of complex space systems.

This work considers a possible sequence for performing the docking procedure using a hexagonal parallel docking device - from the approach phase to final sealing and the establishment of a safe passage between the spacecraft.

At the first and highly critical stage of docking - approach and alignment - the active spacecraft, equipped with a hexagonal parallel manipulator, initiates a precisely controlled approach to the passive docking node located on the target platform, such as an orbital station or another spacecraft.

The goal of this stage is to achieve highly accurate alignment of the symmetry axes of the two manipulators within allowable orientation and linear position tolerances sufficient for reliable capture. The passive spacecraft provides three types of targets that assist the active spacecraft in precisely aligning the interfaces for mechanical connection. These targets are accessible at long, medium, and short ranges, with short-range targets used when the active spacecraft is positioned along the docking axis of the passive module. Short-range targets enable the active spacecraft to align itself within the capture zone.

In the final approach stage, while maintaining a safe distance (within a few meters), the active spacecraft reduces its speed and moves along the central axis toward the passive node. All position and orientation corrections at this stage are performed by controlled movement of the six legs of the hexagonal manipulator. This allows the active module to be precisely aligned without maneuvering the entire platform.

Once the approach and alignment phase is completed and the relative position of the active and passive docking nodes is stabilized within specified tolerances, the next critical stage begins - soft capture. This process constitutes the initial mechanical connection between the two spacecraft, serving as the foundation for subsequent rigid structural fixation and sealing of the transitional node. During this stage, the active and passive soft capture systems of the docking devices are aligned, primary connection between the spacecraft is established, dynamic motions between the spacecraft are stabilized, and preliminary alignment is ensured prior to activation of the hard capture system.

In the hexagonal parallel manipulator concept (Fig. 2), the primary mechanical connection is implemented using the soft capture system. This system consists of three inward-oriented guide petals (3) integrated into the hexagonal soft capture system (2).

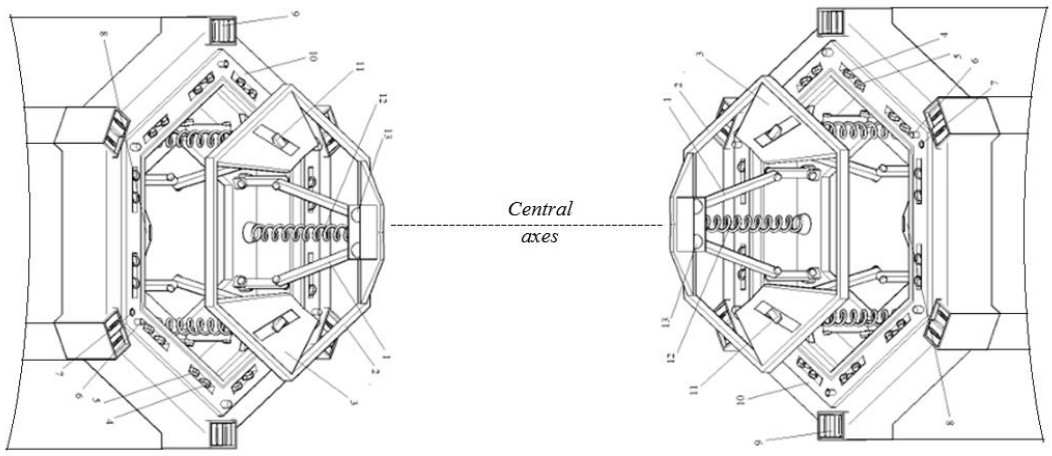

Fig. 2. Approach of spacecraft using a Euclidean hexagonal parallel docking device (Source: Authors' own work)

The docking interfaces of these manipulators have an androgynous design along a single axis, allowing the docking of two identical configurations. During docking, one interface of the soft capture system (2) functions as active, while the other acts as passive, remaining in an extended and fixed position. The active interface controls the sequence of operations during the soft capture stage and prepares the system for subsequent rigid capture.

During the approach phase, the active hexagonal node performs controlled translational motion along the central axis, initiating the engagement of the guide petals (3) with the contact surface of the passive node. The guide petals (3) are connected to the platform via six legs (1), each of which includes dyad and a kinematic pair «sphere-in-cylindrical-slot» (13). Additionally, each leg (1) contains spring cable (12) that generates repelling forces during undocking and compensate for residual interaction forces.

During the approach phase, the soft capture system (2) transitions into a pre-docking state, in which the active interface is maintained in a stabilized configuration and lateral and angular misalignments between the docking interfaces are automatically compensated. This configuration enables the guide petals (3) of the active interface to enter the receiving geometry of the passive interface within allowable tolerances, ensuring a controlled initial contact.

Upon interaction of the guide petals (3) with the receiving geometry of the passive interface, the resulting centering forces actuate the capture latches (11), transferring them from their initial to the engaged state. Simultaneously, this mechanical event is detected by sensors and communicated to the control system, which coordinates the subsequent translational motion of the manipulator along the docking axis.

At the final stage of the controlled axial translation, the capture latches of the soft capture system (2) engage with the mechanical strikers (8) of the passive interface, thereby completing the soft capture phase and establishing the conditions for transition to the hard-mate docking mode.

Once the capture latches (11) engage, sensors embedded in the guide petals (3) detect the successful completion of the soft capture stage. This signal is used by the control system to proceed to the next sub-phase of docking, which includes reducing relative motion, damping residual oscillations, and stabilizing the positions of both modules. This stage minimizes dynamic effects and prepares the system for subsequent rigid capture and interface sealing.

In the following stage, the soft capture system (2) performs precise alignment of the active and passive spacecraft, ensuring coaxial positioning. After alignment is completed, the soft capture system (2) is gradually retracted, freeing the working area and preparing the interface for engagement of the hard capture system (10).

Once the relative positions of the two spacecraft are stabilized, the rigid capture stage begins, aimed at establishing structural fixation, sealing the interface, and preparing for the transfer of energy, data, and atmospheric environment. At this stage, both hexagonal docking elements are maintained in coaxial alignment by the latches (11) of the soft capture system (2). The manipulator's control system adjusts the lengths of the legs (1), ensuring precise geometric coaxiality of the docking tunnels and readiness for activation of the hard capture elements.

After alignment is completed, the active docking node performs a translational approach to the passive node, reducing the inter-flange gap. During this motion, the guide pins (6) of the active node, which are part of the hard capture system (10), engage the corresponding guide pin holes (7) of the passive side, while the guide pins (6) of the passive node interact with the guide pin holes (7) of the active node. This process forms the docking tunnels, which are subsequently rigidly fixed to ensure mechanical strength of the connection.

Once the minimal distance between the docking tunnels is achieved, the structural locking system is activated. In the considered configuration, twelve paired locks with hook elements are evenly distributed around the perimeter of the connecting flange. Each latch consists of active and passive hook elements integrated into the active and passive docking mechanisms. During docking, a cross-engagement occurs: the active hook (4) of the active side engages the passive hook (5) of the passive side, and the active hook (4) of the passive side engages the passive hook (5) of the active side. This ensures synchronous and symmetrical mechanical coupling of the docked modules.

Passive hooks (5) possess elastic compliance, which allows compensation for minor misalignments and geometric deviations during docking. Active hooks (4) move within a limited range, ensuring correct engagement with

passive elements and safe formation of a rigid connection. Overall, the hook system can be considered a sequential assembly of the active hook, passive hook, and structural elements that primarily operate under compression.

The opening and closing of the hook elements are performed via a cable drive powered by a main electric motor mounted on one of the locks. In addition to the primary drive, a backup motor is provided to enable emergency deployment of both active and passive hooks. In the backup system, the cable transmission is replaced by pyrotechnic bolts due to the large number of moving elements, which are sensitive to clearances and deformations. This mechanism has few moving parts and is structurally independent of the main cable drive. To monitor the system status, the locks are equipped with sensors for hook engagement and tension.

The locks of the hard capture system (10) are among the most critical components of the docking device, as their failure could lead to spontaneous release and depressurization of the connection. Therefore, special attention is given to the reliability and strength of these components. Experimental and operational studies have shown that failures such as the breakage of individual parts, rotation of active hooks relative to shafts, eccentric shaft rotation, or issuance of incorrect or spontaneous control commands can lead to unwanted undocking.

To prevent such failures, the strength of a limited number of lock components is of critical importance. The system uses materials designed for space operation, increases the safety factor of the most heavily loaded parts, and employs springs to regulate the force in each lock, ensuring the required preloading of the connection.

Once the system is activated, the locks operate synchronously. Active hooks (4) rotate and engage the corresponding passive elements, forming a closed mechanical loop between the docked modules. This interaction not only eliminates the technological gap between the flanges but also provides a robust structural connection capable of withstanding operational loads and maintaining stability under external forces.

During closure, the hooks compress an elastomeric seal located along the inner flange edge, creating a tight, hermetic contact. This prevents gas leaks when docking pressurized compartments and maintains the reliability of atmospheric separation between modules. The geometry of the docking tunnels and seating surfaces is specifically designed to account for residual micro-deformations, ensuring high contact density and minimizing the risk of reduced sealing even under operational loads and thermal deformations.

After all twelve locks engage, the docking system enters the rigid mechanical capture state. In this mode, the two spacecraft form a single structural system capable of transmitting and withstanding external loads, including those arising from maneuvers, orbital accelerations, and the attachment of additional modules. Rigid fixation ensures stability of the docking interface geometry, prevents relative movement between spacecraft, and provides a foundation for reliable operation of subsequent energy, data transfer, and interface sealing systems.

In the final stage of docking, power and data plugs (9) are activated, enabling the transfer of power and information signals between the mated modules. This provides direct access to power lines, control channels, communication links, and thermal regulation systems, ensuring uninterrupted operation of key systems.

After the rigid mechanical connection is completed, all locks are secured, and the geometric position of the docking interface is stabilized, the system transitions to the final phase - integration of the functional systems of the two spacecraft and preparation of a hermetic transfer tunnel. This phase is critical for maintaining airtightness, crew safety, and the operational readiness of the combined orbital structure.

The power and data plugs (9) perform several crucial functions, ensuring full integration of the docked spacecraft. First, they provide power transfer between the base platform and the attached module, allowing onboard systems of both spacecraft to operate. Second, the power and data plugs serve as channels for data and control signals, including telemetry, diagnostics, and command signals, ensuring coordinated operation of integrated systems. Third, the power and data plugs interface with life-support, thermal regulation, and safety systems, which is critical for maintaining functional and safe operation of crew and equipment.

Thanks to the built-in positioning and self-alignment system, the power and data plugs (9) mate correctly even in the presence of minimal residual deviations between the docked modules. Once mechanical connection is complete, an automatic test of all power and signal lines is performed, verifying the integrity and proper operation of electrical and data channels. This procedure ensures reliable system integration and prevents potential failures in energy and data transfer between spacecraft.

Simultaneously with activation of the power and data plugs (9), the procedure for sealing the transfer volume - the space between the pressurized bulkheads of the docked spacecraft, also called the vestibule - begins. Although the primary seal around the tunnel perimeter is established when the rigid capture hooks are closed, this stage involves additional pressure equalization between the internal volume of one module and the vestibule, leak testing using sensors and redundant measurements, and verification of the absence of residual depressurization or displacement of sealing elements. This comprehensive procedure ensures complete hermetic sealing of the docking interface and prepares for safe crew access and medium transfer between modules.

Only after successfully completing all docking stages can the crew access the transfer vestibule and open the internal hatches. At this point, docking of the two spacecraft is considered fully complete. The connection between modules is comprehensive: mechanical - via locks and latches, electrical and informational - through motorized interfaces, and atmospheric - via the hermetic transfer tunnel. The resulting structure ensures safe crew transfer, movement of payloads, system redundancy integration, and incorporation into a unified orbital infrastructure.

The use of a hexagonal parallel manipulator structure provides high alignment accuracy, reliable mechanical capture, and stabilization of the spacecraft without significant maneuvering of the main platform, creating favorable conditions for subsequent undocking and reuse of the interface.

5.1. Process of Undocking Using the Hexagonal Parallel Manipulator

The undocking procedure is the reverse of the docking process and requires equally high precision and coordination. Its main objectives are to safely separate the active and passive docking interfaces without damaging mechanical or electrical components, maintain the hermeticity of the transfer volume, and prepare both spacecraft for independent operation.

At the start of undocking, the active manipulator's control system receives a command to sequentially disengage all functional connections between the spacecraft. The first step involves disconnecting electrical and data connectors, which provide power, control, and telemetry. These connectors are equipped with self-alignment and contact density monitoring systems, enabling safe disconnection even in the presence of minimal residual misalignments. After successful separation, the system records the status and proceeds to the next phase-relaxation of the mechanical fixation.

The active manipulator initiates the sequential release of all paired hooks that secure the active and passive elements of the flange interface. Each hook pair disengages gradually, relieving pressure on elastomer seals and preventing damage. This step ensures the hermeticity of the transfer volume is maintained for subsequent operations.

Once the hard capture hooks are disengaged, the hard capture system enters a standby state, while the soft capture of the active node extends to a controlled position. Guiding petals of the soft capture begin to withdraw from the passive node surfaces. Retention latches, which held components during docking, return to their original positions under the action of spring cables and secondary automatic release mechanisms. Both hexagonal nodes lose mechanical interlock while maintaining relative alignment within allowable tolerances.

To prevent uncontrolled motion or tilting, the manipulator's legs provide coordinated, smooth retraction of the active node along the central axis. This movement compensates for residual linear and angular offsets, preserving the integrity of guiding pins and guiding pin holes, avoiding shock loads on hooks and latches, and ensuring stable separation of the spacecraft.

At the final stage, the active spacecraft fully retracts from the passive node, leaving the transfer tunnel hermetically sealed by pre-installed seals. Monitoring systems verify the absence of mechanical contact between elements and confirm correct disconnection of connectors. Both modules are now fully autonomous and ready for independent maneuvers, docking with other spacecraft, or autonomous operation.

5.2. Off-Nominal Undocking

In certain cases, undocking may be required outside nominal procedures due to emergencies, actuator failures, or unexpected control commands. Such off-nominal undocking is critical for crew safety, preservation of docking mechanisms, and continued usability of the docking interface.

During off-nominal undocking, the soft capture system with the automatic secondary release mechanism reacts first. It safely separates the active node from the passive node without damaging guiding petals, latches, or strikers. Spring cables of the kinematic supports generate controlled repulsive motion, preventing shock loads. Sensors record the disconnection and relay the information to the control system, completing the primary stage automatically.

Next, the hard capture hooks are disengaged synchronously. Elastomer seals relax, allowing safe exit from the hermetic tunnel. Power and data plugs disconnect correctly due to self-alignment mechanisms, preventing contact damage even with minimal residual offsets. Concurrently, the hermeticity of the transfer volume is verified, and internal pressure is equalized with the atmosphere of one of the spacecraft.

Following the activation of secondary release mechanisms, a re-docking attempt requires inspection of latches, hooks, and connectors before reuse. This safety protocol ensures high reliability while preventing immediate re-engagement without inspection.

The off-nominal procedure is executed in the following sequence:

1. Activation of the soft capture system and secondary release mechanism.
2. Release of active and passive hard capture hooks.
3. Disconnection of power and data plugs.
4. Verification of hermeticity and pressure equalization in the transfer volume.
5. Inspection of system elements to ensure readiness for subsequent docking.

Implementing this procedure within the docking control system increases overall spacecraft reliability and adaptability, ensuring crew safety and minimizing the risk of damage to mechanical elements during emergency undocking maneuvers.

6. Application of graph theory to the modelling of the hexagonal parallel manipulator

Graph theory is a branch of mathematics that examines structures composed of vertices (nodes) and edges (connections), which represent relationships between elements. In engineering, graph models help formalize the architecture of systems and facilitate their structural analysis and optimization.

The hexagonal parallel manipulator can be modelled as a directed graph (Fig. 3), where:

- The central vertex corresponds to the moving platform (soft capture system);
- Peripheral vertices represent the base attachment points of the six legs;
- Each leg is represented by a chain of edges, modelling its joints and actuators.

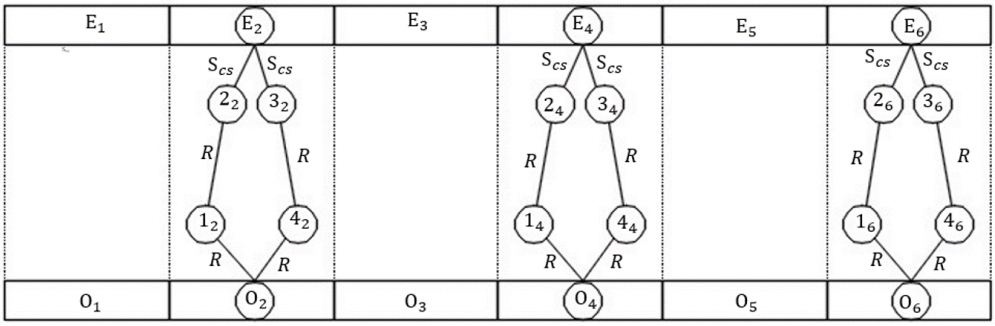

Fig. 3. Design of links of hexagonal Euclidean manipulator by using graph theory (Source: Authors' own work)

This modelling approach allows for:

- Analyzing the transmission of forces and motions within the system;
- Identifying structural redundancy;

- Applying optimization algorithms to improve configuration and control.

A planar graph representation was constructed for all six legs of the manipulator, providing a clear and formalized description of its internal structure.

7. Conclusions

This work presents a comprehensive development and analysis of a hexagonal parallel manipulator for spacecraft docking and undocking. The integration of Euclidean polyhedral geometry with a parallel kinematic structure and the novel RRS_{CS} legs provides high spatial mobility, precise relative positioning, and robustness against residual angular velocities and geometric misalignments. The two-system architecture, comprising soft and hard capture systems, allows controlled step-by-step docking, ensuring reliable mechanical connection, interface sealing, and the transfer of energy and data between modules.

The developed docking and undocking procedures, including emergency scenarios, demonstrate the capability for safe and controlled separation, minimized risk of damage, and the potential for repeated interface reuse. Formalizing the kinematic structure using graph theory provides an analytical tool for structural assessment and system optimization.

The proposed approach combines geometric and kinematic innovations, delivering high reliability, repeatability, and flexibility in automated orbital operations. Although the concept is currently at an early stage and has not yet been implemented in practice, the analysis confirms the potential of parallel manipulators for future spacecraft docking applications.

Abbreviations

R : Revolute
S_{cs} : Sphere in cylinder slot
IDSS : International Docking System Standard

References

Alizade, R. (2019). Structural Synthesis of Robot Manipulators by Using Screw with Variable Pitch. *Universal Journal of Mechanical Engineering*, 7(2), 50–63. http://doi.org/10.13189/ujme.2019.070203

Alizade, R. I., & Samedzade, J. A. (2021). A Hexagonal Interface Spacecraft Docking System. *Robotics & Automation Engineering Journal*, 5(2), Article 555659. http://doi.org/10.19080/RAEJ.2021.05.555659

Alizade, R. I., Azimov, K. S., & Samadzade, J. A. (2023). Structural Synthesis of Euclidean Parallel Robot Manipulators of Spacecraft Docking System. In: Karakoc, T.H., Letnik, T., Marksel, M., Ekmekci, I., Dalkiran, A., Ercan, A.H. (eds). *Emerging Trends in Electric Aviation* (ISEAS 2022), Springer, Cham. https://doi.org/10.1007/978-3-031-37299-5_15

National Aeronautics and Space Administration. (2016). *International Docking System Standard (IDSS) interface definition document (IDD), revision E*. NASA Technical Reports Server. https://ntrs.nasa.gov/api/citations/20170001546/downloads/20170001546.pdf

Sholanov, K. S. (2021). *Parallel Manipulators of Robots: Theory and Applications*. Springer Cham. https://doi.org/10.1007/978-3-030-56073-7

Syromyatnikov, V. S. (1984). *Стыковочные устройства космических аппаратов* [Docking devices of spacecraft]. *Машиностроение* [Mechanical Engineering]. Сыромятников В. С. Стыковочные устройства космических аппаратов (DJVU)

National Aviation Academy

International Journal of Transportation Research and Technology

e-ISSN: 3079-6075

DOI: 10.71108/transporttech.vm03is01.03

Research Article

Blockage and Outage of Aircraft Navigation System: An Implication and Solution for Sustainability of Aviation

Tapdig Imanov*

European Leadership University, Famagusta, TRNC

Timescale of article

Received: 10 October 2025
Accepted: 29 October 2025
Published: 25 June 2026

Corresponding author

Tapdig Imanov
timanov@yahoo.com

Keywords

Global Navigation Satellite System, Aircraft Systems, Jamming, Interface, Trajectory, Radio Frequency Interference

Cite this article as:

Imanov, T. (2026). Blockage and Outage of Aircraft Navigation System: An Implication and Solution for Sustainability of Aviation. *International Journal of Transportation Research and Technology*, 3(1), 26-44.
DOI: 10.71108/transporttech.vm03is01.03

Abstract

Recently, there have been an increasing number of blockages and outages of Global Navigation Satellite Systems signals for civil aircraft by applying jamming, spoofing, and interference modes that threaten flight safety. The purpose of this study is to investigate the impact of intentionally interference of satellite signals, and its negative implication on systems and flight path involved aircraft The methodology considers various applications for countermeasures that affect aircraft navigation systems while GNSS signals are missing. The practical implications demonstrate that, even if all satellite navigation signals and radio navigation systems are turned off, alternative aircraft equipment is able to prevent disasters. Low Range Radio Altimeter interfacing with a Ground Proximity Warning System is the best and most reliable implemented technology to warn and avoid the threat. Modern developments allow the use of countermeasures with Quantum, AI-Powered, and Geomagnetic navigation system technologies to provide stable flight sequences, ensuring the safety of aircraft and passengers.

1. Introduction

Modern life is enabling multiple innovative technologies in various sectors and countless industries, including air transportation. For air transportation systems, the critically important components are the use of Global Navigation Satellite Systems (GNSS), such as GPS, Galileo, GLONASS, and Beidou, for air traffic management and route optimization. Growth of the GNSS system provides accurate navigation, enhanced communication, and due timing. However, recent trends have observed that GNSS technologies are vulnerable to external intrusion and face regular threats from interference using jamming and spoofing. Using jamming on GNSS signals creates radio frequency interference that is similar to the GNSS signals themselves, which can overpower them and lead to a loss of positioning, navigation data, and timing. The effectiveness of a spoofing attack differs from jamming with its sophisticated implications. Applying fake signals in GNSS operations is directly linked to selected object navigation receivers, deceiving them with transmitted radio frequencies while manipulating calculations of incorrect positions and fluctuating a time scale. Interference with the aircraft navigation system leads to an outage of the Flight Management System (FMS), the terrain database of the Traffic Collision Avoidance System (TCAS), the Ground Proximity Warning System (GPWS) and interconnected avionics devices. Meanwhile, the loss of GNSS signals affecting the whole navigation system of the aircraft causes operational malfunctions, disrupts signal interfaces, and creates ramifications for safety risks and accidents. GNSS is an integral part of the modern global airport systems. Jamming and spoofing GNSS signals near airports can compromise and disrupt overall operations, mostly causing imprecise approaches and missed landings, leading to flight delays. As stated in the European Aviation Safety Agency (EASA, 2024) report, since the beginning of 2022, there has been observed significant growth in jamming and spoofing the GNSS. The published EASA Safety Information Bulletin (EASA SIB 2024-02R3) indicates RFI-affected geographical areas and airports throughout the world (Table 1).

Table 1. RFI Areas and Regions (adopted from IATA, 2024)

The Black Sea Area	**LTBB, LTAA, UGGG, LRBB, LBSR, UDDD, UBBA**	**Istanbul, Ankara, Tbilisi, Bucuresti, Sofia, Yerevan, Baku**
The Middle East: Southeastern Mediterranean Area	LCCC, OLBB, OSTT, LLLL, OJAC, HECC, LGGG, ORBB, OKAC, OBBB, OIIX, HLLL.	Nicosia, Beirut, Damascus, Tel-Aviv, Amman, N-E Cairo, Athina, Baghdad, Kuwait, Bahrain, Tehran, Tripoli
The Baltic Sea Area	UMKK, EFIN, EETT, EVRR, EYVL, EPWW, ESAA	Kaliningrad, W-Helsinki, Tallin, Riga, Vilnius, E-Warszawa, S-Sweden
Eastern Europe Area	LZBB, LHCC, LUUU.	Bratislava, Budapest, Chisinau
North Atlantic Region	BIRD, NUUK	Icelandic, Greenlandic
SAM region	SAEF, SARR, SBBS, SBRE	Ezeiza, Resistencia, Brasilia, Recife
MID-Asia region	VIDF, VABF, VYYF, ZPKM	Delhi, Mumbai, Yangon, Kunming
Africa region	FACA, DNKK	Cape Town, Kano

The recently analyzed data, relying on the Network of Analysts and open sources, has concluded that the RFI interference to GNSS jamming and/or spoofing tends to further increase by its severity and intensity. The effect of the RFI on GNSS is not limited to the flight information regions (FIR) emphasized in EASA's SIB. This document is a valuable motivational resource to assist IATA airline members in determining the operational risks associated with the weakening of onboard GNSS-related functionality. According to the International Air Transport Association (IATA, 2024) analysis over the past year, shows that the GNSS outage trend in the first six months of 2024 (GPS signal disruptions per thousand of flight hours) has increased significantly compared to 2023, as demonstrated in Fig. 1.

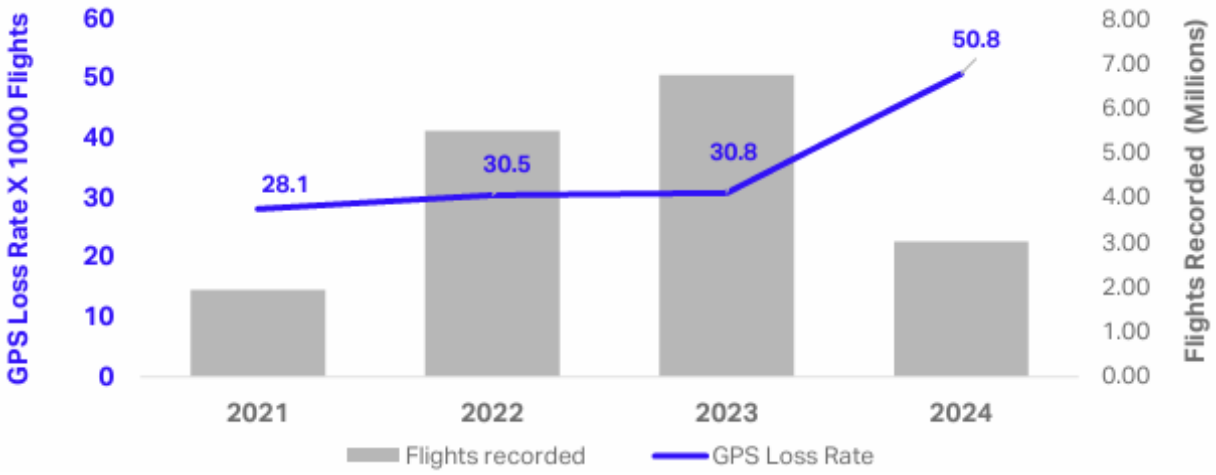

Fig. 1. GNSS signals loss records (IATA, 2024)

Alongside EASA publications, the IATA (2024), in the frame of the Flight Data Exchange (FDX) program, evolved the activity, revealing RFI hotspots in other regions. The results identified increasing GNSS outages between 2021 and 2024, posing a safety risk across wider geographical areas, Fig. 2. It is notable to highlight that the report reflects real aircraft-recorded data and is not based on statistical analysis or predictions. Thus, FDX continues to provide an updated geographic identification of the RFI hotspots, where threats to flight safety exist.

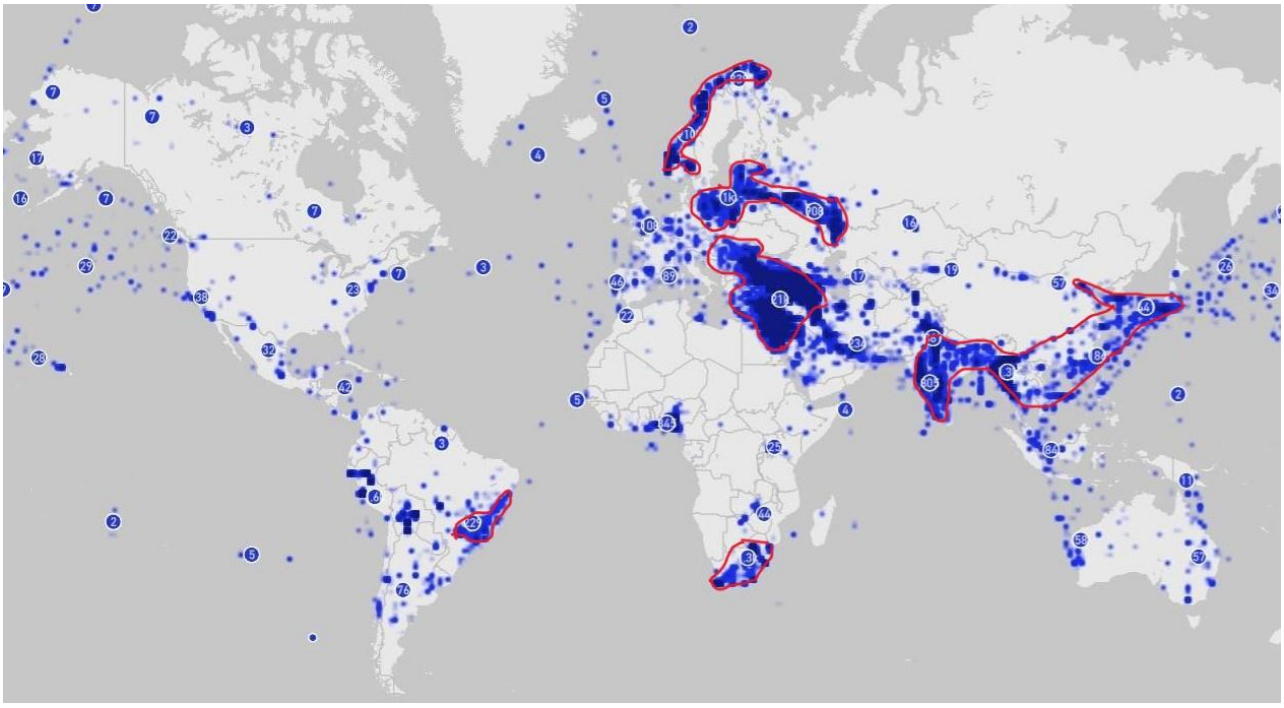

Fig. 2. GNSS RFI Recorded Events between January and June, 2024 (IATA, 2024)

It helps determine the safety controls for member airlines in order to effectively mitigate GNSS interference risks. Because airlines periodically experience the effects of RFI on GNSS in various flight phases, these effects lead to rerouting or diversions of their flight paths. Additionally, the nearby areas covered by RFI jamming GNSS are a potential reason for degradation of aircraft communication, navigation, and surveillance (CNS) systems. To mitigate the limitations of GNSS signal transmission, the International Civil Aviation Organization (ICAO, 2003) has proposed an Automatic Dependent Surveillance-Broadcast (ADS-B) surveillance system that uses onboard aircraft navigation systems to obtain accurate aircraft position. Implementation of the system is intended to assess and support ATC services, particularly focusing on separation and airspace safety (Ali et al., 2015).

However, the challenge of GNSS jamming and spoofing, either intentional or unintentional interferences, delimited normal operation of the aircraft and under the present conditions (NordSky, 2024), GNSS outages impact degraded abilities with ramifications of (i) Loss of waypoint navigation, (ii) Area Navigation (RNAV) approach capability, (iii) inability to perform required navigation performance (RNP) operations,(iv) triggering of terrain warnings, possibly with pull-up commands, (v) scattered aircraft position on the navigation display (ND), (vi) loss of ADS-B functionalities,(vii) failure of time reference, and (viii) Airspace infringements and route deviations (ICAO, 2022).

The purpose of this study is to investigate the impact and implications of the loss of satellite signals on systems and flights of involved aircraft. Limitation of the study a lack of publications describing real situations and events with significant fatal implications involving RFI. Most studies rely on simulations or controlled lab environments which arises the practical, technical, and operational application is prevented being fully effective investigations.

Due to even modern aircraft avionics systems lack real-time detection capabilities of jamming and spoofing, they are unable to precisely alert crew members (Radoš et al., 2024). However, most avionics equipment is able to recognize the loss of GNSS signals (jamming) and struggles to detect spoofing; consequently, crew alerts are basic in the form of “GPS signal lost” or “NAV accuracy degraded,” but not a clear detection warning. GNSS jamming and spoofing affects not just navigation but also dependent systems like ADS-B, CPDLC, TAWS, and EGPWS, yet, literature often treats these systems in isolation.

Therefore, the current study will make a significant contribution to airlines' activities as a tool to pre-emptively reroute or prepare crews for high-risk zones upon RFI attack. Additionally, the validated outcomes fill the gap in scientific literature, introducing the reliability integration of independent landing and warning systems for application in the future researches.

2. Literature Review

One of the important sources of reference signals for synchronization and provision of navigation and positioning services is GNSS. For aircraft navigation systems and accurate positioning, the GNSS application is the best source of reference signals for the synchronized aircraft radio frequency (RF). However, due to the increased provision of services and the use of satellite navigation systems, there are an increasing number of threats and risks, accompanied by harmful interference targeted these systems (Psiaki et al., 2016; Hexagon, 2025). Jamming and spoofing attacks expose navigation systems to security risks (Wu et al., 2020), which negatively affect flight safety. Humphreys et al. (2008) developed a counter-measurement system for spoofing attacks performed on a commercial standard receiver and successfully tested it; later, the strategy to detect spoofing attacks on cryptographically protected GNSS signals was presented in the studies of Humphreys (2013) and Meng et al. (2022).

Altaweel et al. (2023) argue that an important consideration for effective detection of intrusion in GNSS signals and to maintain countermeasures and integrity affected by spoofing and jamming attacks consists of precisely differentiating between authentic and non-authentic signals. Most of the latest literature reviews and scientific research emphasized the detection and localization of GNSS RFI interferences based on ADS-B data. However, to continuously support an acceptable level of safety in aviation, it is necessary to detect the GNSS jamming promptly and secure the incident decisively.

For that reason, existing literature described various detection methods for jamming and spoofing aircraft and GNSS aeronautical navigation systems, which concluded only on strategies and roadmaps (Felux et al., 2024). GNSS intrusions, using radio frequency interference (RFI) and their impact on passenger flight aircraft were conducted in several analyses. Data from ADS-B and avionics, collected by the airline's team for monitoring flight performance for the specific flights that showed warnings to alert the crew about RFI effects on GNSS, have been examined by many researchers (Scaramuzza et al., 2015; Darabseh et al., 2019; Jonáš & Vitan, 2019; Lukeš et al., 2020; Liu et al., 2020; Liu et al., 2021; Murrian et al., 2021; Osechas et al., 2021; Fol & Felux, 2022; Liu et al., 2022; Figuet et al., 2022; Joseph et al., 2023; Blois et al., 2023; Felux et al., 2024).

On the other hand, to solve the current issue related to RF interference to GNSS signals, there is a demand to find out effective countermeasure technology and optimal preventive methodologies. The studies by Qiao et al. (2023) and He et al. (2024) have suggested focusing on the development of technologies for satellite navigation interference monitoring. Conversely, the study by Radoš et al. (2024) provided a detailed and organized overview of ways to detect interference from both GNSS jamming and spoofing combinations. Therefore, the study's

conclusion underscores the significance of emphasizing machine and deep learning methods. Machine learning methods are used to detect and classify the signal to prevent interference where such attacks are more common. In addition, it is able to initiate processing methods of signals, as well as the application of positioning techniques.

Ghanbarzade & Soleimani (2025) have drawn attention to the limitation of traditional methods for RFI analysis, and the idea is supported by studies by Zidan et al. (2020) and Issam et al. (2020), relying on predefined threshold values, which are predicted not to be effective in all scenarios and are susceptible to false identifications of alarm. In contrast, Bose (2021) and Nayfeh et al. (2023) consider that the use of machine learning (ML), deep learning (DL), and artificial intelligence (AI) methods in the investigation of GNSS interference enhances detection by analyzing patterns in large datasets of known signals. These contemporary techniques are able to improve accuracy detection over time by adapting to complex scenarios (Zidan et al., 2020). Albeit, recent achievements reveal a notable shortcoming in detecting jamming and spoofing attacks in GNSS while using ML and deep learning techniques. As far as most studies are concerned, they focus exclusively on either spoofing or jamming, neglecting the simultaneous occurrence of both threats, which limits detection robustness (Zidan et al., 2020; Bose, 2021; Nayfeh et al., 2023; Ghanbarzade & Soleimani, 2025). Meanwhile, ML and DL have the potential for adaptation in major research concentrating on specific systems like GPS or GLONASS, whose implementations remain applicable for validation of RFI detection methods (Aissou et al., 2021; Jullian et al., 2022).

Sustainability of satellite signals and airspace information, particularly while transmitting via quantum sensors in quantum optics, has contributed important progress in developing quantum communication networks (Pirandola et al., 2020). Atomic clocks, another significant application of quantum sensors, are essential for GPS and telecommunications that require exact time measurements in synchronizing worldwide communication systems (Ludlow et al., 2015). The GPS technology, which has a tremendous opportunity for both civilian and military navigation, relies on the accuracy of these quantum sensors to provide location data (Wineland & Dehmelt, 2021). The demonstration of the precision and sensitivity of quantum optics, atomic clocks, and magnetometry may prove advantageous in enhancing precision navigation and timing (PNT), as it can provide navigation locations that are independent from GPS operation. Traditionally, these systems have relied strongly on GPS technology, but GPS comes with inherent vulnerabilities such as signal jamming, spoofing, and signal degradation. These limitations create a critical need for more resilient, autonomous, and accurate navigation systems. Quantum sensors, particularly quantum-based inertial sensors, are emerging as the solution to these challenges, offering unprecedented precision without reliance on external signals like GPS (Abraheem et al., 2025).

3. Method

The current paper uses a qualitative research method, therefore the methodology uses various significant theoretical scientific interpretation from different authors with similar occured events which is important to involve multiple literature sources. The collected data contributes to accomplish to solve the research question concerned with observed object. The analysis method consists of available data for conducting in the sample of the flight J2 8243 to evaluate the RFI influence on civil aviation aircraft. RFI generation has a comprehensive dataset that includes examples of GNSS signals under various conditions, such as normal operations, jamming, spoofing, and combined threats. The collection of the data was achieved utilizing real-world GNSS signal data generated from various sources and a simulation tool. Additionally, the Digital Flight Data Recorder (DFDR) and ADS-B data sets were retrieved and processed for use in the subsequent illustration of the geographical area of interest subject to RFI and to identify differences between the fake and the actual flight path of the specific aircraft. Finally, the study describes the observed trends and actual parameters obtained from a scheduled flight conducted on an Embraer aircraft through an area during known RFI occurrences.

4. Resul and Discussion

4.1. Impact of RFI on aircraft operation experiencing jamming and spoofing

Updated statistical data concerning GNSS disruption and related incidents highlight the growing challenge of GNSS interference in civil aviation. Eurocontrol (2021) estimates that 38.5% of European air traffic destinations operate across regions regularly affected by RFI and 5% of air traffic requires special assistance due to GNSS interference. A significant part of the information reported by the flight crew emphasizes that without backup navigation systems, the aircraft are experiencing the most severe disruptions (Fol & Felux, 2022). Furthermore, the ADS-B data analysis validated the substantially higher number of GNSS jamming incidents in 2024 (Felux et al., 2024). The result of an investigation by OPSGroup (2024) has revealed a catastrophic trend, reporting a 500%

increase in GPS spoofing incidents. Civil Aviation Spoofing Surge has an average of 1,500 flights per day that are intensively affected around conflict zones. These disruptions over the airspace of Israel, Lebanon, and Russia forced aircraft rerouting and posed risks to flight safety.

Referring to EASA (2023) SIB as per Table 1, there are some notable instances of aircraft experiencing jamming and spoofing GNSS signals. The rise in jamming and spoofing is particularly active in regions experiencing geopolitical tensions. However, the incident that occurred in Mexico City (Buesnel & Holbrow, 2017), where pilots reported GPS signal loss and receiver outages while on final approach to the international airport, is suspected to be caused by illegal jamming devices. A GPS jammer installed near Harbin Airport, China, in 2019, disrupted aircraft navigation, forcing authorities to intervene. In March of the same year, there were reports of "circle-style" GPS spoofing in Tehran, the capital of Iran (Buesnel, 2020), which was not a military area. Due to the conflict since 2022, GPS jamming was widespread in Ukraine, affecting civilian aircraft, while disruptions complicated navigation and communication for pilots. Interference affected GPS in several NATO exercises, impacting the aviation sector in Estonia, Latvia, and Lithuania (Garcia et al., 2024; Pultarova, 2025). The Middle East, Eastern Europe, and the Mediterranean and Black Sea regions also reported GPS interference incidents, with aircraft flying over experiencing unreliable ADS-B signals. Some flights had to be tracked using Multilateration (MLAT) instead of GPS, causing aircraft to deviate up to 80 nautical miles from their intended flight paths. Pilots had to rely on radar vectors from air traffic control (ATC) to navigate safely (OPSGroup, 2024). The Fig. 3 is representing occurrence examples over Mediterranean and Black Sea regions RFI affected aircraft an incorrect diversion trajectory.

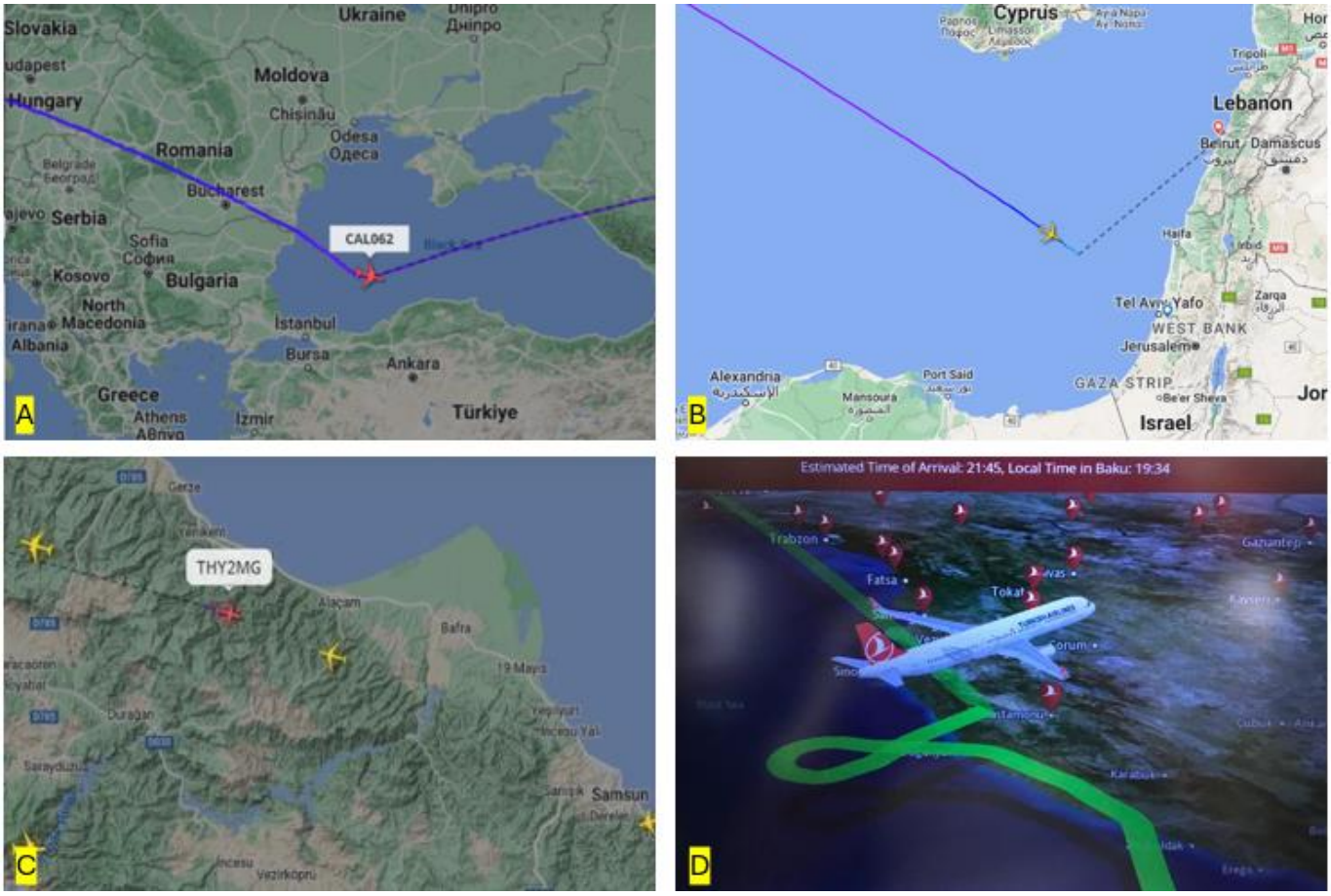

Fig. 3. (A, B, C, D). Aircraft affected by RFI attacks over the Mediterranean and Black Sea regions (Sources: A and B Lomas, 2025; C and D: Author's own work)

Can GPS jamming happen accidentally, especially if the aircraft navigation equipment receives an authentic GNSS signal? - Occurs only if corresponding multi-mode receivers (MMRs) fail or the interface between electronic systems becomes inoperative for technical reasons. Once increasingly, research, manufacturer information letters, and authority awareness reports are seeing it cause deliberately, in an illegal way, rendering the devices used in air vehicles. GPS jamming is illegal, excluding conflict regions, where possible to apply. Using the modern

Multilateration (MLAT) technique, Flightradar24 can track flights experiencing GPS jamming and spoofing in the region of intrusion. Fig. 3(A) shows the Boeing 777 China Airlines flight C162 over the Black Sea near the northern coast of Turkey being tracked via MLAT, dictated to weak and unreliable GPS and ADS-B signals in the crossed area. Fig. 3(B) is a similar incident in which United Airlines Boeing 787-10 flight UA84 (New York-Tel Aviv) in March 2024, which was a victim of GPS spoofing, leading to an incorrect maneuver plotted for the aircraft's flight path (Lomas, 2025). In June 2024, again over the Black Sea, the Turkish Airlines flight TK 334, Istanbul-Baku, (Fig. 3(C)) Airbus A321 spoofing of GPS signals, resulted in the aircraft appearing in places that it should not appear (Fig. 3(D): taken from the passenger display unit by the author during the given flight).

Analysis of the particular aircraft types or families to identify their vulnerability affected by jamming and spoofing, in short, on a global scale against RFI attacks will lead to similar results. The implication of such an intrusion action on GNSS usually impacts appropriate receivers providing navigation systems, either Boeing or Airbus, as well as other regional and business jet aircraft. The consequence is the disruption of functionality in most flight management systems, including GPS, FMGC, TCAS, GPWS, MMR, FMS, and others. Airbus (2019) has released an in-service information, (bulletin) for Airbus aircraft in the event of GNSS loss and interference. This information letter includes announcement messages on the navigation and alerting displays, which serve as cockpit and system effects to significantly increase flight crew awareness. However, Boeing and other types of aircraft design a similar warning effect, albeit with different display names and character of messages. Description of the common cabin and system display effects and functions are containing the functional and system effects corresponding to cockpit effects on the PFD, ND, ECAM (EICAS) by alerts/status/ INOP systems indications with voice messages.

The incident employing jamming GPS signals potentially disrupted and affected navigation, communications, and surveillance systems on Azerbaijan Airlines Flight J2-8243 on 25 December 2024 (Summers, 2025; Domogala, 2025). Sequentially, this flight was affected by GPS spoofing near western Russian airspace, misleading aircraft into reporting incorrect positions, thereby leading to dangerous miscalculations of actual flight coordinates. Pilots lost GPS-based guidance and needed to rely on alternative navigation methods using radionavigation aids. The Grozny ATC tower's assistance with vectoring during the procedure did not promise a solution for the proper approach and landing. The situation resulted in increased cockpit workload and stress for pilots, particularly in low-visibility conditions in the airspace where RFI was used. At the final stage of descents, ADS-B transmitted the wrong navigation coordinate; however, the aircraft has flown near Grozny airport which happens in the situation of electronic warfare interference. The next scenario is revealing the exact and clear impact of spoofing on the real aircraft, which experienced, during the guidance to the airport destination, an unexpected case of occurrence that nearly caused a collision with the mountain top. Following ATC instructions, the aircraft takes the wrong course due to incorrect calculations of the navigational positions, redirecting the aircraft in the opposite direction. Meanwhile, the flight crew is unable to define their accurate location in the airspace contaminated with fake signals.

During the transmission of the GNSS signals, it is important that the waves' spatial variety and capture phase by the aircraft receivers reflect the different directions of arrival (DoA) of the derived signals (Rothmaier et al., 2021). Under standard conditions, these metric angles need to be different for each active satellite; usually, three are necessary for aircraft needs. Consequently, an aircraft antenna receives signals from three satellites distributed across the entire sky for position calculation. However, signals generated from a spoofer will arrive from a single direction. In some cases, if the RFI equipment has an enhanced attack capability, it will transmit from a few directions using multiple transmitting antennas mounted. Then all signals will be transmitted maliciously from a single antenna, and aircraft displays will show a false alert and a fake position. The spoofing detection, based on measured DoAs, is shown in Fig. 4 for the concept of three satellites. Angles/directions of signals i and j are different when coming from the authentic satellites (black arrows) but nearly identical when coming from a single spoofing source (red arrow).

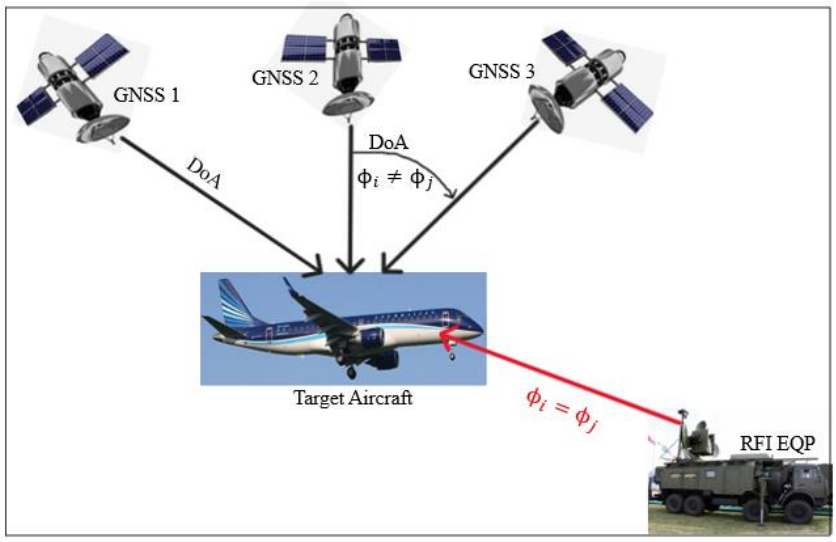

Fig. 4. Authentic diverse signal directions from GNSS and spoofing signal directions from RFI equipment (Source: Author's own work)

The difference in signal angles or directions between authentic satellites and a spoofing source can be expressed using spatial processing techniques. One useful equation for detecting spoofing based on direction of arrival (DoA) can be derived from the Neyman-Pearson Likelihood Ratio Test (LRT) that is independent of prior probabilities (Van Trees, 2001). The general hypothesis test is presented in Equation 1.

$$\log \Lambda\,(y) = h_0^T R^{-1} y - \frac{1}{2}(h_0^T R^{-1} h_0) \tag{1}$$

Whereas;

log Λ(y) - conditioned on (y)

Λ (y) - is the likelihood ratio test statistic

y – represents the observed measurements of signals of DoA

h_0 – represents the expected difference between the DoAs of signals from authentic satellites under null hypothesis (H0).

R - is the covariance matrix of the original DoA measurements.

The study by Rothmaier et al. (2019a) first used a new version of a hypothesis iteration algorithm from Neyman-Pearson and found its efficiency and effectiveness to identify groups of fake satellites, even when there was weak multipath interference. Later research conducted by Rothmaier et al. (2021) enhanced the development of the previous study, considering necessary tests for reasonable performance under real-world conditions. Presented flight test data and data collected during a government-sponsored live spoofing event to support the validation of the theoretical derivations. Recognizing the uncertainty associated with using noisy measurements to determine the presence of a spoofing attack, the new framework study approaches the decision problem as a statistical hypothesis test. The null hypothesis is introduced as ($H0$), representing the nominal situation without spoofing and the alternate hypothesis, considered as ($H1$), represents a spoofed situation attack on the object of interest. Using the formulated hypothesis in accordance with equations created by authors, which derives the formula, the distribution of the statistic likelihood ratio test [log Λ(y)] was conditioned on the observed measurements of DoA signals under nominal and spoof conditions. The threshold (γ) is found by solving the quantile function or inverse cumulative density function (cdf) of the random variable log Λ(y) conditioned on $y \sim H0$ for $PFAmax$, Equation 2.

$$\gamma = \frac{1}{2}\,\bar{\phi}^T R^{-1} \bar{\phi} \; + \; \Phi^{-1}\left(P_{FA_{max}}\right) \sqrt{\bar{\phi}^T R^{-1}\,\bar{\phi}} \tag{2}$$

γ - Detection threshold

Φ^{-1} - Quantile function

$\bar{\phi}$ - arc ($\bar{\phi} = \Delta\theta$) between the two and more satellites normalized by the measurement standard deviation (σ) for different maximum false alert probabilities.

$P_{FA_{max}} -$ *is* the false alert probability or statistical significance level

The optimization problem is solved using the result of the detection threshold (γ), where Φ^{-1} is the quantile function or inverse cumulative density function (cdf) of the Standard Normal distribution.

Application of the theoretical base of the study by Rothmaier et al. (2021) is the best methodology example to check the validity on the aircraft affected by RFI on flight J2 8243, as demonstrated in Fig. 5.

Fig. 5. RFI activation result on the aircraft flight J2 8243 trajectory paths (need to place on horizontal layout) (Source: Author's own work)

Under nominal conditions, the normalized azimuthal DoA measurements from GNSS are multipath, both in flight and after the descent stage upon entering Russian airspace. The flight profile includes descents with a heading of 291 degrees and turns with various banks. The data collection retrieved from the DVDR and ADS-B report for the given flight provides a detailed description of the event. The black line shows a standard normal flight trajectory according to the flight plan to the desired destination assigned to Grozny airport. After the first step impacted by jamming, the aircraft lost both GPS functions; therefore, the onboard navigation units measured the erroneous location. Activation of the spoofing (marked with a red line from RFI EQP) generated identical DoA signals that misled the aircraft. In turn, having two circles over the Grozny region, the aircraft was redirected to the fake destination; meanwhile, the ADS-B transmitter indicated fake positions. The over bounds of the measurement error ensure a fake navigational location and behavior of the aircraft 60 km away from the actual position, which supports the likelihood of the false alert probability and the multipath restriction strategy (Rothmaier et al., 2021).

All satellite signals spoofed from the same transmitter, makes the situation complicated and more dramatic, means that all signals come from the same direction under spoofed conditions. Due to violations of the receiver, it cannot lock emitted signals by the spoofer and still assumes that it is tracking some authentic satellite signals. When the attacker uses multiple antennas to transmit fake signals from multiple sources, it reduces the detection capability of GNSS signals (Rothmaier et al., 2019b) by the aircraft navigation receivers. The intrusion to GNSS waves by using RFI may occur, either unintentionally in result of failure caused by instrumentation or communication systems (Berglund et al., 2011; National Academies of Sciences, Engineering, and Medicine, 2023) or intentionally, mainly observed in conflict zones, which may limit use of GNSS signals or prevent for their intended purpose. Actually, the intentional RFI is caused by harmful transmitters, where sending out noise at the carrier frequency (jamming) or false signals (spoofing), converted to pseudo-random noise codes to trick a receiver into calculating a false position (Chew et al., 2023).

4.2. The available prevention tools and potential solution to prevent application of RFI to GNSS and aircraft

Many scientific investigations, modern technology, various experiments conducted by scientific research institutes, and special laboratories have not yet given positive results for the protection of aircraft from the introduction of jamming and spoofing. Nevertheless, as numerous reports of aviation authorities and bodies studying this problem show, attacks on civilian aircraft using RFI increase year after year. Society and the relevant industries have not yet received any kind of protection warranties for solving this problem. Additionally, the proposed detection tools and methods are only intended to monitor and identify the source of false signals generated against GNSS operations.

The latest developed receivers and software to track the flights advantageously use the Multilateration (MLAT) method, which positions accuracy near ADS-B capability, with an error margin of 10-20 meters. However, the main limitation with MLAT tracking is aircraft altitude, that the signal from the lowest altitude below between 5,000 and 10,000 feet decreases and the aircraft is no longer displayed on the map (Petchenik, 2025). Besides airspace alerts, some researchers have proposed long-term ways to mitigate GNSS interference, such as Spatial Processing and GNSS-Band Radio Interference on Operational Avionics (Rothmaier et al., 2021; Osechas et al., 2022), Automatic Gain Control (AGC) monitoring (Meng et al., 2022), Carrier-to-Noise Density Ratio (C/No) monitoring (Hegarty et al., 2018), the Cross Ambiguity Function (CAF) monitoring (Zarrinnegar et al., 2023), and using Navigation Message Authentication (NMA) (Götzelmann et al., 2023). Finally, Safran Electronics & Defense's sector is currently working on a new device, developing the Interference Detection Mitigation (IDM) algorithms, enabling it to detect GNSS interference and immediately switch to a resilient, autonomous source, ensuring mission continuity (Safrangroup, 2025).

The risks associated with spoofing and jamming attacks are often emitted by military bases and have an omnidirectional range. Affecting civil aircraft even at high altitudes could threaten passenger safety. Safran's solution for flight safety is developing an ultra-compact, highly reliable, and powerful hybrid inertial navigation system (INS) that can be integrated into civil aircraft to ensure precise, safe navigation (Safrangroup, 2025). The most powerful mitigation against RFI, particularly for suppression jamming and spoofing is a dynamic sensor data fusion system. The dynamic sensor data fusion system is designed for suppression, jamming, and spoofing and is the most expensive option; however, it interfaces sensors for GNSS and IRS, which contributes to system sustainability. Most commercial aircraft categories are equipped with IRS, ensuring reliable signal transmission and providing accurate position data even during periods of GNSS jamming or spoofing (Dovis, 2015; Fernández-Hernández et al., 2019).

4.3. IRS/INS solution for GNSS RFI

Based on the data analysis, it's safe to assume that IRS/INS plays a crucial role in maintaining the functionality of aircraft navigation systems, whether due to jamming, spoofing, or other disruptions when GNSS signals are interfered with. Relying on the high reliability of modern IRS systems, new-generation aircraft are often designed to combine IRS with GNSS to enhance the accuracy of navigation even when satellite signals are unavailable for any reason. The IRS is, by the modern operational configuration, at a significant advantage, even if GNSS data do not support the combined functions.

- Independent Navigation: Operates independently, calculates an aircraft's position using input signals from accelerometers and gyroscopes to track the aircraft's movement from a known starting position.
- Fallback System: The Flight Management System (FMS) continues using IRS data to provide velocity and attitude data for automated flight operations and determine the aircraft's position.
- Backup Support Radio Navigation System: Within the Radio Navigation Aids range, the aircraft is able to use IRS signals to improve IRS-based navigation for VOR-DME (VHF Omnidirectional Range and Distance Measuring Equipment) operation as an alternative navigation positioning source.
- Dead Reckoning Navigation: IRS continuously estimates the aircraft's velocity and position relative to its initial location, allowing the aircraft to continue navigating using dead reckoning.
- Drift Angle Correction: Since IRS navigation is based on dead reckoning, using external sources, like radio navigation aids, corrects the positioning data due to accumulated small errors causing a drift.

The Fig. 6 represents block diagram of IRS/INS modules estimating the navigation data using components of input signals and output navigation parameters of aircraft systems.

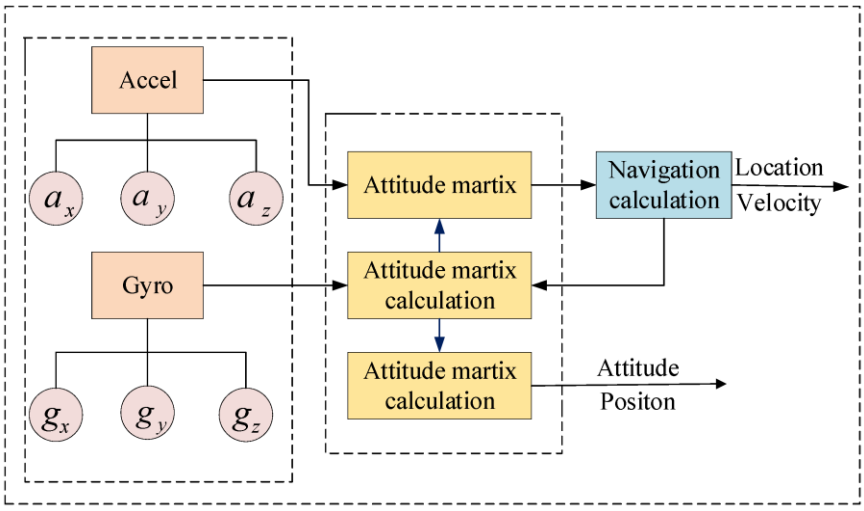

Fig. 6. Block diagram of IRS/INS modules estimating for the navigation data (Xiao et al., 2022)

An inertial system is a "self-contained" equipped in aircraft providing as additional source for navigation system. Moreover, it needs appropriate data inputs to compensate the errors, increasing position accuracy. The Inertial Measurement Unit (IMU) is the main module containing the accelerometers and gyroscopes, responsible for collecting motion data. Accelerometers detect changes to determine velocity and position while measuring linear acceleration along three axes (X, Y, and Z), integrating these data over time. Gyroscopes measure angular movement, helping determine the aircraft's heading and attitude (pitch, roll, and yaw). Unlike mechanical gyroscopes, modern IRS measurement units use Ring Laser Gyros (RLGs) or Fibre Optic Gyros (FOGs) to precisely orient attitudes. The duration and accuracy of an IRS are gradually improved depending on the quality of the integrated IMU (ICAO, 2018). Previous stabilized platforms of the IRS have a position error of 2 nm/hr; a high-performance IRS could guarantee a drift in the magnitude of 1 NM/hour (Stanisak et al., 2024), and the modern RLG in inertial systems tends to have error rates of 0.6 nm/hr, which an RNP10 requirement could be met for multiple hours.

Inputs about the present position (PPOS) are undoubtedly necessary before a flight is initialized with a known starting position to ensure accurate tracking throughout the flight, which is carried out by the Alignment System. Consequently, the Air Data Computer (ADC) is working alongside pitot-static sensors to refine altitude and speed calculations and to feed this data to the IMU. The value of barometric altitude helps stabilize the vertical velocity, meanwhile the value of True Air Speed (TAS) allows for the calculation of wind speed and direction, in order to provide initial outputs to measure the inertial altitude and drift angle. The Inertial Reference Unit (IRU) is a processor that computes the IMU input data, integrates it over time, and provides navigation outputs to appropriate aircraft systems. IRS continuously tracks heading reference and aircraft attitude (pitch, roll, and yaw), helping pilots to maintain situational awareness as well as supporting instrument-based flight. Receiving the pitch, roll, and yaw angles into the flight control unit, the IRS supplies precise orientation and movement data to the autopilot system, ensuring stable flight control and manoeuvring. Typical output data from the inertial system fed to other aircraft avionics and other systems includes:

- Magnetic Heading and Drift Angle.
- True Air Speed (TAS) and True Heading
- Ground Speed (G/S), Vertical Speed and Rate
- Latitude, Longitude, Pitch, Roll, and Yaw
- Altitude
- Wind Speed and Direction.

Finally, the Cockpit Displays (ND, PFD, and announcement devices) supply pilots with real-time heading, pitch, roll, and navigation data. A combined interface control panel and display unit is used for initializing and entering necessary latitude and longitude position data while the aircraft is on the ground. A typical IRS interface control panel is introduced in Fig. 7 (Flightvectors, 2025).

Fig. 7. A typical IRS control panel and display unit used on Boeing 757/767 (Flightvectors, 2025)

The IRS is a single navigation system that provides positioning, altitude, velocity, and timing, ensuring a reliable interface with LRRA and GPWS to avoid ground proximity collisions when aircraft navigation systems are disrupted by GNSS due to jamming or spoofing. Penetration of fake signals generated by RFI equipment on the modular avionic unit (AMU) used on Embraer 190 and Integrated Modular Avionics (IMA) installed on Boeing and Airbus aircraft for a backup (2nd set) unit is secured and is implemented through a similar concept. Either MAU or IMA architectures-nearly equivalent systems-integrate multiple functions into a single system for efficiency and flexibility. This is particularly evident in the Boeing 787 Dreamliner, where avionics functions are distributed across modular computing platforms. Airbus is implementing IMA systems in aircraft like the A380 and A350, allowing avionics applications to run on shared computing resources rather than separate dedicated units. The MAU/IMA systems, which receive signals from various aircraft sensors (except GPS), such as IRS, Low Range Radio Altimeter (LRRA or radar altimeter), and Ground Proximity Warning Systems (GPWS), interact with each other to prevent terrain collisions, as validated empirically during Flight J2 8243, relying on Low Range Radio Altimeter's transmitted data, Fig. 8.

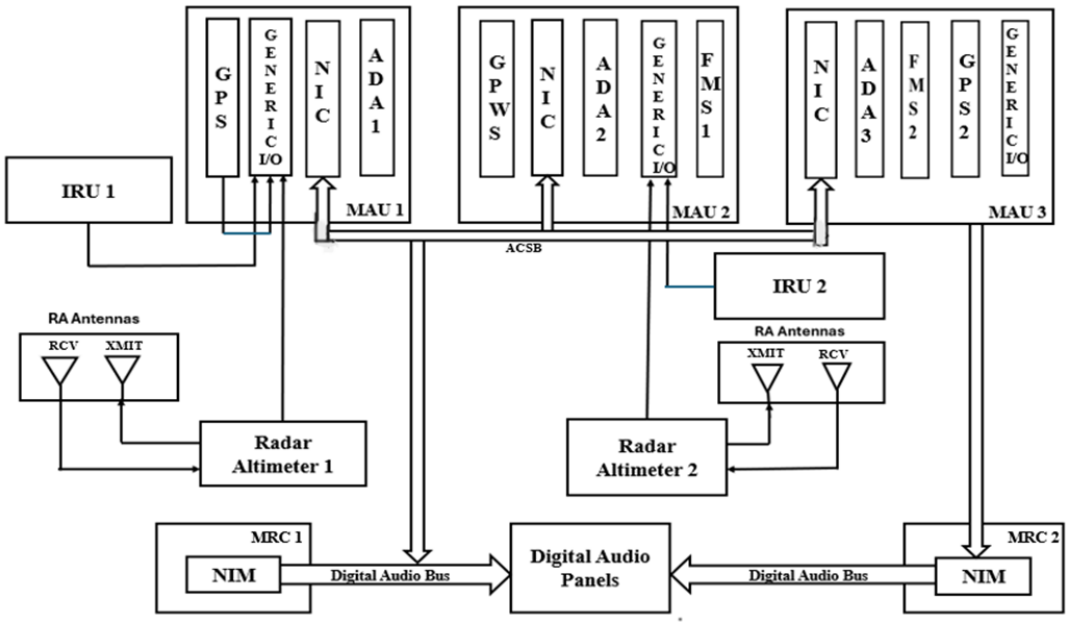

Fig. 8. Block diagram: Interface between Navigation hardware of the Aircraft Embraer E190 (System Schematic Manual (SSM), 2025)

MAU/IMA uses IRS data for precise aircraft positioning while helping in navigation and flight management as well as terrain awareness. Radio altimeter connection provides real-time altitude readings above the ground, which are used for landing approach, terrain avoidance, and GPWS alerts. In turn, the GPWS interaction processes voice message to alert pilots of potential terrain hazards. The reason why the MAU/IMA unit might not receive GPS signals is dedicated functionality, considered to secure IRS operability in the cases of RF interference against civilian aircraft to secure flight safety and passenger lives. Partitioned avionics architecture is an excellent design decision taken by aircraft manufacturers, taking into account increasing intentional intervention by jamming and spoofing and the geography of armed conflict zones. Following this incident, the European Union Aviation Safety Agency (EASA) issued a warning to airlines to refrain from flying in western Russian airspace due to heightened safety concerns. The EASA safety board notes that Russian authorities haven't provided adequate proficiency in airspace risks related to RFI implementation (Villamizar, 2025).

4.4. The incoming modern technology implementation to obstacle the RFI

AI-based and Quantum technologies are being developed to detect and mitigate RFI, including jamming and spoofing threats, particularly in GNSS. However, it does not guarantee the reliable operation of aircraft during such attacks. These AI-driven GNSS interference detection solutions enhance traditional detection methods by learning from new data and adapting to evolving threats. AI algorithms improve the reliability of GNSS-dependent applications by identifying and classifying jamming and spoofing attempts (Bong et al., 2023). The BREGO Project, funded by the European Space Agency, uses AI and machine learning to detect and mitigate GNSS threats in real time. The U.S. Space Force developed the PNT-SENTINEL Program, applying an AI-powered system that geolocates interference sources and predicts patterns of GPS jamming and spoofing (Gutierrez, 2024; Slingshot Aerospace, 2025). In addition, the study by Aftatah and Zebbara (2024) focuses particularly on the utilization of artificial intelligence (AI) approaches; thereby, the authors aim to highlight the importance of artificial intelligence in improving the security of navigation systems via intelligent systems for timely detection and neutralizing these threats. Alongside the AI-powered Navigation System to counter GPS jamming and spoofing threats, the Quantum application concept is the most considered technology to isolate the attacks in the near future. SandboxAQ develops the AQNav security geo-magnetic navigation system, leveraging AI algorithms, quantum sensors, and the Earth's crustal magnetic field in the case if GPS is unavailable or compromised. The product of the latest technology in modern systems is going to provide an all-weather and terrain-agnostic, unjammable, and spoofless navigation solution in a real-time regime (Macey, 2024).

It is expected that quantum technologies will significantly improve the positioning, navigation, and timing (PNT), especially inertial navigation. Time standards and frequency transfer (TFT) are fundamental, which provide precise timing for global navigation satellite systems (GNSS) (Jozsa et al., 2000; Giovannetti et al., 2001). Quantum technology is an emerging area that utilizes the manipulation and control of individual quanta for multiple applications and is expected to have strategic and long-term impacts. However, a precise forecast of quantum technology deployment is not possible, since the transition from the laboratory to real-world applications has not been implemented or is in progress (Krelina, 2021). The quantum technologies are anticipated to have extensive use in space. Using these technologies will lead to combined networks of quantum sensing and communications with other emerging technologies, such as artificial intelligence and laser communication. The deployment of practical employment around the Earth will ensure a response to the growing anti-satellite threats (Krelina, 2023). Quantum sensors play a crucial role in transforming critical sectors by leveraging the unique principles of quantum mechanics, thereby enabling unprecedented precision, security, and efficiency. Real-world uses of quantum sensors in Quantum Key Distribution (QKD) for accurate navigation and spotting hidden threats, along with combining them with current systems and Artificial Intelligence (AI) for quick decision-making, are still being developed (Abraheem et al., 2025). The elements of quantum sensors, which have found applications in navigation systems, mainly consist of atomic clocks and gyroscopes. Atomic clocks based on quantum principles provide precise timekeeping, which is essential for global positioning systems (GPS) and satellite communications. Quantum gyroscopes offer highly accurate rotational measurements, crucial for navigation in autonomous vehicles, drones, and aerospace applications (Khang & Rath, 2025).

5. Conclusion

The increasing prevalence of GNSS (Global Navigation Satellite System) jamming and spoofing poses a significant threat to modern aviation, particularly in regions affected by geopolitical conflict or military activity. These disruptions compromise the integrity of satellite-based navigation systems, which are critical for aircraft

positioning, route tracking, and approach procedures. Operational Impacts of GNSS Interference - jamming involves the deliberate transmission of radio frequency signals that overpower legitimate satellite signals, rendering navigation systems unreliable or unusable. Spoofing, on the other hand, deceives receivers by broadcasting false GNSS signals, potentially leading aircraft off course or misrepresenting their true location which is experienced aircraft Embraer-190 over Russian airspace. The consequences of such interference contributed to loss of positional awareness during critical flight phases such as approach and landing of the flight J2 8243. Due to increased workload for pilots even reverted to alternative navigation methods does not affect to avoid the fatal incident. The potential miscommunication with air traffic control especially when automated systems are compromised and ILS has been deactivated at airport destination, influenced reduced effectiveness of onboard safety systems. The crash of Azerbaijan Airlines flight J2 8243 in December 2024 near Grozny is a tragic example of how GNSS interference can exacerbate already dangerous conditions. Consequently, this incident underscores the vulnerability of civil aviation to GNSS disruptions, especially in conflict zones where such tactics are increasingly employed.

Although it remains clear that GNSS jamming is not directly caused the accident, its presence contributed to a degraded situational environment. Navigation signal blockage has hindered the crew's ability to accurately assess their position and trajectory. Stressful conditions were intensified by unreliable instrumentation, increasing the margin for error during emergency manoeuvres. Jamming and spoofing GNSS signals compromised and disrupted overall operations, mostly causing imprecise approaches and missed landings, leading to conducting twice go around procedure while avoiding collisions with mountain. However, the targeted aircraft used IRS data as well, for precise aircraft positioning while helping in navigation and flight management meanwhile providing terrain awareness. Radio altimeter provided real-time altitude readings above the ground, during two landing approach sensing terrain avoidance, having connection with GPWS which alerted to crew members to cancel the landing with both attempts. In turn, the direct GPWS interaction with LRRA is potential navigation tools to avoid terrain hazards. The finding reveals that reliable interaction between EGPWS and LRRA, while receiving a signal from IRS, has avoided terrain collision after two unsuccessful approaches, thus filling the gap of the lack of reliable terrain awareness during repeated approaches. This is a dedicated functionality which is secured by IRS operability in the cases of RF interference against civilian aircraft and if not receive GPS signal, to secure flight safety and passenger lives. As aviation continues to rely heavily on satellite-based navigation, the risks posed by jamming and spoofing must be addressed through robust detection and mitigation technologies including multi-sensor fusion and inertial backup systems. In this context pilot training and procedural updates to handle GNSS outages effectively can be reached by international collaboration and common regulations to monitor GNSS interference, especially in sensitive airspace. Numerous incidents serve as a sobering reminder that GNSS integrity is not just a technical issue-it is a matter of life and safety in the skies. Finally, GNSS jamming and spoofing are no longer hypothetical threats-they are real, present, and increasingly dangerous. The J2 8243 accident serves as a stark reminder that even indirect interference can have fatal consequences when combined with hostile environments. Aviation must evolve to meet this challenge, ensuring that the skies remain safe, even when signals go dark.

References

Abraheem, S. M., Ali, M. E., & Abuali, R. M. (2025). Emerging Trends in Quantum Sensors: Applications in Defense and Communication. *Middle East Journal of Pure and Applied Sciences* (MEJPAS), 1(1), 19-37.

Aftatah, M., & Zebbara, K. (2024). A Comprehensive Survey on Secure Navigation for Intelligent Systems: Artificial Intelligence Approaches to GPS Jamming and Spoofing Detection. In: Mejdoub, Y., Elamri, A. (Eds.), *Lecture Notes in Networks and Systems*: Vol.1123. Proceedings of the *International Conference on Connected Objects and Artificial Intelligence* (pp. 105-110). Springer. https://doi.org/10.1007/978-3-031-70411-6_17

Airbus. (2019). *In-service Information, GNSS loss and GNSS Interferences on Airbus A/C*. Ref: 34.36.00049.

Aissou, G., Slimane, H. O., Benouadah, S., & Kaabouch, N. (2021). Tree-based supervised machine learning models for detecting GPS spoofing attacks on UAS. In *2021 IEEE 12th Annual Ubiquitous Computing, Electronics & Mobile Communication Conference* (UEMCON) (pp. 0649-0653). IEEE. https://doi.org/10.1109/UEMCON53757.2021.9666744

Ali, B. S., Ochieng, W. Y., Schuster, W., Majumdar, A., & Chiew, T. K. (2015). A safety assessment framework for the Automatic Dependent Surveillance Broadcast (ADS-B) system. *Safety science*, 78, 91-100. https://doi.org/10.1016/j.ssci.2015.04.011

Altaweel, A., Mukkath, H., & Kamel, I. (2023). GPS Spoofing Attacks in FANETs: A Systematic Literature Review. *IEEE Access*, 11, 55233-55280. https://doi.org/10.1109/ACCESS.2023.3281731

Berglund, H.T., Blume, F., Estey, L., & White, S. (2011). GPS/GNSS Interference from Iridium Data Transmitters. In *Proceedings of the American Geophysical Union Fall Meeting* 2011, San Francisco, CA, https://www.researchgate.net/publication/259677698_GPSGNSS_Interference_from_Iridiu_Data_Transmitters

Blois, M., Studenny, J., O'Keefe, K., & Liu, B. (2023). Baseline spoofing detection for aircraft with standard navigation hardware. *Proceedings of the 36th International Technical Meeting of the Satellite Division of the Institute of Navigation* (pp. 824–835). https://doi.org/10.33012/2023.19413

Bong, J. H., Kim, D., & Jeong, S. (2023). AI-based Algorithm for GNSS Spoofing Detection. In 2023 *14th International Conference on Information and Communication Technology Convergence (ICTC)*, (pp. 1630-1632). IEEE. https://doi.org/10.1109/ICTC58733.2023.10392390

Bose, S. C. (2021). GPS spoofing detection by neural network machine learning. *IEEE Aerospace and Electronic Systems Magazine*, 37(6), 18-31. https://doi.org/10.1109/MAES.2021.3100844

Buesnel, G. (2020). *Thousands of GNSS jamming and spoofing incidents reported in* 2020. https://rntfnd.org/2020/12/24/thousands-of-gnss-jamming-and-spoofing-incidents-reported-in-2020-guy-buesnel/

Buesnel, G., & Holbrow, M. (2017). *GNSS Threats, Attacks and Simulations, PNT Advisory Board Baltimore*, 28-29. https://archive.gps.gov/governance/advisory/meetings/2017-06/buesnel.pdf

Chew, C., Roberts, T. M., & Lowe, S. (2023). RFI mapped by spaceborne GNSS-R data. NAVIGATION: *Journal of the Institute of Navigation*, 70(4), Article 618. https://doi.org/10.33012/navi.618

Darabseh, A., Bitsikas, E., & Tedongmo, B. (2019). Detecting GPS jamming incidents in OpenSky data. In *Proceedings of the 7th OpenSky Workshop*, 67, 97–108. https://doi.org/10.29007/1mmw

Domogala, P. (2025). *The dangers of GNSS interference*. https://ifatca.org/article/the-dangers-of-gnss-interference/

Dovis, F. (2015). *GNSS interference threats and countermeasures*. Artech House.

EASA. (2023). *EASA SIB No.: 2023-05-Europe, Subject: Safety Information Bulletin, Operations – ATM/ANS – Aerodromes Possible Risks Emerging During Summer* 2023. https://ad.easa.europa.eu

EASA. (2024). *EASA SIB No.: 2022-02R3 Global Navigation Satellite System Outage and Alterations Leading to Communication / Navigation / Surveillance Degradation*. https://www.easa.europa.eu/en/domains/air-operations/global-navigation-satellite-system-outages-and-alterations

Eurocontrol. (2021). *EUROCONTROL Think Paper #9 - Radio Frequency Interference to satellite navigation: An active threat for aviation?* https://www.eurocontrol.int/publication/eurocontrol-think-paper-9-radio-frequency-interference-satellite-navigation-active

Felux, M., Fol, P., Figuet, B., Waltert, M., & Olive, X. (2024). Impacts of global navigation satellite system jamming on aviation. NAVIGATION: *Journal of the Institute of Navigation*, 71(3), Article 657. https://doi.org/10.33012/navi.657

Fernández-Hernández, I., Walter, T., Alexander, K., Clark, B., Châtre, E., Hegarty, C., Appel, M., & Meurer, M. (2019). Increasing international civil aviation resilience: A proposal for nomenclature, categorization and treatment of new interference threats. In *Proceedings of the 2019 international technical meeting of the institute of navigation* (pp. 389-407). https://doi.org/10.33012/2019.16699

Figuet, B., Waltert, M., Monstein, R., & Felux, M. (2022). Impact of GNSS outage on mid-air collision risk. In *Proceedings of the 2022 International Workshop on ATM/CNS (IWAC)* (pp. 41–48). https://doi.org/10.57358/iwac.1.0_41

Flightvectors. (2025). *Cockpit B757/767*. https://www.flightvectors.com/Aircraft-Cockpit-Posters-Procedure-Trainers/Boeing-Cockpit-Posters-Procedure-Trainers/B757-B767/

Fol, P., & Felux, M. (2022). Identification and operational impact analysis of GNSS RFI based on flight crew reports and ADSB data. In *Proceedings of the 7th International Workshop on ATM/CNS (IWAC)* (pp. 33–40). https://doi.org/10.57358/iwac.1.0_33

Garcia, M., Dolan, J., & Sirigu, G. (2024). *GPS interference and spoofing in the Baltics*. Aireon. https://aireon.com/wp-content/uploads/2024/05/Aireon-White-Paper_GPS-Interference_May2024.pdf

Ghanbarzade, A., & Soleimani, H. (2025). *GNSS/GPS Spoofing and Jamming Identification Using Machine Learning and Deep Learning*. https://doi.org/10.48550/arXiv.2501.02352

Giovannetti, V., Lloyd, S., & Maccone, L. (2001). Quantum-enhanced positioning and clock synchronization. *Nature*, 412, 417-419. https://doi.org/10.1038/35086525

Götzelmann, M., Köller, E., Viciano-Semper, I., Oskam, D., Gkougkas, E., & Simon, J. (2023). Galileo open service navigation message authentication: Preparation phase and drivers for future service provision. NAVIGATION: *Journal of the Institute of Navigation*, 70(3), Article 572. https://doi.org/10.33012/navi.572

Gutierrez, P. (2024). *GMV-led Project Develops AI-based Jamming and Spoofing Mitigation*. https://insidegnss.com/gmv-led-project-develops-ai-based-jamming-and-spoofing-mitigation/

He, Y., Li, B., Chen, J., Wang, Z., Xiao, W., & Lu, Z. (2024). Overview of the development of satellite navigation blanket interference monitoring. *Frontiers in Physics*, 12, Article 1487384. https://doi.org/10.3389/fphy.2024.1487384

Hegarty, C., Odeh, A., Shallberg, K., Wesson, K., Walter, T., & Alexander, K. (2018). Spoofing detection for airborne GNSS equipment. In *Proceedings of the 31st International Technical Meeting of the Satellite Division of The Institute of Navigation* (pp. 1350-1368). https://doi.org/10.33012/2018.16008

Hexagon. (2025). *What Are Global Navigation Satellite Systems?* https://novatel.com/tech-talk/an-introduction-to-gnss/what-are-global-navigation-satellite-systems-gnss

Humphreys, T. E. (2013). Detection Strategy for Cryptographic GNSS Anti-Spoofing. *IEEE Transactions on Aerospace and Electronic Systems*, 49(2), 1073–1090. https://doi.org/10.1109/TAES.2013.6494400

Humphreys, T.E., Ledvina, B.M., Psiaki, M.L., O'Hanlon, B.W., & Kintner, P.M. (2008). Assessing the Spoofing Threat: Development of a Portable GPS Civilian Spoofer. *Proceedings of the 21st International Technical Meeting of the Satellite Division of the Institute of Navigation* (ION GNSS Conference) (pp. 2314-2325).

IATA. (2024). *Global Navigation Satellite System GNSS Radio Frequency Interference, Safety Risk Assessment*. https://ic.iata.org/sites/default/files/iata_sih_document_attachment/IATA_Safety_Risk_Assessment_GNSS_Interference.pdf

ICAO. (2003). *Operational use of ADS-B in Non-Radar Airspace Generic Design Safety Case*. ICAO Separation and Airspace Safety Panel (SASP).

ICAO. (2018). *Manual on Testing of Radio Navigation Aids*. Volume I - Testing of Ground-based Radio Navigation Systems, DOC 8071, Fifth Edition.

ICAO. (2022). *Assembly-41st Session Technical Commission Aviation Safety and Air Navigation Standardization*. GNSS Interference, Working Paper A41-WP/196

Issam, S. M., Adnane, A., & Madiabdessalam, A. I. T. (2020). Anti-Jamming techniques for aviation GNSS-based navigation systems: Survey. In *Proceedings of the 2020 IEEE 2nd international conference on electronics, control, optimization and computer science* (ICECOCS) (pp. 1-4). IEEE, https://doi.org/10.1109/ICECOCS50124.2020.9314449

Jonáš, P., & Vitan, V. (2019). Detection and localization of GNSS radio interference using ADS-B data. In *Proceedings of the 2019 International Conference on Military Technologies (ICMT)* (pp. 1–5). IEEE. https://doi.org/10.1109/MILTECHS.2019.8870034

Joseph, A., Bartolone, P., Griggs, J., Schnaufer, B., Phan, H., & Malhotra, V. (2023). GNSS radio frequency interference mitigation in Collins commercial airborne receivers. *Engineering Proceedings*, 54(1), Article 18. https://doi.org/10.3390/ENC2023-15420

Jozsa, R., Abrams, D. S., Dowling, J. P., & Williams, C. P. (2000). Quantum clock synchronization based on shared prior entanglement. *Physical Review Letters*, 85(9). https://doi.org/10.1103/physrevlett.85.2010

Jullian, O., Otero, B., Stojilović, M., Costa, J. J., Verdú, J., & Pajuelo, M. A. (2022). Deep learning detection of GPS spoofing. In *International Conference on Machine Learning, Optimization, and Data Science* (pp. 527-540). Springer. https://doi.org/10.1007/978-3-030-95467-3_38

Khang, A., & Rath, K. C. (2025). *The quantum evolution: Application of AI and robotics in the future of quantum technology* (1st ed.). CRC Press.

Krelina, M. (2021). Quantum technology for military applications. *EPJ Quantum Technology*, 8(1), Article 24. https://doi.org/10.1140/epjqt/s40507-021-00113-y

Krelina, M. (2023). The prospect of quantum technologies in space for defence and security. *Space Policy*, 65, Article 101563. https://doi.org/10.1016/j.spacepol.2023.101563

Liu, Z., Lo, S., & Walter, T. (2020). GNSS interference characterization and localization using OpenSky ADS-B data. *Proceedings of the 8th OpenSky Symposium*, 59(1), Article 10. https://doi.org/10.3390/proceedings2020059010

Liu, Z., Lo, S., & Walter, T. (2021). GNSS interference detection using machine learning algorithms on ADS-B data. *Proceedings of the 34th International Technical Meeting of the Satellite Division of the Institute of Navigation* (pp. 4305–4315). https://doi.org/10.33012/2021.18111

Liu, Z., Lo, S., & Walter, T. (2022). GNSS interference source localization using ADS-B data. *Proceedings of the 2022 International Technical Meeting of the Institute of Navigation* (pp. 158–167). https://doi.org/10.33012/2022.18241

Lomas, C. (2025). *GPS jamming: the benign, the bad, and the scary*. https://www.flightradar24.com/blog/inside-flightradar24/types-of-gps-jamming/

Ludlow, A. D., Boyd, M. M., Ye, J., Peik, E., & Schmidt, P. O. (2015). Optical atomic clocks. *Reviews of Modern Physics*, 87(2), 637-701. https://doi.org/10.1103/RevModPhys.87.637

Lukeš, P., Topková, T., Vlček, T., & Pleninger, S. (2020). Recognition of GNSS jamming patterns in ADS-B data. In *Proceedings of the 22th International Conference on New Trends in Civil Aviation (NTCA 2020)* (pp. 9–15). https://doi.org/10.23919/NTCA50409.2020.9291039

Macey, J. (2024). *AI & Quantum Powered Navigation System to Counter GPS Jamming Threats*. https://www.defenseadvancement.com/news/ai-quantum-powered-navigation-system-to-counter-gps-jamming-threats/

Meng, L., Yang, L., Yang, W., & Zhang, L. A. (2022). A Survey of GNSS Spoofing and Anti-Spoofing Technology. *Remote Sensing*, 14(19), Article 4826. https://doi.org/10.3390/rs14194826

Murrian, M. J., Narula, L., Iannucci, P. A., Budzien, S., O'Hanlon, B. W., Psiaki, M. L., & Humphreys, T. E. (2021). First results from three years of GNSS interference monitoring from low Earth orbit. NAVIGATION: *Journal of the Institute of Navigation*, 68(4), 673–685. https://doi.org/10.1002/navi.449

National Academies of Sciences, Engineering, and Medicine. (2023). *Analysis of Potential Interference Issues Related to FCC Order 20-48*. National Academies Press. https://doi.org/10.17226/26611

Nayfeh, M., Li, Y., Al Shamaileh, K., Devabhaktuni, V., & Kaabouch, N. (2023). Machine learning modeling of GPS features with applications to UAV location spoofing detection and classification. *Computers & Security*, 126, Article 103085. https://doi.org/10.1016/j.cose.2022.103085

NordSky. (2024). *Understanding GNSS Jamming and Spoofing: Challenges and Solutions*. https://www.nordsky.com/understanding-gnss-jamming-and-spoofing/

OPSGroup. (2024). *GPS Spoofing: Final Report published by Work Group*. https://ops.group/blog/gps-spoofing-final-report/

Osechas, O., Felux, M., Fohlmeister, F., & Dautermann, T. (2021). Impact of RFI on GNSS and avionics–A view from the cockpit. *Proceedings of the 34th International Technical Meeting of the Satellite Division of the Institute of Navigation* (pp. 1142–1159). https://doi.org/10.33012/2021.18055

Osechas, O., Fohlmeister, F., Dautermann, T., & Felux, M. (2022). Impact of GNSS-Band Radio Interference on Operational Avionics. NAVIGATION: *Journal of the Institute of Navigation*, 69(2), Article 516. https://doi.org/10.33012/navi.516

Petchenik, I. (2025). *How We Track Flights with MLAT*. https://www.flightradar24.com/blog/inside-flightradar24/how-we-track-flights-with-mlat/

Pirandola, S., Andersen, U.L., Banchi, L., Berta, M., Bunandar, D., Colbeck, R., Englund, D., Gehring, T., Lupo, C., Ottaviani, C., Pereira, J. L., Razavi, M., Shamsul Shaari, J., Tomamichel, M., Usenko, V. C., Vallone, G., Villoresi, P., & Wallden, P. (2020). Advances in quantum cryptography. *Advances in Optics and Photonics*, 12(4), 1012-1236. https://doi.org/10.1364/AOP.361502

Psiaki, M. L., Humphreys, T. E., & Stauffer, B. (2016). Attackers can spoof navigation signals without our knowledge. Here is how to fight back GPS lies. *IEEE Spectrum*, 53(8), 26–53. https://doi.org/10.1109/MSPEC.2016.7524168

Pultarova, T. (2025). *How Ukraine's Drones are Beating Russian Jamming*. https://spectrum.ieee.org/killer-drones

Qiao, J., Lu, Z., Lin, B., Song, J., Xiao, Z., Wang, Z., & Li, B. (2023). A survey of GNSS interference monitoring technologies. *Frontiers in Physics*, 11, Article 1133316. https://doi.org/10.3389/fphy.2023.1133316

Radoš, K., Brkić, M., & Begušić, D. (2024). Recent advances on jamming and spoofing detection in GNSS. *Sensors*, 24(13), Article 4210. https://doi.org/10.3390/s24134210

Rothmaier, F., Chen, Y. H., Lo, S., & David Powell, J. (2019a). Single GNSS antenna heading estimation. *Proceedings of the 32nd International Technical Meeting of the Satellite Division of the Institute of Navigation* (pp. 2159–2171). https://doi.org/10.33012/2019.16915

Rothmaier, F., Chen, Y. H., Lo, S., & Walter, T. (2021). GNSS spoofing detection through spatial processing. NAVIGATION: *Journal of the Institute of Navigation*, 68(2), 243-258. https://doi.org/10.1002/navi.420

Rothmaier, F., Chen, Y., & Lo, S. (2019b). Improvements to steady state spoof detection with experimental validation using a dual polarization antenna. *Proceedings of the 32nd International Technical Meeting of the Satellite Division of the Institute of Navigation* (pp. 967–983). https://doi.org/10.33012/2019.16989

Safrangroup. (2025). *Meeting the challenges of "jamming" and "spoofing" in civil aviation*. https://www.safran-group.com/news/meeting-challenges-jamming-and-spoofing-civil-aviation-2025-01-15

Scaramuzza, M., Wipf, H., Troller, M., Leibundgut, H., Rämi, S., & Wittwer, R. (2015). GNSS RFI detection: Finding the needle in the haystack. *Proceedings of the 28th International Technical Meeting of the Satellite Division of the Institute of Navigation* (pp. 1617–1624). https://www.ion.org/publications/abstract.cfm?articleID=13064

Slingshot Aerospace. (2025). *Slingshot to Develop Geolocation and AI-based GPS Jamming and Spoofing Detection Technology for US Space Force*. https://www.everythingrf.com/news/Details/19542-slingshot-to-develop-geolocation-and-ai-based-gps-jamming-and-spoofing-detection-technology-for-us-space-force

Stanisak, M., Wilkens, C., & Musmann, F. (2024). *High-precision Reference Positioning in Case of GNSS Jamming*. https://icasc.co/wp-content/uploads/2024/08/High_Precision-Reference-Positioning-in-Case-of-GNSS-Jamming.pdf

Summers. C. (2025). *GPS Spoofing, Jamming Attacks in the Air Are Increasing, Experts Say*. https://www.theepochtimes.com/us/gps-spoofing-jamming-attacks-in-the-air-are-increasing-say-experts-5925866

System Schematic Manual. (2025). *System Schematic Manual* (SSM), Chapter 34: Embraer E190, Available at: Author Library.

Van Trees, H. L. (2001). *Detection, Estimation, and Modulation Theory* (Part I). John Wiley & Sons. https://doi.org/10.1002/0471221082

Villamizar, H. (2025). *Impacts of GPS Spoofing on Commercial Aviation*. https://www.airwaysmag.com/new-post/gps-spoofing-commercial-aviation

Wineland, D. J., & Dehmelt, H. G. (2021). Precision quantum clocks: From superposition to hyperfine interactions. *Reviews of Modern Physics*, 90(4), 173-199.

Wu, Z., Zhang, Y., Yang, Y., Liang, C., & Liu, R. (2020). Spoofing and Anti-Spoofing Technologies of Global Navigation Satellite System: A Survey. *IEEE Access*, 8, 165444–165496. https://doi.org/10.1109/ACCESS.2020.3022294

Xiao, J., Li, Y., Zhang, C., & Zhang, Z. (2022). INS/GPS Integrated Navigation for Unmanned Ships Based on EEMD Noise Reduction and SSA-ELM. *Journal of Marine Science and Engineering*, 10(11), Article 1733. https://doi.org/10.3390/jmse10111733

Zarrinnegar, K., Tohidi, S., Mosavi, M. R., Sadr, A., & de Andrés, D. M. (2023). Improving Cross Ambiguity Function Using Image Processing Approach to Detect GPS Spoofing Attacks. *Iranian journal of electrical & electronic engineering*, 19(1), Article 2584. http://ijeee.iust.ac.ir/article-1-2584-en.html

Zidan, J., Adegoke, E. I., Kampert, E., Birrell, S. A., Ford, C. R., & Higgins, M. D. (2020). GNSS vulnerabilities and existing solutions: A review of the literature. *IEEE Access*, 9, 153960-153976. https://doi.org/10.1109/ACCESS.2020.2973759

National Aviation Academy

International Journal of Transportation Research and Technology

e-ISSN: 3079-6075

DOI: 10.71108/transporttech.vm03is01.04

Research Article

Enhancing Object Detection in UAV Videos under Complex Environments

Dmytro Krytskyi, Alina Artomova, Elvira Kaidan*

National Aerospace University "Kharkiv Aviation Institute", Kharkiv, Ukraine

Timescale of article

Received: 09 April 2026
Accepted: 19 May 2026
Published: 25 June 2026

Corresponding author

Elvira Kaidan
e.s.kaidan@student.khai.edu

Keywords:

Unmanned Aerial Vehicle, RGB sensor, Self-calibration, Color correction, YOLO11s, Precision–Recall, F1-score, mAP

Cite this article as:

Krytskyi, D., Artomova, A., & Kaidan, E. (2026). Enhancing Object Detection in UAV Videos under Complex Environments. *International Journal of Transportation Research and Technology*, 3(1), 45-57.
DOI: 10.71108/transporttech.vm03is01.04

Abstract

The paper presents an improved computer vision system for unmanned aerial vehicles (UAVs) that combines RGB sensor lighting compensation with an optimized YOLO11s detection model. Unlike traditional digital correction methods (AWB, CLAHE, Histogram Equalization), the proposed approach is based on physical measurements of illumination and provides dynamic stabilization of detection confidence in real time. The use of white stripe padding during preprocessing eliminated geometric distortions and increased the stability of bounding box formation. Reducing the number of classes to four (armored_vehicle, support_vehicle, tank, vehicle) reduced the number of misclassifications and accelerated inference.

The YOLO11s model demonstrated high efficiency: the total mAP@0.5 is 0.939, and for the classes support_vehicle, vehicle, and tank, values of 0.983, 0.968, and 0.956 were achieved, respectively. Analysis of the Precision–Confidence, Recall–Confidence, and F1–Confidence curves confirmed the stable operation of the system over a wide range of thresholds, with a maximum F1 ≈ 0.89 at a threshold of about 0.4. The normalized confusion matrix shows a 20–35% reduction in false negatives. The model training time was reduced to 27 minutes, and the processing speed is 22–25 FPS with an additional power consumption of 0.18 W compared to the baseline UAV vision system without RGB sensor compensation.

Field experiments in conditions of grass cover, dry vegetation, smoke, and fog confirmed the effectiveness of sensory feedback and the stability of detection in complex visibility conditions.

1. Introduction

Computer vision systems for unmanned aerial vehicles (UAVs) are widely used for monitoring, reconnaissance, search, and analysis of ground objects. The effectiveness of such systems largely depends on the stability of detection algorithms under conditions of variable natural lighting. Fluctuations in light intensity, the presence of smoke, fog, shadows, and various spectral characteristics of the surface lead to a decrease in recognition accuracy and instability of the confidence thresholds of deep learning models. Single-frame detectors such as YOLO are particularly sensitive to these factors, with their accuracy deteriorating in conditions of strong glare, low contrast, or image distortion during preprocessing.

Traditional lighting compensation methods, such as automatic white balance (AWB), CLAHE, and histogram equalization, operate after the image is formed and do not take into account the physical parameters of the scene, which often leads to color distortion or noise amplification. This necessitates combining sensor measurements with algorithmic compensation to create stable operating conditions for the detectors.

The image preprocessing strategy also plays an important role. Scaling with frame stretching distorts the proportions of objects and reduces detection quality, while letterboxing preserves the geometric structure of the scene and improves the accuracy of object boundary detection.

Modern deep learning architectures, such as the YOLO11s model, provide high performance, reduced inference latency, and increased accuracy with low power consumption. This makes them suitable for UAV onboard systems that must operate reliably in dynamic and challenging outdoor environments.

This combination not only improves detection accuracy, but also significantly reduces the number of false positives, stabilizes the model's confidence mechanism, and ensures rapid adaptation to difficult observation conditions—smoke, fog, uneven lighting, and natural obstacles.

The goal of this work is to create and experimentally test an updated UAV computer vision sensor system that provides increased accuracy and stability in detecting objects in various natural conditions, using a hardware-algorithmic approach to lighting compensation and an optimized YOLO11s architecture.

Computer vision systems for UAVs have been actively developing in recent years due to the introduction of deep learning methods. Reviews indicate that modern neural network detectors provide high accuracy in controlled conditions, but their effectiveness is significantly reduced in real field scenarios where there are sharp changes in lighting, shadows, atmospheric interference, and complex backgrounds (Wu et al., 2021).

In a comprehensive review, Wu et al. emphasize that the key problem of UAV detection is the instability of input images, rather than the limitations of neural network architecture (Wu et al., 2021). The authors note that even modern models show a significant drop in Precision and Recall values when lighting conditions change, particularly in shadows or in the presence of haze.

Similar conclusions are presented in the work of Tang et al., which analyzes modern approaches to object detection with UAVs based on deep learning (Tang et al., 2024). The authors note that most studies focus on architectural improvements to models, while the issue of physical stabilization of the input signal is often overlooked.

A separate area of research is devoted to compensating for shadows and changes in lighting in aerial photographs. In their work, Liu et al. propose a method of local color correction that takes into account the textural features of the scene, which allows preserving the geometry of objects and improving the quality of subsequent detection (Liu et al., 2022). The authors demonstrate that stabilizing the color balance before the neural network analysis stage reduces the number of false positives.

Further development of shadow compensation methods is presented in the work of Shen et al., which uses an automatically generated synthetic dataset to train lighting correction algorithms (Shen et al., 2025). The study confirms that preliminary lighting normalization significantly improves the stability of computer vision algorithms in complex optical conditions.

For scenes with fog, smoke, and reduced contrast, dehazing methods are widely studied. A comprehensive review by Gui et al. shows that most modern deep learning approaches are focused on digital contrast restoration, but have high computational complexity and limited suitability for real-time use on embedded platforms (Gui et al.,

2021). Similar conclusions are presented in the work of Cheng et al., which emphasizes the trade-off between restoration quality and algorithm performance (Cheng et al., 2022).

At the same time, the YOLO family of neural network detectors, which have become the standard for real-time tasks, is actively developing. Ultralytics documentation confirms that modern versions of YOLO, in particular YOLO11, are focused on optimizing inference and reducing latency while maintaining high accuracy (Ultralytics, 2024; Ultralytics, 2024–2025). Further reviews of YOLO's evolution show that new architectures provide better bounding box consistency and more stable F1-score values in complex scenes (Sapkota & Karkee, 2025).

An important aspect is the image preprocessing strategy. Ultralytics' technical documentation states that the use of letterboxing (proportional padding) avoids geometric distortions and improves detection stability for objects of different scales (Ultralytics, 2023-2024). Practical recommendations from the Ultralytics community confirm the effectiveness of this approach during real-time inference (Murat & Kiran, 2025).

Correct assessment of color differences plays a special role in stabilizing visual systems. The works of Zhao et al. show that the use of color difference metrics, in particular ΔE according to the CIE standard, allows quantitative assessment of color reproduction quality in conditions of a wide dynamic range (Zhao et al., 2020). Similar results are presented in the study by Basova et al., which emphasizes the relevance of such metrics for systems with high lighting variability (Basova et al., 2024).

Thus, analysis of current research shows that the most promising direction is the combination of physically based lighting compensation methods, optimized image preprocessing, and the use of modern neural network detectors. It is this comprehensive approach that allows increasing the stability of UAV computer vision systems in real field conditions and ensuring stable Precision, Recall, F1-score, and mAP values without the need to retrain the model.

2. Method

The proposed system is based on the principle of combining sensor-based illumination compensation and optimized neural network detection. The main idea is that the RGB sensor continuously measures the spectral components of the ambient light, and the compensation coefficient calculated based on this data is used to stabilize the brightness and contrast of the video stream before the image is fed into the YOLO11s model. This approach reduces input variability, improves color balance consistency, and prevents detection quality degradation in conditions of shadow, smoke, or fog.

During preprocessing, white padding is applied to a square format instead of scaling, which eliminates geometric distortions and preserves the proportions of objects. This significantly improves the stability of detection frame formation, as the model receives uncorrupted target geometry even with different frame aspect ratios.

Optimizing the set of classes to four has reduced the number of misclassifications, accelerated inference, and increased model confidence on complex backgrounds. Combined with the new YOLO11s model, which has lower latency and higher accuracy compared to the previous YOLO8n, this provides a significant increase in system quality without increasing computational costs. YOLO8n was used only as a baseline model for comparison, whereas the proposed system is based on the optimized YOLO11s architecture.

Thus, the general principle of the system is to stabilize the input signal in stages (sensor correction → padding → normalization → detection), which allows for high accuracy in real time and ensures the algorithm's stability to dynamic lighting changes during UAV flight.

2.1. System hardware architecture

The hardware part of the system includes a TCS34725 RGB sensor, an ESP32-S3 microcontroller, an HQ camera, and a Jetson Nano computing module. The TCS34725 sensor is equipped with photodiodes for the R, G, B, and Clear channels and a 16-bit ADC, which provides stable light measurements in the range of 0.1–65,000 Lux. The built-in IR filter minimizes distortions caused by direct sunlight. The sensor is mounted next to the camera on a rigid platform to eliminate the parallax effect and ensure that the same lighting environment is recorded (AMSCO / AMS-OSRAM, n.d.).

The ESP32-S3 microcontroller receives data via I²C (400 kHz), averages 10 measurements to reduce noise, and calculates the illumination compensation factor. Data is transmitted to the computing module via an MQTT channel with a typical delay of up to 80 ms (Espressif Systems, 2023). The HQ camera with an 8 mm lens and a

1/2.3" CMOS sensor operates in the exposure range of 1/50–1/10,000 s, which allows for stable frame formation in conditions of contrasting or diffused lighting (Raspberry Pi Foundation, 2023).

The main processing is performed by Jetson Nano 2GB with TensorRT optimization support. The module performs YOLO11s model inference at a rate of 22–25 frames/s with an input image size of 640×640 (NVIDIA, 2022). Power is supplied by a 3S LiPo battery (11.1 V, 5200 mAh), and the total power consumption of the hardware complex does not exceed 7.2 W (AYAATech, n.d.). This configuration ensures real-time operation of the system without overloading the UAV's computing resources.

The generalized structure of the hardware-software interaction of the system components is shown in Fig. 1.

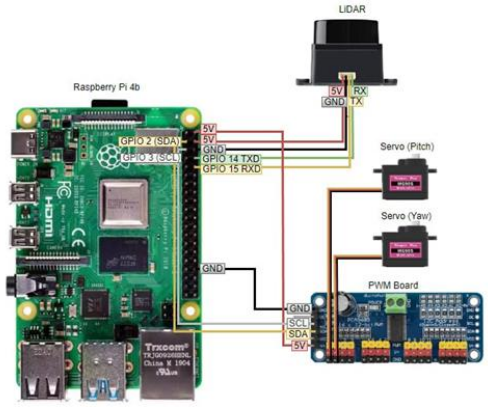

Fig. 1. Schematic representation of the hardware and software architecture of the sensor-based illumination compensation and neural network detection system (Source: Authors' own work)

The presented scheme illustrates the logic of data exchange between the RGB sensor, camera, and computing module. The light sensor generates a correction coefficient that is applied to the video stream before it is fed into the neural network, which allows stabilizing the input data regardless of lighting conditions.

The algorithmic part relies on the formation of a lighting compensation coefficient derived from the current measurements of the RGB sensor. The coefficient is calculated according to Equation (1), which defines the ratio between the reference RGB components obtained during calibration and the current measured values:

$$K_C = \frac{R_0 + G_0 + B_0}{R + G + B} \tag{1}$$

R_0, G_0, B_0 — reference values determined during sensor calibration under normal lighting conditions

R, G, B — current measured components

To avoid brightness jumps and ensure smooth response during rapid environmental changes, such as entering shade, smoke, or fog, recursive smoothing is applied using Equation (2):

$$K_C^*(t) = \alpha K_C(t) + (1 - \alpha) K_C(t - \Delta t) \tag{2}$$

α = 0.92

Δt = 0.2 c

This provides a correct response to changes in lighting during UAV flight, for example when entering an area of shadow, smoke, or fog.

In practice, the compensation coefficient fluctuations remained within 10–15%, which is consistent with the stable operation of the detector under various natural conditions and confirms the sufficient inertia of the filter for real flight.

Pre-processing of video frames has been optimized separately. Instead of scaling to a fixed size, which can distort objects and impair localization, letterboxing with white bars is used to a square format of 640×640 pixels. This allows you to maintain the proportions of the scene, stabilize the geometry of targets, and increase the reliability of bounding box formation, which is especially important for objects with a pronounced structure (for example, tracked vehicles). As a result, classification confidence is increased and the model's sensitivity to scale changes, perspective distortions, and uneven lighting is reduced.

The key difference in the updated implementation is the use of the YOLO11s model instead of YOLOv8n. The transition to YOLO11s has increased accuracy and reduced inference latency in real-time operation, as well as significantly reduced training time (to ~27 minutes instead of >2 hours) thanks to a more efficient architecture (Hidayatullah et al., 2025). To reduce interclass confusion and improve prediction consistency, the set of classes was optimized to four categories: armored_vehicle, support_vehicle, tank, vehicle. Fewer classes reduce errors at the boundaries of similar categories and simultaneously reduce the computational cost of the classification part of the detector.

YOLO11s was trained on a set of images of military equipment in various landscape and climatic conditions. The distribution of examples by class is shown in Fig. 2 (armored_vehicle — 398, support_vehicle — 216, tank — 137, vehicle — 35).

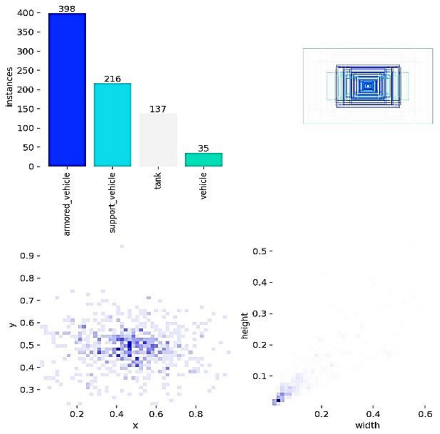

Fig. 2. Class distribution chart (Source: Authors' own work)

The imbalance reflects the actual frequency of objects in field scenarios, and the wide range of bounding box sizes and positions contributes to the formation of a generalizable model capable of working with targets of different scales. Subsequently, the quality of the model was evaluated using Precision, Recall, F1-score, andmAP@0.5 metrics, as well as the behavior of PR curves and confusion matrices, which allows for a comprehensive characterization of the detector in complex optical environments to mitigate the effect of class imbalance, data augmentation techniques were applied, including scaling, rotation, and brightness variation. In addition, samples were collected across different environmental scenarios to improve generalization. Model performance was evaluated using class-wise metrics and confusion matrices, which confirmed stable detection quality even for minority classes.

3. Experimental Part

Field tests of the system were conducted in open conditions with natural lighting, which varied in both intensity and spectral composition. To evaluate the algorithm's performance, four typical scenarios were created that correspond to the real conditions of UAV use: a grassy surface with sharp transitions between light and shadow; a local smoke screen with reduced contrast; dry vegetation with a changed spectral background; a foggy environment with scattered light and muted RGB components.

To improve reproducibility, the environmental conditions were additionally quantified. The illumination level measured by the TCS34725 sensor varied in the range of 500–65,000 Lux. Smoke and fog conditions were characterized by a decrease in RGB intensity and contrast, reflected in histogram compression and signal attenuation. Dynamic lighting variations were evaluated using the compensation coefficient, whose fluctuations

remained within 10–15%. These parameters provide a quantitative description of complex environments and allow reproducibility of the experimental setup.

Each scenario used camouflaged Pixel, Multicam, and Olive mock-ups, as well as camouflage nets. The drone flew at altitudes of 10, 20, and 30 m at speeds of up to 2 m/s. Each flight lasted 120 seconds, which provided sufficient data for further statistical analysis.

An experimental hardware setup was used to conduct the experiments, which reproduced the configuration of the UAV's onboard computer vision system in laboratory and field conditions (Fig. 3). Rigid fixation of the camera, RGB sensor, and computing module ensured stable geometric conditions and eliminated the influence of mechanical disturbances on the measurement results.

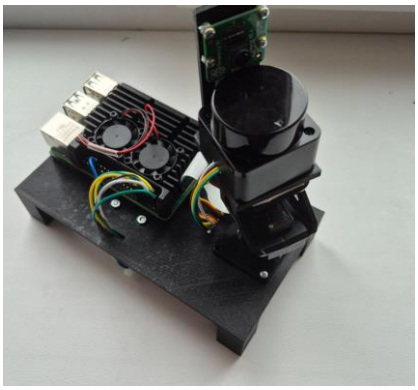

Fig. 3. Experimental model of a computer vision system with RGB sensor lighting compensation (Source: Authors' own work)

All images (Fig. 4) for further analysis were obtained in real conditions, including various levels of smoke, shadows, contrasting areas, and low atmospheric transparency.

Fig. 4. Samples of experimental footage during UAV flights (Source: Authors' own work)

The examples provided illustrate real-life situations in which the system must ensure stable detector operation: scenes with varying contrast, uneven surface structure, local explosions and smoke clouds, as well as a large number of small objects in the field of view. Such conditions create significant obstacles for computer vision algorithms - from sharp brightness changes and exceeding the camera's dynamic range to partial object overlap and the appearance of noise artifacts. That is why they were included in the experimental set to evaluate the system's performance in scenarios as close to real-world field conditions as possible.

As can be seen from the samples, the objects are located at different scales and at different viewing angles, which made it possible to test the performance of the YOLO11s model when changing the flight altitude, perspective distortions, and the level of detail of the target. Some frames contain intense smoke flows or areas of low transparency, which made it possible to investigate the effect of sensor compensation of lighting on the quality of detection in conditions of video signal degradation.

3.1. Data processing and system stability analysis

Experimental data was collected by simultaneously recording video from the camera and measuring illumination using an RGB sensor. The camera recorded video in 1080p format at 30 frames per second, while the sensor transmitted data at 200 ms intervals. Synchronization between video frames and sensor measurements was ensured using UNIX time stamps. For additional verification of time consistency, a control LED was used, which was activated simultaneously with the sensor polling. The total amount of experimental data was over 60,000 video frames and over 12,000 light measurements, which were stored in CSV format (R, G, B, Lux, timestamp) and subsequently synchronized by timestamps (Fig. 5).

Fig. 5. Example of video frames obtained during an experiment with touch control of lighting (Source: Authors' own work)

The dataset used in this study consists of UAV video frames collected during field experiments under various environmental conditions. The dataset was divided into training, validation, and test subsets in a ratio of approximately 70/15/15. Annotation was performed manually using bounding boxes for four classes (armored_vehicle, support_vehicle, tank, vehicle). To ensure label quality, a subset of annotations was additionally verified manually.

During the preprocessing stage, the strategy for preparing images for inference was changed. Instead of scaling frames, white padding was applied to a square format of 640×640 pixels, which made it possible to avoid geometric distortions, preserve the proportions of objects, and stabilize their shape regardless of the aspect ratio of the original image. This approach had a positive effect on classification confidence, especially in conditions of uneven lighting and complex backgrounds. Additionally, the number of classes was optimized to four (armored_vehicle, support_vehicle, tank, vehicle), which reduced interclass overlap and shortened inference time without losing information. To validate the effectiveness of the proposed approach, a comparative evaluation with standard image enhancement methods (AWB, CLAHE, and Histogram Equalization) was performed under identical experimental conditions, as summarized in Table 1.

Table 1. Comparison of image preprocessing methods under identical conditions

Method	Precision	Recall	F1-score	mAP@0.5
AWB	0.71	0.68	0.69	0.74
CLAHE	0.74	0.71	0.72	0.78
Histogram Equalization	0.72	0.69	0.70	0.76
Proposed method	0.83	0.81	0.84	0.939

Object detection was performed using the YOLO11s model in 640×640 pixel format with an average speed of 22–25 frames per second. Performance was evaluated using Precision, Recall, F1-score, and mAP@0.5 metrics. To verify the correctness of the automatic calculations, 15% of the frames were randomly selected and analyzed manually. Based on the results, Precision–Confidence, Recall–Confidence, F1–Confidence, and Precision–Recall graphs were constructed (Fig. 6), which reflect the behavior of the model when the confidence threshold changes.

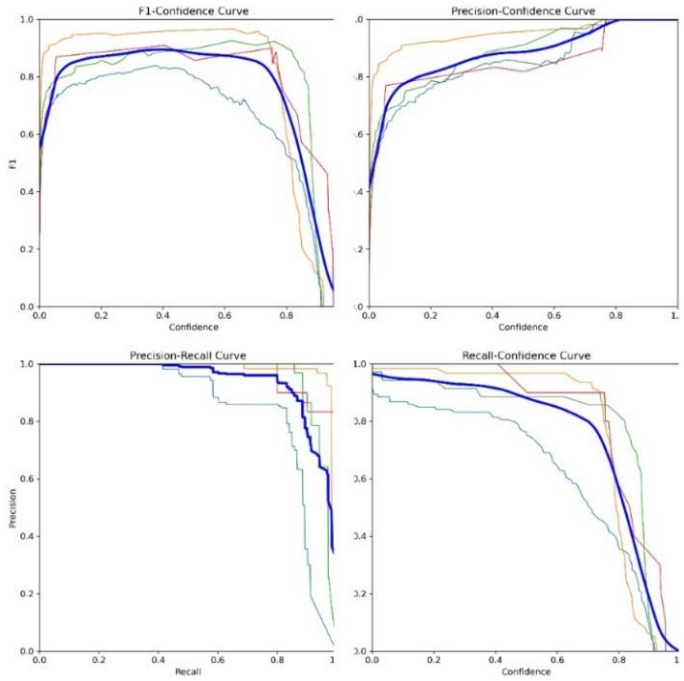

Fig. 6. BoxP, BoxR, F1, PR-curve graphs (Source: Authors' own work)

The graphs show that the blue curve reflects the average values of metrics for all classes and provides an integral assessment of the model's performance regardless of the frequency of occurrence of individual objects. It is smoothed and shows a general upward trend in Precision, Recall, and F1-score with a change in the confidence threshold. The thin colored lines characterize the class-specific behavior of the model and allow us to assess the complexity of detecting individual categories. In particular, classes with more examples in the training sample (armored_vehicle, support_vehicle) have smoother curves, while the rare vehicle class shows increased variability.

The averaged curve runs above most class dependencies in the range of average confidence thresholds, indicating the stable performance of YOLO11s and its ability to maintain high Precision, Recall, and F1-score values even with heterogeneous data structures. The Precision–Recall curve reached a value of mAP@0.5 = 0.939, indicating a high degree of consistency between the predicted and reference object boundaries.

The obtained dependencies confirm the increase in Precision and Recall indicators after applying sensor light compensation and optimized image preprocessing. The model demonstrates increased sensitivity to objects in fog, smoke, and on heterogeneous surfaces, which indicates the effectiveness of integrating physical light measurements into the input data formation process.

Energy consumption monitoring using an INA219 sensor with a sampling frequency of 1 Hz showed that the additional load from the RGB sensor and the calculation of the compensation coefficient is insignificant. The average consumption of the sensor module was about 0.18 W (≈1–1.2% of the total power of the platform), which does not affect the flight duration of a light reconnaissance UAV.

The stability of the algorithm was evaluated by analyzing the dynamics of the compensation coefficient K_c^* in real conditions. During sharp changes in illumination (Fig. 5) — for example, when entering a shadow, the appearance of a smoke screen, or a change in the direction of the sun's rays — the system demonstrated smooth correction without brightness jumps.

Fig. 7. Examples of stable object detection in conditions of sudden changes (Source: Authors' own work)

The maximum deviation of the coefficient did not exceed 12–15%, and the response delay was 0.35–0.40 s. Under these conditions, the video stream remained stable, without overexposure or underexposure, and the neural network received uniformly normalized frames with constant contrast.

Thus, the results of the experiments confirm that the proposed system provides stable detection performance in dynamic lighting conditions, has a minimal impact on the energy balance of the UAV, and effectively maintains the quality of object detection in real time.

It should be noted that the experiments were conducted at UAV speeds of up to 2 m/s, which corresponds to low-speed platforms. At higher speeds, system latency may cause bounding box displacement and reduce tracking stability. Therefore, the current approach is primarily suitable for low-speed UAV applications, while further work should focus on improving performance for faster platforms.

In addition, the system demonstrates low energy consumption (~0.18 W) and acceptable end-to-end latency, confirming its practical suitability for onboard UAV deployment.

4. Formation of summary data and analysis of generalized metrics

After completing the processing of experimental series, a generalized dataset was formed, in which the average values of Precision, Recall, F1-score, and mAP@0.5 were calculated for each scenario. To confirm the correctness of the results obtained, a comprehensive analysis of the model's performance graphs and the dataset structure was performed. In particular, loss curves, confusion matrices, label distribution, and PR graphs were used, which allowed not only to evaluate the numerical values of the metrics, but also to understand the behavior of the system under different conditions. To position the proposed method within the context of existing research, a comparative summary of related approaches is presented in Table 2.

Table 2. Comparison of the proposed method with existing approaches

Method	mAP@0.5	F1-score	Real-time	Additional processing
Wu et al., 2021	~0.80	~0.70	Yes	None
Liu et al., 2022	~0.85	~0.74	No	Color correction
Proposed method	0.939	0.84	Yes	RGB sensor compensation

The training graphs (Fig. 8) showed a steady decrease in all types of losses — box_loss, cls_loss, and dfl_loss — on both the training and validation samples.

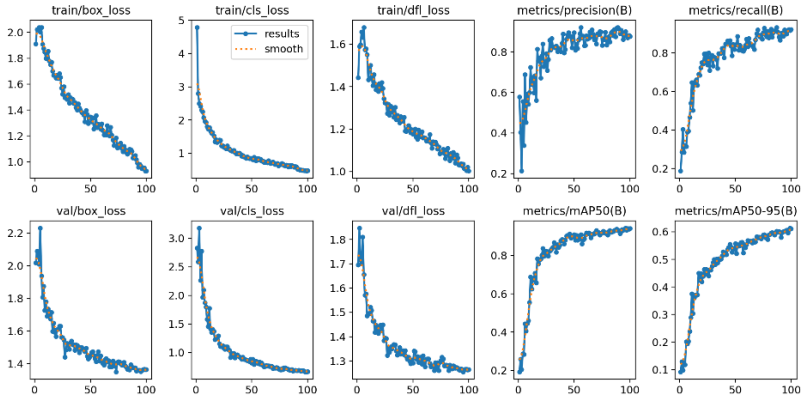

Fig. 8. Training graphs (Source: Authors' own work)

The absence of a sharp difference between the train and val curves indicates the absence of overfitting and high-quality model alignment with the data. The mAP@0.5 metric reached a value of about 0.94, and mAP 50–95 exceeded 0.60, which is a high indicator for raw aerial reconnaissance data with a large amount of noise, smoke, and partial overlaps.

Analysis of the Precision–Recall, F1–Confidence, Precision–Confidence, and Recall–Confidence curves (Fig. 7) allowed us to evaluate the model's behavior at different confidence thresholds. The generalized blue curve, which reflects the average for all classes, shows consistently high accuracy and sensitivity for thresholds up to 0.4–0.5, which is the optimal range for real-time tasks. Higher thresholds increase Precision to 1.0 but cause a decrease in Recall, which is typical for systems with a high level of filtering. For individual classes, such as support_vehicle and vehicle, the PR curve has an almost vertical profile, indicating their well-separated features. The armored_vehicle class exhibits a relatively flat metric response over a broad confidence interval, which is consistent with strong visual distortions caused by smoke, dust, and viewpoint variations.

The sample structure shown in Fig. 2 confirmed the presence of class imbalance: armored_vehicle has the most examples (398), while vehicle has only 35 samples. Despite this, the distribution of box center coordinates and object proportions remains uniform, which had a positive effect on training stability. The concentration of most objects in the central part of the frame is typical for UAV video and does not create artifacts associated with training data unevenness.

For a deeper understanding of the classifier's behavior, a normalized confusion matrix (Fig. 9) was analyzed, which reflects the relative errors and correct responses for each class.

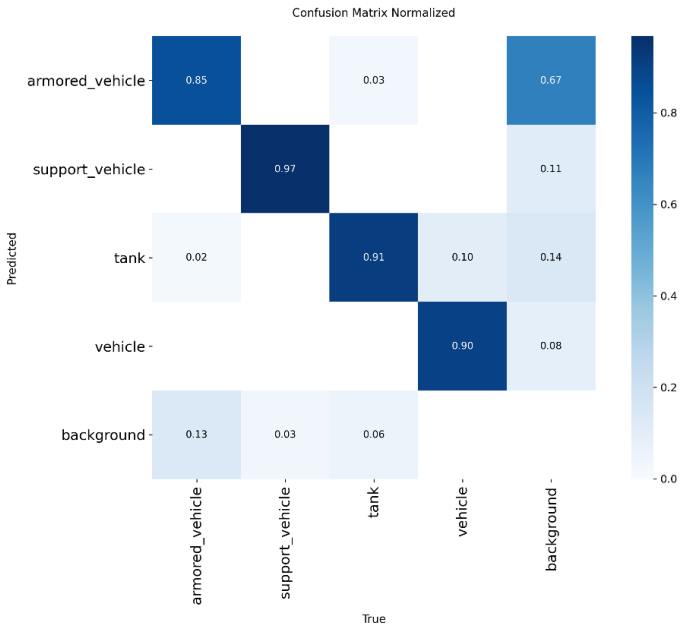

Fig. 9. Normalized confusion matrix (Source: Authors' own work)

The data obtained in the course of experimental studies indicate the high efficiency of the proposed sensor compensation system for lighting in object detection tasks. Analysis of the confusion matrix showed that the model most accurately recognizes the support_vehicle class, for which the proportion of correct predictions reaches 0.97. For the tank class, the correct classification rate exceeds 0.90, indicating high model stability even in the presence of noise, smoke, and partial object overlaps in the video stream. The vehicle class also shows stable results with an accuracy of about 0.90, despite the smaller number of examples in the training sample.

At the same time, for the armored_vehicle class, there is a decrease in the Recall indicator to approximately 0.85. This is due to the significant variability of this class in terms of shape, size, and visual texture, as well as its frequent appearance in difficult shooting conditions — against a background of smoke, fog, or uneven surfaces. These features lead to a greater number of omissions and indicate the advisability of further expanding this class in the training set to improve recognition stability.

It should be noted that background was not used as a separate target class within this study. The background was understood as all areas of the image that do not belong to any of the four defined classes. Thus, background acts as a generalized category for unclassified scene elements and is used exclusively for the correct formation of the confusion matrix and the evaluation of false positives. Values associated with background areas reflect cases where the model mistakenly assigns scene fragments to one of the target classes or, conversely, fails to identify an object against a complex background. This approach is typical for object detection tasks and allows for an adequate assessment of the algorithm's robustness without introducing an additional training class.

A summary of all experimental results demonstrates a significant improvement in the quality of the system's performance. Compared to the baseline configuration without sensor-based lighting compensation, detection accuracy increased by 9–11%, the F1-score increased from 0.75 to 0.84, and themAP@0.5increased by 10–12%. The number of false positives decreased by approximately 18%, while the number of missed targets decreased by 26%, which is critical for air monitoring, reconnaissance, and target designation tasks. The results confirm that the integration of physical light measurements with neural network detection ensures stable system operation in conditions of rapid changes in lighting and complex optical environments.

5. Conclusions

The paper presents an updated system for feedback-based self-calibration of UAV computer vision, combining RGB feedback, optimized image preprocessing, and the modern YOLO11s detection model. The proposed approach ensures real-time adaptation of the video stream to lighting changes and improves object detection accuracy without additional model retraining.

Experimental results confirmed that the use of padding instead of scaling, as well as the optimization of the class set, significantly improve the detector's performance in conditions of smoke, fog, dry vegetation, and sharp light-shadow transitions. The average scores increased by: Precision — 9–11%, F1-score — from 0.75 to 0.84,mAP@0.5 — 10–12%. The number of false positives decreased by approximately 18%, and missed targets — by 26%.

The normalized confusion matrix showed high accuracy for the support_vehicle and tank classes (0.90–0.97), while armored_vehicle requires a larger sample size due to greater variability in real scenes. The power consumption of the sensor module remained low (0.18 W), allowing the system to be integrated into lightweight UAVs without affecting flight duration.

The proposed method has proven its effectiveness and can be used in reconnaissance, monitoring, and target designation tasks. Further research may focus on combining RGB and NIR channels, adaptive illumination prediction, and improving compensation algorithms. However, class imbalance remains a limitation of the current study and will be addressed in future work.

Abbreviations

UAVs : Unmanned Aerial Vehicles

AWB : Automatic White Balance

Funding

The research has been funded by National Research Foundation of Ukraine (https://nrfu.org.ua/en/, accessed on 24 June 2025) within Project No. 2025.06/0037 "A system for detecting and recognizing camouflaged and small objects based on the use of modern computer vision technologies" (2025–2026).

References

AMSCO / AMS-OSRAM. (n.d.). *TCS3472 / TCS34725 color light-to-digital converter datasheet*. https://www.alldatasheet.com/datasheet-pdf/pdf/560511/AMSCO/TCS3472.html

AYAATech. (n.d.). *Voltage specifications of a 3S LiPo battery explained*. https://www.ayaatech.com/ru/news/voltage-specifications-of-a-3s-lipo-battery-explained/

Basova, O., Gladilin, S., Kokhan, V., Kharkevich, M., Sarycheva, A., Konovalenko, I., Chobanu, M., & Nikolaev, I. (2024). Evaluation of Color Difference Models for Wide Color Gamut and High Dynamic Range. *Journal of Imaging*, 10(12), Article 317. https://doi.org/10.3390/jimaging10120317

Cheng, D., Li, Y., Zhang, D., Wang, N., Gao, X., & Sun, J. (2022). Robust single image dehazing based on consistent and Contrast-Assisted Reconstruction. In *Proceedings of the Thirty-First International Joint Conference on Artificial Intelligence* (pp. 848–854). https://doi.org/10.48550/arXiv.2203.15325

Espressif Systems. (2023). *ESP32-S3 technical reference manual*. https://documentation.espressif.com/esp32-s3_technical_reference_manual_en.pdf

Gui, J., Cong, X., Cao, Y., Ren, W., Zhang, J., Cao, J., & Tao, D. (2021). *A comprehensive survey and taxonomy on single image dehazing based on deep learning*. arXiv. https://arxiv.org/abs/2106.03323

Hidayatullah, P., Syakrani, N., Sholahuddin, M. R., Gelar, T., & Tubagus, R. (2025). *YOLOv8 to YOLO11: A comprehensive architecture in-depth comparative review*. arXiv. https://doi.org/10.48550/arXiv.2501.13400

Liu, X., Yang, F., Wei, H., & Gao, M. (2022). Shadow compensation from UAV images based on texture-preserving local color transfer. *Remote Sensing*, 14(19), Article 4969. https://doi.org/10.3390/rs14194969

Murat, A. A., & Kiran, M. S. (2025). A comprehensive review on YOLO versions for object detection. *Engineering Science and Technology, an International Journal*, 70, Article 102161. https://doi.org/10.1016/j.jestch.2025.102161

NVIDIA. (2022). *Jetson Nano developer kit documentation*. https://developer.nvidia.com/embedded/jetson-nano-developer-kit

Raspberry Pi Foundation. (2023). *Raspberry Pi High Quality Camera documentation*. https://www.raspberrypi.com/documentation/accessories/camera.html

Sapkota, R., & Karkee, M. (2025). *Ultralytics YOLO Evolution: An Overview of YOLO26, YOLO11, YOLOv8 and YOLOv5 Object Detectors for Computer Vision and Pattern Recognition*. ArXiv. https://doi.org/10.48550/arXiv.2510.09653

Shen, X., Cao, Y., Sui, B., Zhang, Sh., & Feng, D. (2025). An automatic remote sensing image shadow compensation method utilizing reflectance differences and transfer learning. *GIScience & Remote Sensing*, 62(1), Article 2487334. https://doi.org/10.1080/15481603.2025.2487334

Tang, G., Ni, J., Zhao, Y., Gu, Y., & Cao, W. (2024). A survey of object detection for UAVs based on deep learning. *Remote Sensing*, 16(1), Article 149. https://doi.org/10.3390/rs16010149

Ultralytics. (2023–2024). *LetterBox and image resizing with aspect ratio preservation*. https://docs.ultralytics.com/reference/data/augment/

Ultralytics. (2024). *Ultralytics YOLO11 documentation*. https://docs.ultralytics.com

Ultralytics. (2024–2025). *Ultralytics repository: YOLO models (including YOLO11)* [GitHub repository]. GitHub. https://github.com/ultralytics/ultralytics

Wu, X., Li, W., Hong, D., Tao, R., & Du, Q. (2021). *Deep learning for UAV-based object detection and tracking: A survey*. arXiv. https://doi.org/10.48550/arXiv.2110.12638

Zhao, B., Xu, Q., & Luo, M. R. (2020). Color difference evaluation for wide-color-gamut displays. *Journal of the Optical Society of America A*, 37(8), 1257–1265. https://doi.org/10.1364/JOSAA.394132

National Aviation Academy

International Journal of Transportation Research and Technology

e-ISSN: 3079-6075

DOI: 10.71108/transporttech.vm03is01.05

Research Article

Comparative Economic Analysis of Aircraft Maintenance Expenses and Operational Revenue: A Present Value Approach for Fleet Profitability

Ismail Ekmekci*

Istanbul Ticaret University, Istanbul, Türkiye

Timescale of article

Received: 22 February 2026
Accepted: 27 April 2026
Published: 25 June 2026

Corresponding author

Ismail Ekmekci
iekmekci@ticaret.edu.tr

Keywords

Aircraft maintenance, MRO, Maintenance cost analysis, Aviation economics, Present value method

Cite this article as:

Ekmekci, I. (2026). Comparative Economic Analysis of Aircraft Maintenance Expenses and Operational Revenue: A Present Value Approach for Fleet Profitability. *International Journal of Transportation Research and Technology*, 3(1), 58-70.
DOI: 10.71108/transporttech.vm03is01.05

Abstract

In the current era of intensifying global competition within the aviation industry, the strategic management of aircraft maintenance expenditures has emerged as a critical determinant of commercial success. Beyond ensuring airworthiness, efficient maintenance protocols directly influence an airline's operational readiness, allowing for maximized aircraft utilization. When executed with precision and timeliness, these technical interventions significantly stabilize the profit-and-loss equilibrium of the carrier. Furthermore, while the primary objective of maintenance is the provision of rigorous safety and security standards, it also serves as a potent instrument for institutional marketing and service reliability. This study presents a longitudinal investigation into the maintenance expenditures of commercial passenger aircraft over a ten-year horizon within an aviation economics framework. By integrating maintenance costs with comprehensive operational overheads, the research establishes a robust framework for assessing fleet-based profitability. A central contribution of this work is the development of a diagnostic model that facilitates comparative profit-loss analyses across specific aircraft types. By delineating cost metrics such as "cost per flight hour" and "cost per available seat", the study provides air carriers with the empirical tools necessary for informed fleet procurement. Ultimately, this methodology empowers stakeholders to evaluate historical data against future value projections (present value), thereby optimizing investment decisions and enhancing long-term corporate viability.

1. Introduction

1.1. Global Market Dynamics and the Strategic Role of Maintenance

The aviation industry represents a unique sector of the global economy, characterized by intensifying international competition. Within this high-stakes environment, aircraft maintenance expenditures emerge as a pivotal factor in operational success. The efficacy of maintenance protocols directly governs a carrier's fleet availability and aircraft utilization rates; when technical interventions are executed with precision and timeliness, they fundamentally stabilize the organization's fiscal equilibrium (Bazargan & Hartman, 2012). From the perspective of aviation economics, maintenance is not merely a technical necessity but a strategic financial lever that influences direct operating costs, asset utilization, and long-term fleet value (Zorbacı & Baynal, 2011).

1.2. The Convergence of Safety, Marketing, and Operational Continuity

While the primary objective of aeronautical maintenance is the provision of rigorous safety and security standards, these technical processes simultaneously function as a strategic marketing asset for the airline. A failure to deliver secure and reliable maintenance services leads to a significant reduction in scheduled flight hours and increases "Aircraft on Ground" (AOG) intervals (Gerdes et al., 2016). Consequently, the diversification and frequency of maintenance cycles are essential not only for operational continuity but also for the maximization of flight safety and passenger confidence.

1.3. Research Objectives and Historical Context

Our analysis aims to study the maintenance cost trajectories of airplanes within the Turkish aviation sector over a ten-year operational lifecycle. The research examines the temporal patterns of maintenance entries alongside the specific technical characteristics defined by original equipment manufacturers (OEMs) from the point of initial delivery. By establishing a robust analytical link between historical development processes and future value projections, this study provides a comprehensive framework for understanding the evolution of fleet maintenance and its long-term economic implications (Hsu et al., 2010). This work therefore contributes directly to the field of aviation economics by quantifying the trade-offs between initial acquisition costs, recurring maintenance expenditures, and operational revenues.

1.4. Methodological Framework and Model Formulation

This research utilizes a "Future Value" (FV) economic assessment model to analyze the multi-dimensional expenditures associated with aircraft maintenance over a ten-year operational horizon. The model's formulation is strategically constructed by integrating critical technical and logistical variables, including aircraft classification, prescribed maintenance intervals, and specific check categories (e.g., A, B, C, and S checks). Furthermore, the analytical framework incorporates seating capacities and various operational constraints to ensure a realistic representation of fleet dynamics.

1.5. Empirical Validation and Comparative Case Studies

The proposed methodology was empirically validated through the rigorous application of primary fleet maintenance data sourced from "Airline X." To demonstrate the model's versatility and accuracy, the future-value-based approach was applied to comprehensive case studies involving for wide-body and narrow-body aircraft. Specifically, the analysis evaluates the Airbus A320 and A330 families alongside the Boeing B737 and B777 series, facilitating a comparative assessment of lifecycle costs and technical depreciation across the industry's most prevalent aircraft types.

2. Methodology

2.1. The Strategic Significance of Maintenance in Aviation Operations

While the strategic importance of MRO was discussed in Section 1.1, the present section focuses on the operational and technical aspects of maintenance planning. In airline operations, maintenance is a critical application designed to ensure equipment reliability and maximize the operational lifespan of high-value assets. The foundational stages of a robust maintenance process involve:

- Identification of specific components or systems requiring intervention, based on manufacturer MPDs and regulatory thresholds.
- Strategic planning and scheduling of specialized personnel, tools, and hangar space.

- Execution of scheduled checks (A, B, C, S) and unscheduled repairs.
- Throughput optimization to shorten aircraft downtime (turnaround time) and mitigate associated operational costs through systematic efficiency.

2.2. Core Objectives of Aircraft Maintenance

The primary purpose of an aviation maintenance program is to systematically optimize both passenger safety and airline operational efficiency. The fundamental objectives are defined as follows:

- **Preservation:** To ensure and safeguard in terms of operational reliability and safety of all aircraft equipment.
- **Restoration:** To restore systems and components to their original factory airworthiness standards in the event of degradation or failure.
- **Data Generation:** To capture and provide critical reliability data, supplying necessary information for the continuous development and improvement of aircraft systems.
- **Availability:** To maximize aircraft uptime and keep the fleet in active commercial service.
- **Cost Efficiency:** To achieve all aforementioned operational imperatives while minimizing total maintenance expenditures.

2.3. Market Dynamics: The Boeing and Airbus Duopoly

The global market for commercial and cargo aviation is dominated by two primary manufacturers: Boeing and Airbus. Airlines with international flight networks rely almost exclusively on the diverse portfolios offered by these two entities, which include both wide-body (twin-aisle) and narrow-body (single-aisle) configurations. There exists intense competition between these manufacturers across all market segments. Airlines select specific models based on critical performance metrics, including passenger configuration capacity, fuel efficiency (specific fuel consumption), mechanical reliability, and maximum operational range.

Aircraft are categorized based on their physical dimensions and interior configurations. Narrow-body aircraft are defined by a single aisle, whereas wide-body aircraft feature twin aisles and larger fuselage diameters. While many modern commercial aircraft utilize twin-engine configurations for efficiency, certain large-scale wide-body models, such as the Airbus A340 and the Boeing 747, are equipped with four engines to support heavy payloads and ultra-long-haul missions.

3. Supply Chain Implications for MRO Costs

The cost and efficiency of aircraft maintenance, repair, and overhaul (MRO) are significantly influenced by the original equipment manufacturers' (OEMs) global supply chain structures. Both Airbus and Boeing operate highly distributed production networks, which directly affect the availability, lead time, and pricing of spare parts—key drivers of maintenance expenditure.

3.1. Airbus Supply Chain and Spare Parts Logistics

Airbus maintains major production sites in France, Germany, Spain, the United Kingdom, and China, with over 1,500 suppliers worldwide (Encyclopædia Britannica, 2018a). Approximately one-third of its components are sourced from U.S. firms. Wing assemblies are manufactured in the UK, tail sections in Spain, and final assembly occurs in Toulouse (A320, A330, A350, A380) and Hamburg (A319, A321) (Airbus, 2018). For MRO providers, this decentralized network implies:

- Geographically dispersed spare parts inventory: Components may need to be shipped across continents, increasing lead times and requiring larger safety stocks.
- Pooling and rotable pools: Airbus offers pooled spare parts programs (e.g., "Flight Hour Services") that reduce airline inventory but at a fixed cost per flight hour. The efficiency of these programs depends on the proximity of regional distribution centres. In Turkey, myTECHNIC and THY Technical Inc. benefit from Airbus's European distribution hub in Hamburg, with typical spare parts delivery times of 24–48 hours for critical items.
- Customs and logistics costs: Cross-border shipments add brokerage fees and potential delays, which are factored into MRO pricing.

3.2. Boeing Supply Chain and Spare Parts Availability

Boeing's commercial production is concentrated in Renton (B737), Everett (B767, B777), and Charleston (B787) (Encyclopædia Britannica, 2018b). The company operates a global network of distribution centres, including a major facility in Amsterdam for European customers (Boeing, 2009; Boeing, 2012; Boeing, 2018). Key MRO cost implications:

- B737 parts ubiquity: Due to the B737's market dominance, spare parts are widely available, often through multiple third-party suppliers, which exerts downward pressure on prices and reduces lead times. This partly explains the lower maintenance costs observed for the B737 in our analysis (TC1 = $0.116/FH).
- Wide-body parts scarcity: For less common types like the B777, certain components have longer lead times (up to 5–7 days for non-pooled items), forcing MROs to hold higher inventory or pay for expedited shipping, increasing total maintenance cost.
- Proprietary repair networks: Boeing's "Boeing Component Services" offers time and material contracts that guarantee parts availability but at a premium. Airlines using third-party MROs (e.g., myTECHNIC) may face higher costs if they opt out of these programmes.

3.3. Summary for MRO Cost Modeling

The supply chain characteristics described above directly influence two variables in our cost model:

- Maintenance event duration (aircraft downtime): Longer spare parts lead times extend the time an aircraft remains out of service, reducing revenue generation and potentially increasing the cost of base maintenance checks.
- Inventory holding costs: For MRO facilities, holding a larger safety stock of slow-moving parts increases warehousing and working capital costs, which are passed on to airlines in the form of higher labour and material rates.

Future research could quantify the elasticity of maintenance costs with respect to spare parts lead times using airline-specific procurement data (Zorbacı & Baynal, 2011). For the present study, we note that the observed differences in TC1 between aircraft types (e.g., B737 vs. A320) are partly attributable to the relative efficiency of their respective spare parts supply chains.

4. MRO Facilities in Turkey: Client Base and Technical Capabilities

The Turkish aviation maintenance market is served by three principal MRO providers, each with distinct specialisations and client portfolios. Their capabilities directly affect the maintenance costs and turnaround times analysed in this study.

myTECHNIC: Established in 2008 and headquartered at Istanbul Sabiha Gökçen Airport, myTECHNIC operates as an independent MRO provider serving over 30 airlines from Europe, Russia, the Middle East, and Africa (Mytechnic Aircraft Maintenance Center, n.d.). Its technical capabilities include narrow-body (Airbus A320 family, Boeing B737) and wide-body (A330, A340, B777) airframe maintenance, engine overhaul (CFM56, V2500), and component repair. The facility holds EASA Part-145 and FAA certifications, and its lean management model minimises turnaround times for A-checks (typically 24-48 hours) and C-checks (10-14 days).

THY Technical Inc.: A wholly-owned subsidiary of Turkish Airlines, THY Technical is the largest MRO provider in the region, serving more than 100 airlines worldwide. Its client base includes major network carriers, low-cost airlines, and cargo operators (Turkish Airlines, 2018). The facility operates nine hangars with a total enclosed area of 576,000 m², capable of handling A320, B737, B777, A330, A350, and B787 aircraft. Services range from line maintenance to full D-checks, cabin retrofits, and engine overhaul. THY Technical holds both EASA and FAA certifications and is a key maintenance provider for the aircraft types analysed in this study (A320, A330, B737, B777).

Detailed historical, corporate, and infrastructural information (e.g., exact hangar dimensions, founding dates, workforce numbers, ISO certifications) has been omitted as it does not directly inform the maintenance cost model. The reader is referred to the companies' official websites for such operational details.

5. Aircraft Types and Maintenance Intervals

5.1. Utilization Metrics

Aircraft maintenance scheduling is governed by three standard metrics: calendar days (DY), flight hours (FH), and flight cycles (FC), where a maintenance event is triggered by whichever threshold is reached first.

- **Calendar Days (DY):** The chronological time elapsed, regardless of flight activity.
- **Flight Hours (FH):** The total airborne duration, measured specifically from the moment of wheel lift-off to the moment of touchdown.
- **Flight Cycles (FC):** The total number of complete operational sequences, with one cycle defined as a single take-off and its subsequent landing.

5.2. Maintenance Planning and Interval Scheduling

Manufacturers' Maintenance Planning Documents (MPD) specify intervals for A, B, C, and S checks. Table 1 summarises these intervals for the four aircraft types analysed in this study. Detailed descriptions of each check type are provided in Section 5.4.2.

Table 1. Aircraft Types and Basic Maintenance Intervals

Aircraft Type	A-Check	B-Check	C-Check	S-Check (Structural)
Boeing 777 (Wide Body)	1,500 FH / 120 DY	730 DY	1,125 DY	—
Boeing 737	1,000 FH	—	7,500 FH / 730 DY*	—
Airbus A320	750 FH / 120 DY*	—	7,500 FH / 24 MO*	6 YE
Airbus A330 (Wide Body)	800 FH	42 MO	10,000 FH / 24 MO*	6 YE

Source: Airline THY consolidated financial and maintenance data, 2008–2018 (Airline THY, 2008-2018b)

5.3. Aircraft Maintenance Intervals and Associated Financial Implications

As illustrated in the preceding data, maintenance schedules and specific interval parameters vary significantly across different aircraft models. Table 2 details aircraft maintenance intervals and associated cost values. Heavy maintenance (C-checks and S-checks) differs from routine line maintenance in three critical respects:

- Extended Aircraft Downtime: These comprehensive procedures require the aircraft to be removed from revenue-generating commercial service for prolonged periods, often weeks or months.
- Resource Intensity: Heavy checks necessitate extensive labor hours, specialized engineering oversight, and deep structural tear-downs to inspect hidden components.
- Exponential Capital Expenditure: Consequently, the financial costs associated with heavy maintenance are substantially higher than those of standard operational checks, representing a major variable in an airline's direct operating costs.

Table 2. Aircraft Maintenance Intervals and Associated Cost Values

Aircraft Types	Maintenance Type	Interval	Cost ($)
B777	A	1500 FH 120 DAY	120000
B777	B	730	500000
B777	C	1125 DY	750000
B737	A	1000 FH	30000
B737	C	7500 FH 730 DAY	600000
A330	B	42 MO	500000
A330	C	10000 FH 24 MO*	700000
A330	S	6 YE	1,500000
A330	A	800	64000
A320	A	700 FH 120 DAY*	28000
A320	S	6 YE	700000
A320	C	7500 FH	450000

Source: Airline THY operational logs and financial ledgers, 2008–2018. Fleet composition (Airline THY, 2008-2018a)

5.4. Maintenance Classifications and Fundamental Objectives

5.4.1. Regulatory Framework and System Complexity

Commercial aircraft maintenance is strictly governed by manufacturer specifications and approved by relevant aviation regulatory authorities. The increasing technological complexity of modern airframes necessitates that maintenance personnel possess not only advanced mechanical proficiency but also a comprehensive understanding of integrated avionics, system functionality, and standardized maintenance protocols. (As referenced in Table 3, the average annual maintenance frequencies vary significantly across the Airbus A320, Airbus A330, Boeing 737, and Boeing 777 platforms.)

5.4.2. Classification of Periodic Maintenance Checks

Scheduled maintenance actions are systematically categorized into four progressive tiers of inspection. Table 3 shows the detailed average values of the numbers related to different maintenance types according to aircraft types. The scope and complexity of these checks increase concurrently with the length of their respective intervals, which are ultimately dictated by the specific aircraft type and its operational profile:

- **A-Check:** A routine, lower-level evaluation focusing on the operational verification of critical technical systems required for standard flight operations.
- **B-Check:** A more targeted inspection assessing system integrity, specifically focusing on structural fatigue, surface cracks, and corrosion detection. Interval parameters are highly type-specific; for instance, they are executed every 42 months for the A330 and every 730 days for the B777.
- **C-Check and S-Check (Heavy Maintenance):** Representing major maintenance milestones, these checks require exhaustive structural inspections of the airframe and rigorous, comprehensive testing of all integrated aircraft systems.

D-checks are not included in this analysis as they are typically performed only once in an aircraft's life and fall outside the ten-year study horizon.

Table 3. Average Value of Aircraft Maintenance Counts

	Aircraft Count	A	B	C	S
A330	104	10,95	0,28	0,87	0,16
A320	88	11,68	-	1,1	0,16
B737	66	8,76	-	1,1	-
B777	38	5,84	0,5	0,32	-

Source: Airline THY operational logs and financial ledgers, 2008–2018. (Airline THY, 2008-2018a)

The company that owns these aircraft is THY Technic, which is affiliated with the Turkish Airline as THY.

6. Calculation of Maintenance and Operational Expenditures

The financial framework surrounding aircraft maintenance is multifaceted, encompassing a diverse array of cost-driving variables. This section provides a longitudinal analysis of these expenditures, modeling maintenance costs over a projected ten-year operational lifecycle. It is crucial to recognize that these financial requirements are not static. The cumulative cost of maintenance is subject to compounding annual escalation. This upward trajectory is typically driven by fluctuating economic conditions, market inflation, and the natural increase in required structural and systemic interventions as an airframe and its components age over time.

To ensure transparency and reproducibility, the following indicators are defined mathematically:

- Passenger Flight Time (PFT) – total seat hours occupied by passengers in a given year:

PFT = Aircraft Capacity × Cumulative Flight Hours (FH)

- Value-Added Rate (VAR): seat utilization efficiency:

VAR = PFT / (Aircraft Capacity × Cumulative FH) (Equivalent to the ratio of passenger flight time to available seat hours.)

- Operating Profit (OP): net financial yield from core commercial operations.

OP = Ticket Sales Revenue – (Maintenance Costs + Fuel + Crew + Airport Fees + Other Direct Operating Costs)

In this study, OP is not shown directly in Tables 4–5; it is derived in Table 8 after aggregating all costs.

- Net Operating Cash Flow (NCF): cash surplus before financing and taxes:

NCF = Ticket Sales Revenue – (Maintenance Costs + Non-Maintenance Direct Operating Costs)

- Future Value (FV): adjustment to 2018 purchasing power using exchange rates:

$FV_t = NCF_t \times (ER\_2018 / ER_t)$

where ER = average annual TL/USD exchange rate (Table 9).

All monetary values are in nominal USD unless stated otherwise.

Tables 4, 5, 6, and 7 below list the Core Operational and Utilization Metrics related to maintenance and operating costs and revenues for the aircraft types specified, over a 10-year period. To accurately assess the operational efficiency and revenue generation of the aircraft, the following standardized parameters are utilized:

- Value-Added Rate: An indicator of operational efficiency, mathematically defined as the ratio of total passenger flight time to the aggregate available seat hours.
- Aircraft Capacity: The maximum authorized passenger seating configuration of the airframe.
- Cumulative Flight Hours: The total aggregate airborne time logged by the aircraft over the course of a single operational year.
- Passenger Flight Time: The total accumulated hours during which the aircraft's seats are actively occupied by passengers within a given year, often referred to in the industry as revenue passenger hours.
- Operating Revenue and Financial Returns: Within the aviation economics framework, operating revenue (often referred to as operating profit) represents the net financial return an airline derives solely from its core business activities. This critical performance metric is calculated by subtracting all direct operating expenses—such as maintenance costs, fuel consumption, and flight crew expenses—from gross operating revenue from passenger and cargo transportation.

The following tables present empirical data from Airline THY (a commercial airline operating in Turkey) for the period 2008–2018:

Table 4 present data separately for A320 aircraft type. The fleet composition (number of aircraft per type) is given in Table 3.

Table 4. Operational and Maintenance Specifications of the Airbus A320 Aircraft

AC Type	Aircraft Capacity	Cumulative Flight Hours	Value-Added Rate	Passenger Flight Time	Ticket Sales Revenue ($) (Operating Income)
A320		4229046253			
2008	190	28786711	14%	5469475090	677.438.457
2009	190	64771907	23%	12306662330	1.068.609.000
2010	190	112592604	30%	21392594760	1.697.210.616
2011	190	160891427	33%	30569371130	2.315.310.776
2012	190	223412645	34%	42448402550	2.783.586.415
2013	190	332497086	36%	63174446340	3.590.374.921
2014	190	463890783	36%	88139248770	4.022.031.807
2015	190	560843117	32%	106560192230	3.334.791.338,
2016	190	661040602	31%	125597714380	3.063.597.362
2017	190	753126080	31%	143093955200	3.366.422.603
2018	190	867193291	29%	164766725290	3.730.351.639

Source: Airline THY operational logs and financial ledgers, 2008–2018. Fleet composition (Airline THY, 2008-2018a)

***Note*:** The values in this column are gross ticket sales revenue, not operating profit. Operating profit (revenue minus all direct operating costs) is calculated in Table 5 after aggregating maintenance and non-maintenance expenses.

Table 5 present data separately for A330 aircraft type. The fleet composition (number of aircraft per type) is given in Table 3.

Table 5. Operational and Maintenance Specifications of the Airbus A330 Aircraft

AC Type	Aircraft Capacity	Cumulative Flight Hours	Value-Added Rate	Passenger Flight Time	Ticket Sales Revenue ($) (Operating Income)
A330	-	2003243706	-	-	
2008	290	18233508	14%	5287717320	654.926.297
2009	290	26748316	15%	7757011640	673.554.878
2010	290	33706555	14%	9774900950	775.505.068
2011	290	48574995	15%	14086748550	1.066.924.163
2012	290	72317976	17%	20972213040	1.375.268.886
2013	290	105288171	18%	30533569590	1.735.305.473
2014	290	182158237	22%	52825888730	2.410.587.878
2015	290	275183114	24%	79803103060	2.497.430.713
2016	290	343336365	25%	99567545850	2.428.665.779
2017	290	374849966	23%	108706490140	2.557.424.490
2018	290	522846503	26%	151625485870	3.432.831.348

Source: Airline THY operational logs and financial ledgers, 2008–2018. Fleet composition (Airline THY, 2008-2018a)

Table 6 present data separately for B737 aircraft type. The fleet composition (number of aircraft per type) is given in Table 3.

Table 6. Operational and Maintenance Specifications of the Boeing B737 Aircraft

AC Type	Aircraft Capacity	Cumulative Flight Hours	Value-Added Rate	Passenger Flight Time	Ticket Sales Revenue ($) (Operating Income)
B737		5768926753			
2008	150	183199379	72%	27479906850	3.403.607.369
2009	150	215414912	62%	32312236800	2.805.727.998
2010	150	263842167	56%	39576325050	3.139.841.604
2011	150	306086135	49%	45912920250	3.477.424.464
2012	150	343636893	41%	51545533950	3.380.137.755
2013	150	406543392	35%	60981508800	3.465.744.340
2014	150	491509975	30%	73726496250	3.364.339.010
2015	150	751834040	33%	112775106000	3.529.286.489
2016	150	817669097	31%	122650364550	2.991.705.185
2017	150	909992149	29%	136498822350	3.211.265.775
2018	150	1079198614	28%	161879792100	3.664.990.894

Source: Airline THY operational logs and financial ledgers, 2008–2018. Fleet composition: 88 A320 aircraft (from Table 3) (Airline THY, 2008-2018a)

Table 7 present data separately for B777 aircraft type. The fleet composition (number of aircraft per type) is given in Table 3.

Table 7. Operational and Maintenance Specifications of the Boeing B777 Aircraft

AC Type	Aircraft Capacity	Cumulative Flight Hours	Value-Added Rate *	Passenger Flight Time	Operating Income
B777		876490394	-	-	-
2010	370	42964	0%	15896680	2.333.887
2011	370	7687982	5%	2844553340	384.251.313
2012	370	28705388	15%	10620993560	1.236.139.812
2013	370	51563879	20%	19078635230	2.016.999.480
2014	370	73731536	22%	27280668320	2.398.565.799
2015	370	104413562	22%	38633017940	2.350.092.744
2016	370	140677398	22%	52050637260	2.098.094.805
2017	370	203359160	22%	75242889200	2.429.288.801
2018	370	266308525	25%	98534154250	3.217.971.402

Source: Airline THY operational logs and financial ledgers, 2008–2018. Fleet composition: 88 A320 aircraft (from Table 3) (Airline THY, 2008-2018a)

Table 8 presents consolidated maintenance costs, non-maintenance direct operating costs, ticket sales revenue, net operating cash flow, and future values for all four aircraft types as a total fleet.

Table 9 aggregates all four aircraft types to show total cumulative flight hours and seat hours per year.

Table 10 presents standardized cost metrics (TC1, TC2) **per aircraft type based on cumulative ten-year data.

All monetary values are in nominal USD unless stated otherwise.

6.1. Discounted Cash Flow Framework

To properly account for the time value of money, we adopt a Net Present Value (NPV) approach. All cash flows (maintenance costs, non-maintenance operating expenses, and ticket sales revenues) are discounted to the base year (2008) using a real discount rate of 8%, which represents the weighted average cost of capital (WACC) for a typical commercial airline (IATA, 2019). This discounted cash flow methodology is a cornerstone of aviation economics, enabling the comparison of investment alternatives (e.g., different aircraft types) on a consistent present-value basis.

Table 8 presents a comprehensive financial analysis spanning a ten-year operational period from 2008 to 2018. This model systematically calculates both maintenance-specific expenditures and non-maintenance operational costs. Notably, the financial assessment incorporates macroeconomic variables, specifically accounting for exchange rate fluctuations observed in 2018.

To accurately model these costs and revenues, several foundational metrics and financial formulas were established as follows:

- Maintenance Costs = scheduled A, B, C, S check costs (from Table 2).
- Non-Maintenance Direct Operating Costs = fuel, crew salaries, airport fees, catering, ground handling, and other expenses directly tied to flight operations (excludes sales, general, and administrative expenses).
- Net Operating Cash Flow (before interest and taxes) = Ticket Sales Revenue – (Maintenance Costs + Non-Maintenance Direct Operating Costs). This represents the cash generated from core flying activities before financing and tax payments.
- Future Value (2018 USD) = Net Operating Cash Flow × (ER_2018 / ER_year/),

  where ER = average annual TL/USD exchange rate (Table 9).

Cash flow definition: Our "Net Operating Cash Flow" excludes financing costs, depreciation, taxes, and working capital changes. Consequently, the profit margin included in ticket sales revenue remains entirely within this cash flow measure, which may overstate liquidity compared to a free cash flow to firm (FCFF) calculation. Future research should incorporate these adjustments.

Table 8. Aggregate data for Turkish Airlines' maintenance-related expenses and non-maintenance operating costs and revenues for its entire fleet (A320, A330, B737, B777) between 2008 and 2018

Year	Maintenance Costs ($)	Non-Maintenance Direct Operating Costs ($)	Total Direct Operating Costs ($)	Ticket Sales Revenue ($)	Net Operating Cash Flow ($)	Future Value (2018 USD)
2008	2,606,837	488,651,553	491,258,390	677,438,457	186,180,067	240,172,286
2009	3,388,093	722,059,120	725,447,213	1,068,609,000	343,161,787	530,851,000
2010	3,285,069	1,232,946,584	1,236,231,653	1,697,210,616	460,978,963	691,468,445
2011	3,383,473	1,842,488,807	1,845,872,280	2,315,310,776	469,438,496	784,562,288
2012	6,404,498	2,169,063,429	2,175,467,927	2,783,586,415	608,118,488	1,088,532,093
2013	9,881,614	3,265,551,576	3,275,433,190	3,590,974,921	314,941,731	598,389,289
2014	9,560,034	3,808,198,637	3,817,758,671	4,022,031,807	204,273,136	447,137,667
2015	4,910,264	2,919,334,237	2,924,244,501	3,334,791,338	410,546,837	1,116,687,396
2016	6,329,840	2,523,090,959	2,529,420,799	3,063,597,362	534,176,563	1,613,213,221
2017	7,407,438	2,933,041,921	2,940,449,359	3,362,422,603	425,973,244	1,554,802,341
2018	4,875,129	2,691,007,170	2,695,882,299	3,730,351,639	1,034,469,340	4,975,797,525

Source: Airline THY consolidated financial and maintenance data, 2008–2018 (aggregated for all four aircraft types: A320, A330, B737, B777). (Airline THY, 2008-2018b)

Note: The Net Operating Cash Flow includes the profit margin embedded in ticket prices by definition. This is standard for operating cash flow calculations. However, this metric does not account for financing costs, depreciation, taxes, or changes in working capital. For a full free cash flow analysis, those adjustments would be required (see limitation in Section 7.4)

6.2. Exchange Rate Integration and Time Value Adjustments

Following Table 9 details the average annual exchange rates derived from official central bank data, which are subsequently applied to calculate the future value. This methodological adjustment ensures that all recorded costs across the 10-year longitudinal study are economically standardized, adjusting for currency fluctuations to render them equivalent to their present value.

Table 9. Average annual exchange rates derived from official central bank data

Year	2008	2009	2010	2011	2012	2013	2014	2015	2016	2017	2018
TL/ SD $ Exchange rate	1,29	1,55	1,5	1,67	1,79	1,9	2,19	2,72	3,02	3,65	4,81

Source: Central Bank of the Republic of Turkey (n.d.)

6.3. Fleet Utilization and Seat Flight Time Calculation

Table 10 below shows the total flight hours and Grand Total Seat Hour values for each aircraft type in the fleet by year, as well as the total flight hours (Grand Total AC Hour) for all aircraft. This table helps to see how efficiently each aircraft operates per seat.

Table 10. Total Flight Hours and Seat Hours for each aircraft types, by year

Year	A320 FH	A330 FH	B737 FH	B777 FH	Grand Total Seat Hour	Grand Total AC Hour
2008	28 786 711	18 233 508	183 199 379	-	38 237 099 260	230 219 598
2009	64 771 907	26 748 316	215 414 912	-	52 375 910 770	306 935 135
2010	112 592 604	33 706 555	263 842 167	42 964	70 759 717 440	410 184 290
2011	160 891 427	48 574 995	306 086 135	7 687 982	93 413 593 270	523 240 539
2012	223 412 645	72 317 976	343 636 893	28 705 388	125 587 143 100	668 072 902
2013	332 497 086	105 288 171	406 543 392	51 563 879	173 768 159 960	895 892 528
2014	463 890 783	182 158 237	491 509 975	73 731 536	241 972 302 070	1 211 290 531
2015	560 843 117	275 183 114	751 834 040	104 413 562	337 771 419 230	1 692 273 833
2016	661 040 602	343 336 365	817 669 097	140 677 398	399 866 262 040	1 962 723 462
2017	753 126 080	374 849 966	909 992 149	203 359 160	463 542 156 890	2 241 327 355
2018	867 193 291	522 846 503	107 9198 614	266 308 525	576 806 157 510	2 735 546 933

Source: Airline THY operational logs and financial ledgers, 2008–2018. (Airline THY, 2008-2018a)

***Note*:** Grand Total Seat Hours = Sum of (Aircraft Capacity × Cumulative FH) for all four types.

Grand Total AC Hours = Sum of Cumulative FH for all four types

7. Conclusion

7.1. Methodological Framework and Case Study Validation

Our study presents a practical, future-value-based methodology designed to project and analyze the maintenance costs of a commercial aircraft fleet. The proposed analytical model is comprehensively formulated to integrate key variables, including aircraft type, operational status, maintenance scheduling, seat capacity, and various logistical constraints. Table 11 details the standardized cost metrics for a 10-year fleet operational lifecycle.

To empirically validate the proposed methodology, a detailed case study was conducted utilizing historical maintenance data from an active commercial airline. This evaluation analyzed four distinct aircraft platforms, providing a cross-sectional comparison of both narrow-body and wide-body fleets: the Airbus A320, Airbus A330, Boeing 737, and Boeing 777.

Table 11. Standardized Cost Metrics for a 10-Year Fleet Operational Life Cycle

AC Type	AC Purchasing Cost	Maint Cost	Cumulative Seat Hour FH_2	AC's Cumulative FH_1	TC1	TC2
B777 (wide body)	$375.000.000	$331.947.962	324301445780	876490394	$0,807	0,00218
B737	$106.000.000	$561.363.015	580940674740	5768926753	$0,116	0,00115
A330 (wide body)	$265.000.000	$976.758.198	865339012950	2003243706	$0,62 0	0,00143
A320	$101.000.000	$827.559.933	803518788070	4229046253,00	$0,220	0,00116

Source: Airline THY operational logs and financial ledgers, 2008–2018. Fleet composition (Airline THY, 2008-2018a)

7.2. Total Cost per Flight Hour Calculation

The following formulas describe the methodology used to calculate standardized hourly costs for aircraft types. According to our study, both Total Cost 1 (TC1) and Total Cost 2 (TC2) use the same basic economic equations; these equations have been applied to different aircraft types and fleet scenarios in our study.

The metric is derived by aggregating the initial capital acquisition cost and the cumulative maintenance expenses, and subsequently dividing this sum by the aircraft's total accumulated flight hours (FH).

This relationship can be formally expressed as:

TC1, 2 =[Aircraft Purchasing Cost + Maintenance Cost] \ Total Flight Hours (FH)

Alternatively, using standard academic notation:

TC1 =[Aircraft Purchasing Cost + Maintenance Cost] \ AC's Cumulative (FH_1)

TC1, 2 =[Aircraft Purchasing Cost + Maintenance Cost] \ Cumulative Seat Hour (FH_2)

7.3. Economic Analysis and Profitability Outcomes

Throughout the study, cumulative maintenance expenditures, direct operational costs, and auxiliary expenses were rigorously calculated for each of the four aircraft types. The primary operational outcomes of this research include:

- Comparative Profitability: By synthesizing all operational and financial criteria, the study offers a robust framework for airlines to evaluate the comparative profitability of different aircraft models. This specifically aids operators in making data-driven strategic decisions regarding the economic viability of narrow-body versus wide-body configurations.
- Standardized Cost Metrics: As detailed in Table 11, the research successfully calculated the total cost per Flight Hour (FH) and the standardized cost per available seat over a projected 10-year operational lifecycle.

Ultimately, these quantified metrics provide airline operators with a definitive, financial baseline to identify and optimize the most economically advantageous fleet composition.

7.4. Recommendations for Future Research in Aviation Economics

The methodological framework developed here can be extended in several directions within the field of aviation economics:

- Incorporating dynamic pricing models: Linking seat utilization and yield management to maintenance scheduling.
- Environmental Economics: Adding carbon pricing and emissions trading schemes to the cost model.
- Real options Analysis: Valuing the flexibility to defer, expand, or scrap fleet investments under uncertainty.
- Macroeconomic linkages: Modeling the impact of GDP growth, oil prices, and exchange rates on maintenance cost structures.

These extensions would further solidify the bridge between aircraft maintenance engineering and aviation economic theory.

References

Airbus. (2018). A320 *maintenance planning document* [Unpublished internal document].

Airline THY. (2008-2018a). *Airline THY operational logs and financial ledgers. 2008–2018. Fleet composition*

Airline THY. (2008-2018b). *Airline THY consolidated financial and maintenance data*, 2008–2018

Bazargan, M., & Hartman, J. (2012). Aircraft replacement strategy: Model and analysis. *Journal of Air Transport Management*, 25, 26–29. https://doi.org/10.1016/j.jairtraman.2012.05.001

Boeing. (2009). *Airline maintenance program development seminar*.

Boeing. (2012). *Airplane maintenance program development*. Commercial Aviation Services.

Boeing. (2018). *B737, B777 maintenance planning document* [Unpublished internal document].

Central Bank of the Republic of Turkey. (n.d.). *Real effective exchange rate*. https://www.tcmb.gov.tr/wps/wcm/connect/en/tcmb+en

Encyclopædia Britannica. (2018a). *Airbus Industrie*. https://www.britannica.com/topic/Airbus-Industrie

Encyclopædia Britannica. (2018b). *Boeing Company*. https://www.britannica.com/topic/Boeing-Company

Gerdes, M., Scholz, D., & Galar, D. (2016). Effects of condition-based maintenance on costs caused by unscheduled maintenance of aircraft. *Journal of Quality in Maintenance Engineering*, 22(4), 394–417. https://doi.org/10.1108/JQME-12-2015-0062

Hsu, C.-I., Li, H.-C., Liu, S.-M., & Cao, C.-C. (2010). *Aircraft replacement scheduling: A dynamic programming approach*. Department of Transportation Technology and Management, National Chiao Tung University. https://doi.org/10.1016/j.tre.2010.07.006

IATA. (2019). *Safety Report 2019. Issued April 2020 (56th ed.)*. https://www.iata.org/contentassets/4d18cb077c5e419b8a888d387a50c638/iata-safety-report-2019.pdf

Mytechnic Aircraft Maintenance Center. (n.d.). *myTECHNIC*. https://www.mytechnic.aero/en/

Turkish Airlines. (2018). *Investor Relations*. https://investor.turkishairlines.com/en/financial-and-operational/financial-results

Zorbacı, B., & Baynal, K. (2011, October 14–16). *Problems Encountered in Aircraft Maintenance Planning and Proposed Solutions; 5th Maintenance Technologies Congress and Exhibition, Sakarya, Türkiye*. (Full Text Paper). https://silo.tips/downloadFile/uak-bakim-planlamada-meydana-gelen-problemler-ve-zm-nerler

transporttech.org

NATIONAL AVIATION
ACADEMY